Dual contrast microvascular MRI

HoeSu Jung

Department of Biomedical Engineering

Graduate School of UNIST

2016

Dual contrast microvascular MRI

HoeSu Jung

Department of Biomedical Engineering

Graduate School of UNIST

Dual contrast microvascular MRI

A thesis/dissertation
submitted to the Graduate School of UNIST
in partial fulfillment of the
requirements for the degree of
Doctor of Philosophy

HoeSu Jung

06. 03. 2016 of submission

Approved by

Advisor
HyungJoon Cho

Dual contrast microvascular MRI

HoeSu Jung

This certifies that the thesis/dissertation of HoeSu Jung is approved.

06. 03. 2016 of submission

Advisor: HyungJoon Cho

Sebyung Kang

Jongnam Park

Sungyou Hong

Gyunggoo Cho

Abstract

The fundamental magnetic resonance angiography (MRA) has been used for obtaining vascular information, such as vessel size and structure. For many decades, MRA techniques with contrast agent have been developed and implemented in research and the clinical area for *in vivo* applications. Especially, the longitudinal (T_1) and transverse (T_2 or T_2^*) contrasts in MRA provide diverse and different information of same subject's vasculature. The assessments of vascular structure and function by using two types of contrast are important for monitoring vascular behavior.

Generally, the two types of contrast agent are T_1- and T_2-contrast agents. In recent years, several efforts have been focusing on synthesizing hybrid nanoparticles to achieve T_1- and T_2-contrast, simultaneously. The MR images with both positively and negatively enhanced contrast over the same anatomical region offer complementary information. The benefits of dual contrast with a single agent for *in vivo* experiments are obvious.

In this study, instead of synthesized hybrid contrast agents or multiple contrast agents, simultaneous acquisitions of *in vivo* dual contrast with size-controlled superparamagnetic iron oxide nanoparticles (SPION) in MRA were obtained and evaluated. As this method is successful for preclinical investigations, dual contrast has a great potential to directly help to compensate vascular information by positively and negatively enhanced contrast. The results of obtained dual contrast in *in vivo* images were apparent, the smaller vessels in the head region of rodents were distinctively visible from negatively enhanced contrast MRA, while positively enhanced contrast MRA eliminated false contrasts in regions of airways and bone from negatively enhanced contrast MRA.

Based on advantages of dual contrast in *in vivo* MRA, we systematically compared the strengths and weaknesses of dual contrast-enhanced MRAs with SPION in cerebral micro-vessels of the rodent brain. The vasculatures in rodent brain with positively enhanced contrast were visualized well without any artifact, but smaller vessels than given spatial resolution were hardly detected. On the other hand, negatively enhanced contrast based MRA provided good sensitivity for micro-vessels. However, negatively enhanced vessels and specific regions suffered from susceptibility-induced artifacts. Consequently, dual contrast enhanced MRAs were combined for compensation of those shortcomings and visualization of whole-brain micro-MRA.

The other subject of this thesis is a feasibility evaluation of newly developed contrast agent for *in vivo* applications at high magnetic field. From MR perspective, the behavior of higher magnetic field (> 7T) is attractive, as it is expected to drastically increase SNR, resolution and susceptibility contrast, which improves lesion detection and quantifications. Also the reduction of inherent T_1 relaxation time of contrast agent at high magnetic field is important to increase positively enhanced contrast with limited MR acquisition parameters.

The developed contrast agent used in this study was observed to maintain its favorable positive relaxivity even at 7 T magnetic field without drastic reductions of r_1 relaxivity. The developed contrast agent was characterized by this phantom and *in vivo* experiments. The results of 3D MRA proved the feasibility of vascular imaging within 2 hours after intravenous injection of the contrast agent. And a significant reduction of T_1 values was observed in the tumor region 7 hours after contrast agent injection in the tumor mouse model.

Contents

List of figures

List of tables

Chapter 1. Introduction

1.1 Purpose

The aim and content of this thesis can be summarized into two distinct subjects. One is to verify and develop the feasibility of dual contrast by using superparamagnetic iron oxide nanoparticles (SPION) in *in vivo* applications. Furthermore, the information of dual contrast in MRI is used for compensation of their inherent drawbacks. The other is to evaluate and characterize the developed contrast agent through both *in vitro* and *in vivo* experiments.

The detailed objectives of the research are as followings:

First section includes the below topics,

(1) Dual MRI T_1 and T_2^* contrast with size-controlled iron oxide

(2) UTE–ΔR_2–ΔR_2^* combined MR whole-brain angiogram using dual-contrast superparamagnetic iron oxide nanoparticles

Second section includes the topic below,

(1) Lumazine Synthase Protein Nanoparticle-Gd(III)-DOTA Conjugate as a T_1 contrast agent for high-field MRI

1.2 Outline

This thesis is organized as follows:

Chapter 2 introduces the background of this thesis. In this section, the physiochemical characteristic and bio-distribution of SPION is introduced to understand how SPION can be utilized in MRI. Then, the basics of MRI were explained and introduced for understanding fundamental concept. And, the essential concepts of used pulse sequences in this study for 3D MR imaging were presented to comprehend results of this research in later chapters. Especially, emphasis is placed on describing the principles of the FLASH, TSE, and radial UTE techniques for 3D imaging. Finally, the MR angiography (MRA) in MRI is described to understand features of contrast enhanced vasculature images by various MRA methods.

Chapter 3 is focused on describing the development and application of dual contrast MRA, employing concentration of SPION and pulse sequence techniques. The simulation and optimization of maximizing dual contrast effect for the *in vivo* applications are investigated. Furthermore, the application of dual contrast implements into the rodent's brain and resultant MRAs of dual contrast enhanced brain was combined for raising their strengths. The quantification of vascular parameters was also performed

to verify advantage of dual contrast enhanced combined MRA.

Chapter 4 is about evaluation and characterization of developed contrast agents. The experiment strategies of newly developed contrast agents were systematically established to verify the usefulness as T_1 contrast agent. Developed contrast agent could be successfully applied as a positive T_1 contrast agent at high field and utilized as a high-resolution vascular imaging agent within 2 hours after contrast agent injection. It also demonstrated that developed contrast agent was consistently flowed into the region of the tumor for a long time after injection.

Chapter 5 will provide the summary and conclusions of thesis work.

1.3 Abbreviations

BOLD	Blood oxygen level-dependent
BV	Blood volume
BW	Body weight
CE	Contrast enhanced
CPMG	Carr–Purcell–Meiboom–Gill
DLS	Dynamic light scattering
DMEM	Dulbecco’s modified eagle medium
ETL	Echo train length
FA	Flip angle
FBS	Fetal bovine serum
FLASH	Fast low-angle shot
FOV	Field of view
FPM	Finite perturber method
HWHM	Half-width at half-maximum
IACUC	Institutional animal care and use committee
IRSE	Inversion recovery spin echo
MC	Monto carlo
MEGE	Multi echo gradient echo
MION	Monocrystalline iron oxide nanoparticles
MIP	Maximum intensity projection
MRA	MR angiography
MRI	Magnetic resonance imaging
MSME	Multi slice multi echo
NA	Number of averages

NR	Number of repetitions
PBS	Phosphate buffered saline
PS	Penicillin–streptomycin
RARE	Rapid acquisition with relaxation enhancement
ROI	Region of interest
SD rat	Sprague-Dawley rat
SNR	Signal to noise ratio
SPION	Superparamagnetic iron oxide nanoparticles
TE	Echo time
TEM	Transmission electron microscope
TI	Inversion time
TR	Repetition time
TM	Temporalis muscle
TIR	Turbo inversion recovery
TSE	Turbo spin echo
USPIO	Ultra-small superparamagnetic iron oxide
UTE	Ultra-short echo time

Chapter 2. Background

2.1 Superparamagnetic iron oxide nanoparticles

Superparamagnetic iron oxide nanoparticles (SPION) can reduce proton relaxation as contrast agents and have been used for extensive research over the past decade. This topic provides the chemical and biological features of SPION as contrast agent for *in vivo* magnetic resonance image (MRI) application. The SPION among various MRI contrast agents has been recently used to obtain MR angiograms for imaging the vasculature by using their smaller size, prolonged blood circulation time and suitable MR relaxivities. Generally, SPION is characterized to have appropriate and consistent diameter of less than 50 nm and maintain a high longitudinal and transverse relaxivity [1]. Due to their higher relaxivities and relatively long half-life, SPION can be utilized to well evaluate characterization of vasculatures without repetitive injections on follow-up MR imaging studies [2].

The structure of SPION was made of mixtures of ferrous (Fe_2^+) and ferric (Fe_3^+) salts usually with the incorporation of ammonium compounds [3]. Superparamagnetic property was occurred by regions of unpaired spins. Single domain particles with unpaired spins are named magnetic domains as shown in **Figure 2.1.1**. A net of magnetic dipole in magnetic domain is greater than the total unpaired electrons. So, these particles have paramagnetic features. When magnetic field does not apply to magnetic domains, these domains are rotated freely by thermal energy, and positioned randomly. In the existence of the main magnetic field, the magnetic dipoles in magnetic domain are oriented with direction of the main magnetic field. When the main magnetic field is terminated, the net of magnetic moments becomes zero and re-positioned randomly [4].

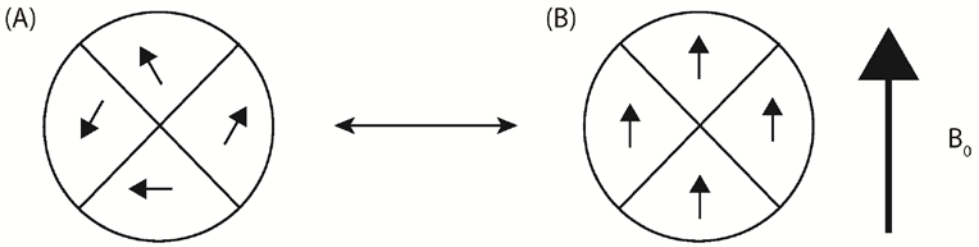

Figure 2.1.1 Magnetic domains in absence and presence of main magnetic field. (A) The image of magnetic domain in the absence of the main magnetic field, (B) The image of magnetic domain in the presence of the main magnetic field.

The longitudinal and transverse relaxation effect of SPION is related to protons. The longitudinal relaxation requires a dipole-dipole interaction. The interactions appear between the protons of water molecules and a paramagnetic contrast agent. The distance factor is important for dipole-dipole interaction. Explain briefly, if the distance of the paramagnetic ion species and the water molecule is close, the relaxation effect will be strong. In other words, the correlation time between the water proton and the paramagnetic ion is important.

The process of transverse relaxation depends on stationary or slowly fluctuating fields. When individual magnetic dipole is fluctuated slowly in local magnetic field, the small changes of magnetic field will lead to a different resonance frequency. Although the net magnetization still has the same frequency, the phase information of individual magnetic dipole differs in the transverse plane. Especially, SPIONs provide large variation of magnetic field and the dipolar coupling between water protons and magnetic dipole cause de-phasing effect [5].

In blood, iron oxide nanoparticles with the appropriate composition can produce significant signal enhancement and numerous experiments have studied for the use of these nanoparticles in MR angiography (MRA). Most of iron oxide nanoparticles are intravascular contrast agents. The proper size of iron oxide particles aids to continuous flow in vessels without purification and penetration. Intravascular contrast agents have a large molecular weight to prevent leakage from the vascular to the intravascular space. Most of contrast agents after injection circulate in the blood vessels and simultaneously escape and disappear by the process of phagocytosis of macrophages in the reticuloendothelial system, which is included of the lymph nodes, spleen and liver. After SPION injection, the reaching steady-state time was less than 10 min and SPION is slowly phagocytosed by macrophages for several hours or days. As a result, SPION was considered as suitable blood pool contrast agents during the first-pass and steady state phase of imaging [6].

In this study, in-house SPION was synthesized, which was also called monocrystalline iron oxide nanoparticles (MION). Generally, this SPION was widely used as T_2-contrast agent for MR lymphography, detection of tumor, and infarctioned tissue detection in the pre-clinic field. The core size distribution of the SPION is 5–10 nm. The in-house SPION do not leakage though undamaged vascular endothelial into the interstitial space and was less affected by the process of phagocytosis of macrophages due to their proper size. The concentration of in-house SPION in the blood vessels was maintained until 8 hours after the injection of in-house SPION by observed experimental result. We typically observe that in-house SPION clears off from brain vessels after ~3 days.

Since the synthetization of the first SPION over decades ago, FDA approved SPION have been utilized as a contrast agent in clinical field. The representative FDA approved iron oxide was Ferumoxytol. This contrast agent is relatively safe to apply in clinical field and is not related with any risk unlike gadolinium chelates. Although in-house SPION is not well known about the safety profile, the safety evidence

of Ferumoxytol is guaranteed that in-house SPION also has a low risk for application of *in vivo* imaging [7].

This in-house SPION has been used in research field over many years. Especially, the existence of SPION in brain produces interference of local magnetic field and growth the transverse relaxation rates. By using spin and gradient echo, regional blood volume distributions and change of pharmacological manipulation and functional activation in the brain of small animal can be extracted. Also, vessel density and size of micro-vasculature potentially expected by using SPION [8]. Dynamic susceptibility contrast (DSC) which was one of the most generally used techniques for MRI perfusion can be used by using a bolus of SPION contrast agent passing through a capillary bed [9].

2.2 T_1 and T_2/T_2^* relaxation

MRI system consists of three main parts; a main magnet field, three gradient field and transmit/receive coil. Based on three main parts, MR signals are generated for obtaining MR images. A main magnetic field is existed across the object along the direction of the bore of the magnet. When the strong magnetic field is applied, water protons attempt to align with or against the main magnetic field. The slightly more protons are aligned with main magnetic field, the object has net magnetization vector in the same direction as the main magnetic field [10-12].

As shown in **Figure 2.2.1**, the magnetic field vector B_0 and z axis are parallel each other. The net magnetization of any material is also aligned with z axis by main magnetic field. When magnetic field caused by radiofrequency (RF) pulse is applied to magnetization vector by the transmit coil, the magnetization vector moves down toward the transverse plane.

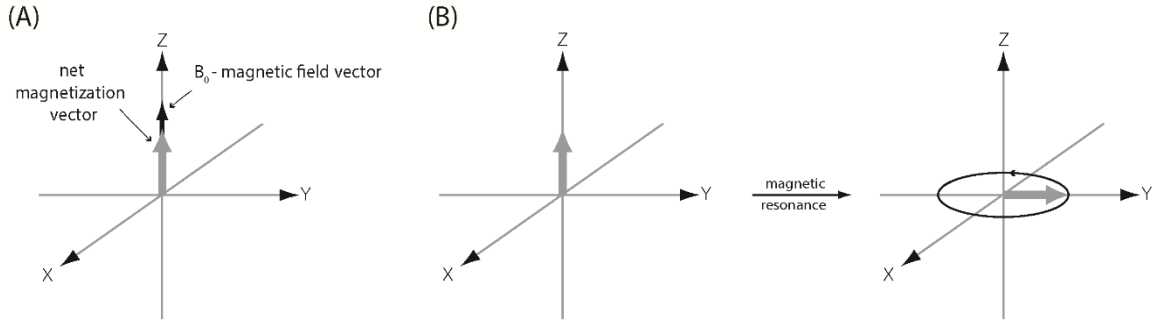

Figure 2.2.1 Magnetization vector before and after applied RF magnetic field. (A) The image of magnetization vector before applied RF magnetic field, (B) The image of magnetization vector after applied RF magnetic field.

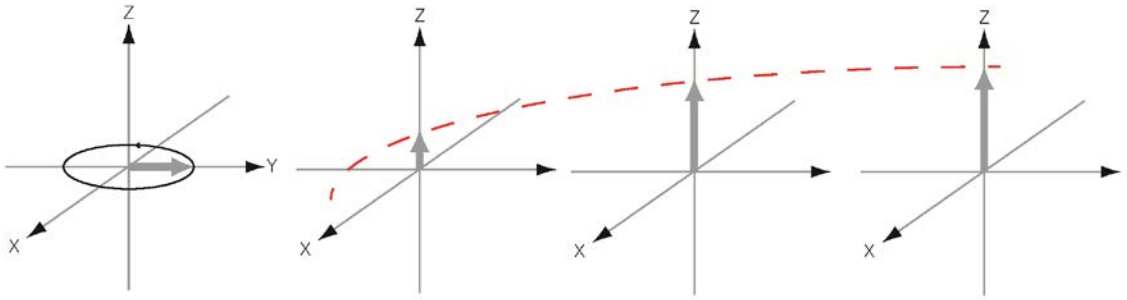

Figure 2.2.2 T_1 relaxation of magnetization vector after applied RF magnetic field.

After the RF pulse, the net magnetization vector starts to return back to its equilibrium state. This process is known as relaxation and MR signals are generated during the relaxation process. There are two kind of relaxation processes and these processes relate to the longitudinal and transverse components of the net magnetization vector. The first process of relaxation is called by T_1 relaxation and also known as spin-lattice relaxation. The 'lattice' relates to the surrounding material. T_1 relaxation depends on effective energy exchange between proton and its surroundings. Some water molecules are at the suitable speed for effective energy transfer. The pure water has a very wide distribution of natural speed. If those water molecules are large, the water molecules slow down and exchange the energy more efficiently. The magnetization vector along the longitudinal axis recovers to its equilibrium value as shown in **Figure 2.2.2** [13].

The second relaxation process is related to the decay of the magnetization vector on the transverse component as it rotates about the z axis. The rotation speed of molecular is important for T_2 relaxation. T_2 relaxation is related to spin-spin relaxation because effects of one 'spin' can transfer another. Adjacent protons act as small magnet moment and exist slight effects on their neighbors. For example, the iron oxide is ferromagnetic material and generates magnetic field. The existence of a neighboring proton will affect the local magnetic field. And tissue-air interfaces also add to inhomogeneity in the magnetic field. This will be a bias on the local magnetic field and change the resonance frequency of that proton, and thus leads to T_2 dephasing.

In transverse plane, the angle of each magnetic moment at any direction is defined as the phase angle. When magnetic moments have similar phase angles, the state is called by in phase. Over time, the magnetic moments of in phase state loss their coherence and move with different rotate velocity. This state is named as out of phase. The net magnetization is decreased by different phase angle of magnetic moments. Consequently, the magnetization vector on the transverse component is gradually reduced and the measured MR signal also gradually decays.

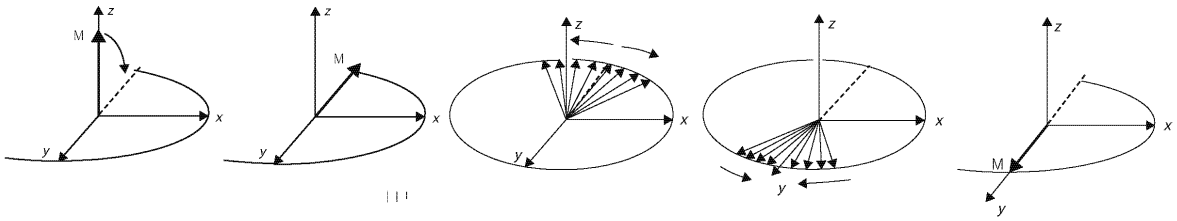

Figure 2.2.3 T_2 relaxation of magnetization vector on the transverse plane after applied RF magnetic field.

The transverse relaxation is divided into T_2 and T_2^* relaxation. Firstly, T_2 relaxation is affected by the presence of interactions between neighboring protons. These interactions of protons occur different phase angle of magnetic moments. The de-phasing of magnetic moments in T_2 relaxation is irreversible and T_2 relaxation time is slightly short than T_1 relaxation time. As shown in **Figure 2.2.3**, each magnetic vector on transverse plane was spread out as time goes. If 180° pulse is applied to spin system after 90° pulse, the de-phasing effect by external factors can be compensated.

The second source for the de-phasing relates to local in-homogeneities in the applied magnetic field as shown in **Figure 2.2.4**. These inhomogeneities may be susceptibility-induced field distortions produced by the materials. The magnetic moments at different spatial locations will rotate at different rates. This transverse relaxation is called as T_2^* relaxation and de-phasing effect is greater than T_2 relaxation. So the MR signal decays more rapidly and T_2^* relaxation processes is written by:

$$\frac{1}{T_2^*} = \frac{1}{T_2} + \frac{1}{T_{2i}} \qquad (2.2.1)$$

where $1/T_{2i}$ is the change of relaxation time by inhomogeneities. Gradient echoes are produced by the controlled magnetic field gradients. The losing coherence or de-phasing of proton rapidly change by gradient magnetic field along the one direction. The amount of de-phasing can be compensated by one reversed gradient magnetic field along the opposite direction with a slope of equal amplitude. When the same amount of time as the first gradient is applied as the second gradient along the opposite direction, the de-phasing caused by the first gradient is annulled and the MR signal reappears. It reaches a maximum amplitude of MR signal at the point by the first gradient have returned back into phase. This result is called as re-phasing. If the second gradient is applied to the spin system continually, the MR signal disappears. The re-phasing of signal occurs by the switching of the gradient direction is known as a gradient echo [14].

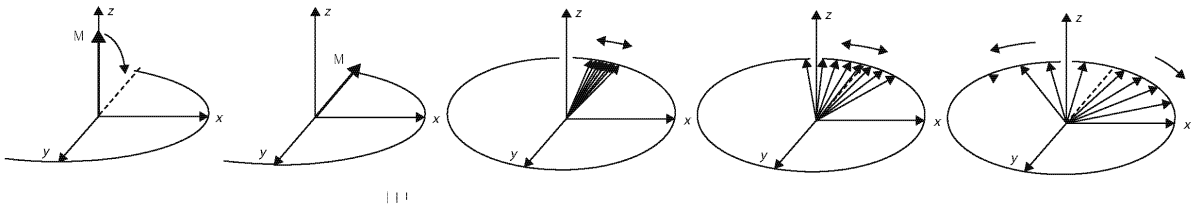

Figure 2.2.4 T_2^* relaxation of magnetization vector on the transverse plane after applied RF magnetic field.

Longitudinal and transverse relaxation both occur at the same time. The MR signal can be detected as the form of an echo by using pulse sequences and its MR parameters. As shown in **Figure 2.2.5**, the time peak of the MR signal after 90° excitation pulse was defined by echo time (TE). MR parameter of echo time (TE) and repetition time (TR) determine T_2 and T_2^* relaxation effects. The time between excitation pulse and subsequent excitation pulse refers to repetition time. It controls how much magnetization vector of longitudinal component recovers between each excitation pulse.

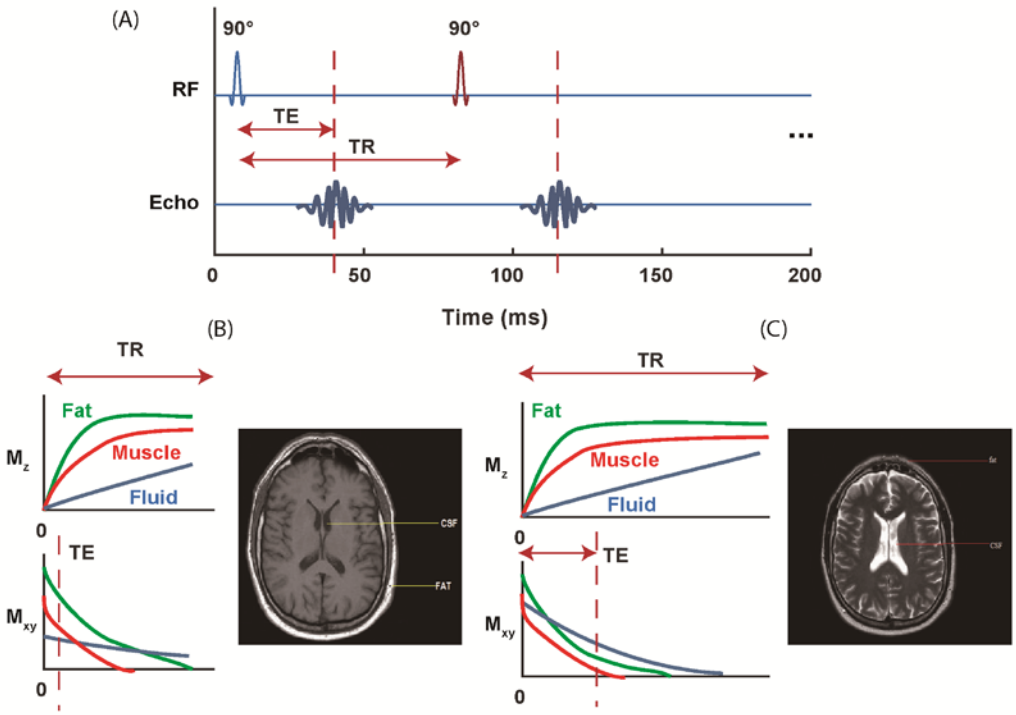

Figure 2.2.5 The T_1-weighted and T_2-weighted images which were generated by echo. (A) The general pulse diagram with TE and TR, (B) T_1-weighted image with a short TR and short TE, (C) T_2-weighted image with a long TR and long TE.

As shown in **Figure 2.2.5B** and **C**, the MR parameters for T_1-weighted echo are a short TR and short TE. The short TR allows that fluid with a long T_1 will recover less than fat with a short T_1. When the subsequent excitation pulse is applied, the initial value of the transverse magnetization was determined. The short TE suppresses the influence of the T_2 relaxation. The images with short TE and short TR are said to be T_1-weighted image. T_1 weighted images are typically characterized by bright fat signal and a low signal from fluid.

The MR parameters for T_2-weighted echo are long TR and long TE. The long TR determines that the magnetization vector of longitudinal component to recover close to the its equilibrium values and the T_1 effect was minimized. The long TE allows the decay of the transverse magnetization component. The different decay rates of a fat with a short T_2 and a fluid with a long T_2 represent to difference of signal intensity. Acquired images was called as T_2-weighted image. The short T_2 induces low signal intensity, while the long T_2 induces high signal intensity. These images are characterized by bright fluid signal and a low fat signal.

2.3 Bloch equation

The magnetization vector can be calculated by a sum of each magnetization vectors as below equation [15]:

$$M(t) = \sum_{j}^{N} \mu_j(t) \qquad (2.3.1)$$

The below equation describe relaxation and precession of magnetic vector in three dimensional (3D) space.

$$M(t) = \; M_x(t)e_x + \; M_y(t)e_y + \; M_z(t)e_z \qquad (2.3.2)$$

The equation also can be represented as form of differential equation.

$$\frac{dM(t)}{dt} = \; \omega(t) \times \; M(t) - [R][M(t) - M_0] \qquad (2.3.3)$$

where

$$\omega(t) = -\gamma(1-\sigma)B(t)$$

$$M_0 = M_0 e_z, \qquad [R] = \begin{bmatrix} 1/T_2 & 0 & 0 \\ 0 & 1/T_2 & 0 \\ 0 & 0 & 1/T_1 \end{bmatrix}$$

This equation is called as Bloch equations. The term of $[R][M(t) - M_{eq}]$ in the Bloch equation implies the increase of longitudinal magnetization and decay of transverse magnetization relaxation. The term of $\omega(t) \times M(t)$ implies the variation of magnetization vector about the magnetic field direction. In other words, the magnetization vector M(t) precesses about the arbitrary direction of the vector $\omega(t)$ with an arbitrary frequency of precession.

In laboratory frame, magnetization vector appears to rotate with opposite direction. And the magnetization vector appears stationary in the rotating frame. In the rotating frame, the magnetization vector is described easily because of stationary state and exact frequency of precession. So the magnetization vector in the rotating frame is described as the Bloch equation transforms.

$$\frac{d^* M(t)}{dt} = \omega_{eff}(t) \times M(t) - [R][M(t) - M_0] \quad (2.3.4)$$

where the magnetization vector in the rotating frame precesses about a direction with a lower precession frequency given by

$$\omega_{eff}(t) = \omega(t) - \omega_{rot} \quad (2.3.5)$$

The ω_{rot} describes instantaneous vector in the rotating frame. The rate of change for the magnetization vector components in the rotating frame can be calculated. When the static magnetic field applied alone, the precession of magnetization vector can be represented in the static and an oscillating magnetic field. In the existence of a static magnetic field, the precession frequency in the rotating frame will be

$$\Omega = \omega_0(1 - \sigma) - \omega_{rot} \quad (2.3.6)$$

and the solution of Bloch equation in the rotating frame is described by:

$$\begin{bmatrix} M_x^*(t) \\ M_y^*(t) \\ M_z^*(t) \end{bmatrix} = \begin{bmatrix} [M_x^*(0) cos\Omega t - M_y^*(0) sin\Omega t] e^{-t/T_2} \\ [M_y^*(0) cos\Omega t - M_x^*(0) sin\Omega t] e^{-t/T_2} \\ M_z^*(0) e^{-t/T_1} + M_{eq}(1 - e^{-t/T_1}) \end{bmatrix} \quad (2.3.7)$$

where M_x^*, M_y^*, and M_z^* are the components of magnetization vector in the rotating frame. The components of magnetization vector transform from Cartesian basis to spherical basis vectors.

$$M(t) = M^*_{+1}(t)e^{+1} + M^*_0(t)e^0 + M^*_{-1}(t)e^{-1} \quad (2.3.8)$$

Where

$$e^{\pm 1} = \mp\frac{1}{\sqrt{2}}\left(e^*_x \mp ie^*_y\right), e^0 = e^*_z$$

$$M^*_{\pm 1} = \mp\frac{1}{\sqrt{2}}\left(M^*_x \mp iM^*_y\right), M^*_0 = M^*_z$$

The magnetization vector which is applied by rf pulse described in terms of the spherical basis components.

$$\begin{bmatrix} M^*_{+1} \\ M^*_0 \\ M^*_{-1} \end{bmatrix} \rightarrow \begin{bmatrix} \frac{1}{2}M^*_{-1}e^{i2\phi} - \frac{i}{2}M^*_0e^{i\phi} + \frac{1}{2}M^*_{+1} \\ \frac{1}{\sqrt{2}}M^*_{-1}e^{i2\phi} \qquad\qquad - \frac{i}{\sqrt{2}}M^*_{+1}e^{-i\phi} \\ \frac{1}{2}M^*_{-1} - \frac{i}{\sqrt{2}}M^*_0e^{-i\phi} + \frac{1}{2}M^*_{+1}e^{-i2\phi} \end{bmatrix} \quad (2.3.9)$$

A single 90° pulse with x axis generates the MR signal. This MR signal can be detected by form of the complex magnetization component M^*_{+1} in the rotating frame. The progress of the magnetization vector by the 90° pulse is as follows:

$$M = M_0e_0$$

$$\downarrow \left(\frac{\pi}{2}\right)_x$$

$$M^+ = -M_0e_y = \frac{i}{\sqrt{2}}M_0e^{-1} + \frac{i}{\sqrt{2}}M_0e^{+1} \quad (2.3.10)$$

$$\downarrow \text{free evolution}$$

$$M(t) = \frac{i}{\sqrt{2}}M_0e^{-i\Omega t}e^{-\frac{t}{T_2}}e^{-1} + M_0(1 - e^{-t/T_1})e_0 + \frac{i}{\sqrt{2}}M_0e^{-i\Omega t}e^{-t/T_2}e^{+1}$$

The description of magnetization vector is obtained from the excited spins with relaxation mechanism of a longitudinal and transverse component by the variation of the oscillating RF magnetic field. Based on solution of Bloch equation, the MR signal can be detected by properties of T_1, T_2, and T_2^*.

2.4 Measurement of T_1 and T_2/T_2^* relaxation time

In the T_1 relaxation mechanism, the magnetization vector is flipped down on transverse plane and then the time is observed magnetization vector recovery back to its equilibrium state. The inversion recovery (IR) experiment of measurement T_1 relaxation time is the gold standard method as shown in **Figure 2.4.1**. This IR experiment can be used to obtain the general behaviors of T_1 relaxation time by using the IR pulse sequence [16]. After 180° pulse is applied to spin system, the longitudinal magnetization will recover back to its equilibrium value. The excitation of magnetization can measure the MR signal intensities at the different inversion times (TI). To exact measure T_1 relaxation time, TR is set 5 times of T_1 relaxation time to recover fully longitudinal magnetization [13].

The magnetization vector in the IR experiment was switched from the -z axis to the +z axis. The magnetization vector recovers back to the +z axis during a T_1 period. According to the Bloch equation, the validation of magnetization vector about a z axis will be

$$\begin{aligned} M_z(t) = \; & M_0\left(1 - e^{-\frac{TI}{T_1}}\right) + M_z(0)e^{-\frac{TI}{T_1}} \\ = \; & M_0\left(1 - e^{-\frac{TI}{T_1}}\right) + M_0(0)e^{-\frac{TI}{T_1}} \quad (M_z(0) = M_0(0)) \\ = \; & M_0\left(1 - 2e^{-\frac{TI}{T_1}}\right) \end{aligned} \qquad (2.3.11)$$

The signal intensities of longitudinal magnetization were given by a function of TI point. The longitudinal magnetization was grown proportionally at different TI time. The signal intensity at the long TI is close to the equilibrium value of magnetization.

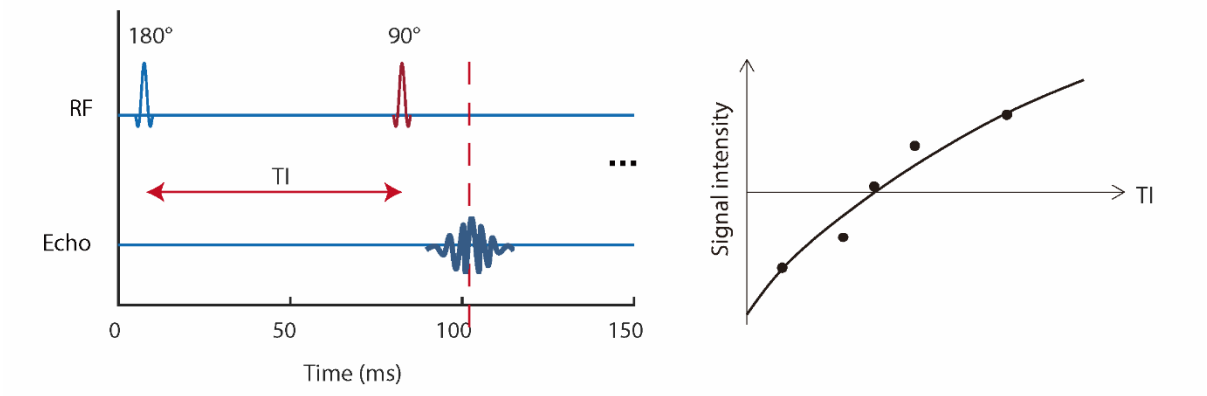

Figure 2.4.1 The signal intensities with TI by using the IR pulse sequence. The experimental data curve of signal intensities was fitted by theoretical equation.

The CPMG method is widely used for T_2 measurement. As shown in **Figure 2.4.2**, 90° pulse is applied to initial state of the spin system. The magnetization vector is flipped down on the transverse plane and the de-phasing of transverse magnetization begins. By using then 180° pulse, the magnetization is inverted into the transverse counter plane. The re-phasing of magnetization is progressing and producing a signal called an echo. The signal intensities at the different TE was fitted by theoretical equation. We can calculate relaxation time. Instead of 180° pulse, the de-phase and reverse gradient is used for T_2^* measurement.

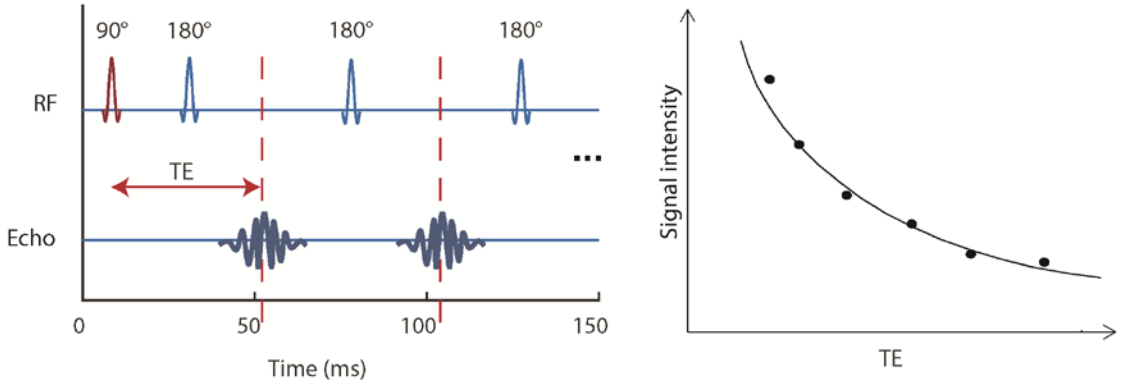

Figure 2.4.2 The signal intensities with TE by using the CPMG pulse sequence. The experimental data curve of signal intensities was fitted by theoretical equation.

2.5 Three-dimensional (3D) Magnetic Resonance Imaging

To generate reliable MR images, the whole k-space was filled by signals with spatial frequencies. For Cartesian acquisition, the signals which is affected by gradient field were equally spaced in k-space. As shown in **Figure 2.5.1**, the MR signals with phase encoding gradient were filled in the k-space. The amplitude of the phase encoding gradient is increased in each line of k-space and next adjacent line in k-space is filled with each successive repetition. This is known as a linear phase encoding order [17].

To obtain a whole range of the k-space, the MR signals are acquired multiple times with different step by using phase encoding gradient. The acquisition time is given by phase encoding step and TR. In 3D MR imaging, the whole range of object is excited by pulse and two phase encoding gradients are applied with two directions. The echoes from pulse excitations in 3D k-space were needed more to make a complete volume compared with two dimensional (2D) in the Cartesian coordinate system. In other words, the acquisition signals in spatial encoding of 3D k-space were added along the phase encoding direction which was consisted of the second and third phase dimension unlike accumulation along the

only one phase encoding direction in 2D k-space. So the acquiring the 3D k-space takes a long acquisition time due to a number of echo for 3D k-space.

In spite of long acquisition time, there are several reasons for choosing 3D rather than 2D acquisition from the point of view of a MRA. The images with a 3D acquisition provides higher signal to noise ratio (SNR) because the signal from each volume element is integrated over the whole scan as opposed to images with 2D. The 3D acquisition also permits higher spatial resolution with isotropic or non-isotropic voxels than 2D resolution. Especially, a relatively small vessel structure in the 3D imaging was depicted well regardless of vessels orientations and flow effects by comparing with 2D imaging [18].

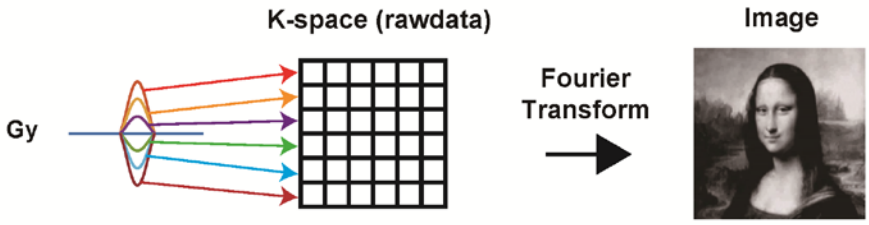

Figure 2.5.1 A k-space with linear phase encoding and image by Fourier transformation.

The MR images were acquired by converting measured k-space of the complex values signal by using the Fourier transform. And the analytical expression for converting MR signal into k-space is given as follow.

$$\boldsymbol{B}(\boldsymbol{r}) = \boldsymbol{B_0} + \boldsymbol{G} \cdot \mathbf{r} \qquad (2.5.1)$$

The static (B) and gradient magnetic field (G) in MRI system are mixed. Assumed that the relaxation is ignored, MR signal in the rotating frame is described as below equation.

$$S(t) = \iiint \rho(\boldsymbol{r}) e^{i\gamma \boldsymbol{G}\cdot\mathbf{rt}} dr \qquad (2.5.2)$$

where dr is volume integration of the object. The space vector k is described by

$$\mathrm{k} = \gamma \boldsymbol{G} \mathrm{t}/2\pi$$

The MR signal can represent as basis of k,

$$S(k) = \iiint \rho(\boldsymbol{r}) e^{i2\pi k \cdot \mathbf{r}} dr \qquad (2.5.3)$$

Based on k-space perspective, the volume integral of the signal is regarded as a Fourier transform of the magnetization density in real space. If S(k) is applied to inverse Fourier transform, images based on real space is obtained.

$$\rho(r) = \iiint S(\boldsymbol{k}) e^{-i2\pi k \cdot \mathbf{r}} dk \qquad (2.5.4)$$

In 3D space, gradient magnetic fields are applied to object along three orthogonal directions. The images in 3D space can be described by inverse Fourier transform of S(k) with three orthogonal directions.

$$\rho(x, y, z) = \iiint S(k_x, k_y, k_z) e^{-i2\pi(k_x \mathbf{x} + k_y \mathbf{y} + k_z \mathbf{z})} dk_x dk_y dk_z \qquad (2.5.5)$$

2.6 Signal equation

The MR signal was evaluated from the excited spins, which were evolved by precession and relaxation mechanism with a longitudinal and transverse component in the occurrence of the magnetic field variation. The evaluated MR signal may be weighted in many ways in order to extract useful information and was given by:

$$S = S_0 \frac{[1 - e^{-TR \cdot R_1}]}{[1 - \cos(\alpha) \cdot e^{-TR \cdot R_1}]} \cdot \sin(\alpha) \cdot e^{-TE \cdot (R_2^* \ or \ R_2)} \qquad (2.6.1)$$

where S is the steady-state signal intensity, S_0 indicates the equilibrium magnetization, α is flip angle (FA), R_1 is longitudinal relaxation rate and R_2 and R_2^* are transverse relaxation rate induced by spin and gradient echoes, respectively.

The steady state signal was affected by the MR imaging parameters such as FA, TE and TR with intrinsic longitudinal and transverse relaxation times. **Equation 2.6.1** is valuable to analyze the obtained image properties and optimize the imaging parameters. The specific parameters give several weighted signal. Signal is always proportional to spin density. A small flip angle minimizes T_1-weighting because of small recovery of the longitudinal magnetizations. Hence at small flip angles, proton density and T_2

or T_2^* effects predominate. When TR is small, exponential term becomes large and T_1-weighting increases.

As shown in **Figure 2.6.1**, proton density-, T_1- and T_2-weighted images were extracted from S_0, T_1 and T_2 maps of *in vitro* kidney sample by using simulation. To emphasis proton density of kidney, the MR parameters are set by long TR and short TE to minimize T_1 and T_2 relaxation effects. The map and image of proton density were similar. To obtain T_1-weighted image, the MR imaging parameters are set by short TR and short TE to minimize T_2 relaxation effects. The relation of high and low values of T_1 map and T_1-weighted image reversed. The T_1-weighted image shows that region with short T_1 appears bright and the region with long T_1 appears dark. To obtain T_2-weighted image, the MR imaging parameters are set by long TR and long TE to minimize T_1 relaxation effects. The T_2-weighted image shows that the region with short T_2 appears dark and the region with long T_2 appear appears bright.

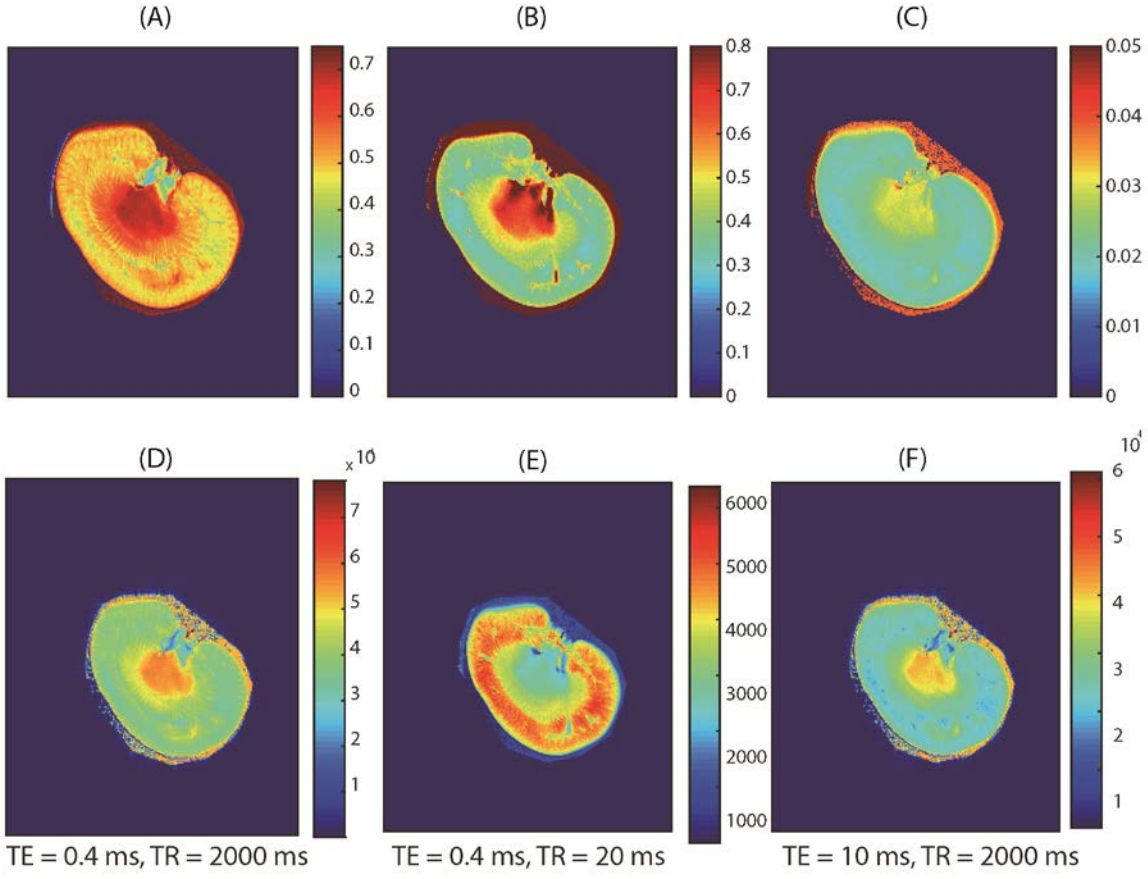

Figure 2.6.1 Simulation of proton density-, T_1- and T_2-weighted images. The maps of inherent (A) proton density, (B) longitudinal and (C) transverse relaxation time of *in vitro* kidney sample were used for obtaining the (D) proton density-, (E) T_1- and (F) T_2-weighted images.

2.7 Fast low-angle shot (FLASH) pulse sequence

The first pulse sequence for MRA imaging was 3D fast low-angle shot (FLASH) and this pulse sequence was generally used for T_2^* weighted image using gradient echo. The sequence diagram for 3D FLASH is shown in **Figure 2.7.1** [19]. In this pulse sequence, the proton density, T_1, and T_2^* contrast can be adjusted by using TE and TR maintaining the steady-state of the signal. T_1 contrast can be obtained with short TE and long TR. Also T_1 contrast can be enforced by removing the remaining echo contributions to the signal using spoiler gradients at the end of the sequence. With long echo times, T_2^* contrast becomes dominant.

The 3D FLASH was widely used for imaging vascular system though time-of-flight (TOF) MRA method with no contrast agent. Although several MRA techniques have been developed and used in clinical field, it still remains one of the most important methods for noninvasive MRA. However, in this study, 3D FLASH was utilized for obtaining contrast enhanced (CE) -MRA in order to enhance signal of the whole vasculature of object including slow flow vessels such as vein and capillary. The contrasts of CE-MRAs were determined by a kind of contrast agent and MR imaging parameters, which was dominated by echo time.

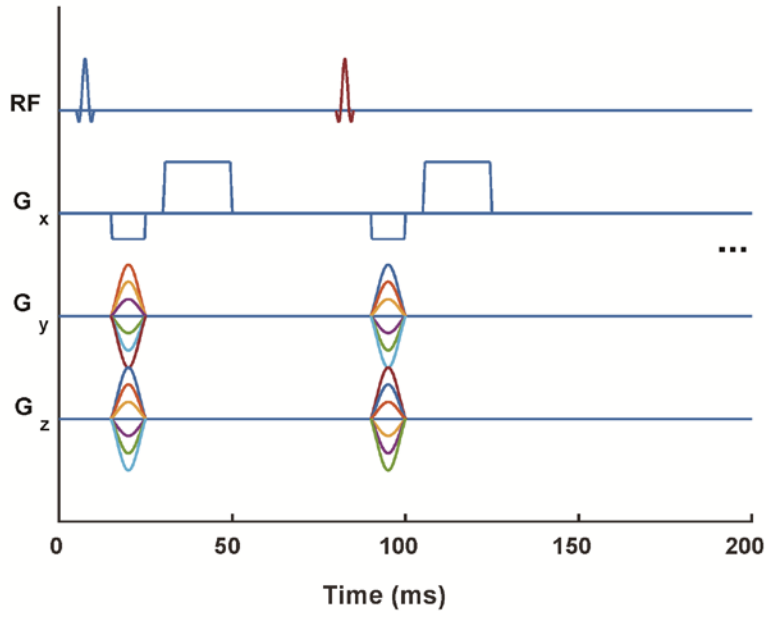

Figure 2.7.1 Pulse sequence diagram of 3D FLASH. The gradient echoes were used for obtaining optimal 3D k-space.

2.8 Turbo spin echo (TSE)

The turbo spin echo (TSE) is multiple spin echoes which were generated by using the CPMG sequence [20]. Each echo was used separately phase-encoded. The phase encoding is incremented within one echo train to accelerate the acquisition. It is possible to obtain two or more echo with different effective TEs. The schematic sequence diagram for TSE is shown in **Figure 2.8.1**.

Generally, the scan time of TSE can be shorted by the number of spin echo within TR. The number of spin echoes called RARE factor can accelerate the speed of scan time compared to the conventional spin echo imaging because of multiple phase-encoding lines are acquired during each TR interval. The RARE factor typically ranges from 4 to 32 for routine imaging, but may exceed 200 for rapid imaging/echo planar techniques.

Increasing the RARE factor reduces the scan time but typically increases the effective TE and the blurring caused by T_2 relaxation. On the other hand, turbo factor should be carefully selected because T_2 effect is inevitably contained at later echoes and associated imaging blurring artifacts may arise with echo train imaging without multiple spin echoes compensation

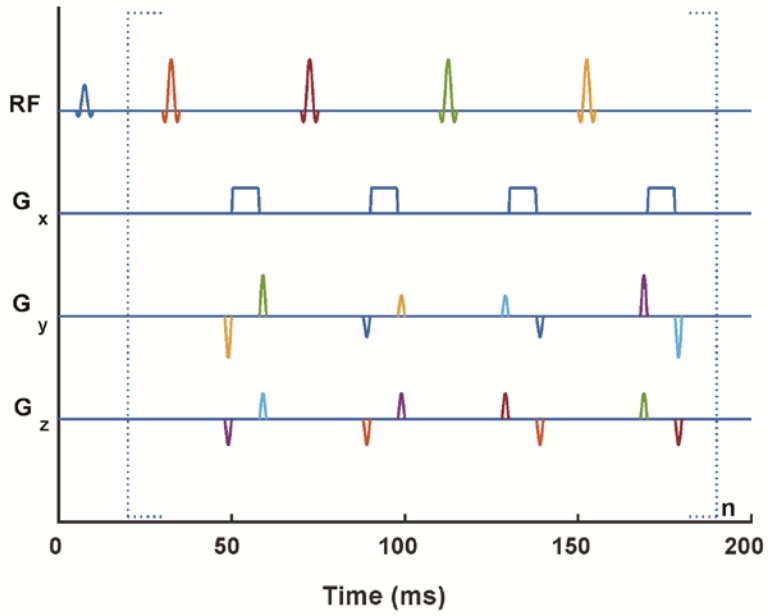

Figure 2.8.1 Pulse sequence diagram of 3D TSE. This example generates 4 echoes after 90° pulse. Each echo is encoded to the different position of k-space line.

2.9 3D Ultra-short echo time (UTE)

Ultra-short echo time 3D (UTE3D) is a 3D imaging sequence based on a ramp-sampled 3D radial acquisition combined with a RF excitation [21-24]. It allows visualization of objects having very short transverse relaxation times. The 3D implementation of the ultra-short TE technique (UTE3D) allows extremely short echo time because of the use of a non-selective RF excitation.

After a hard RF excitation pulse with low flip angle is applied, the responded echoes immediately were collected from the center of k-space on a half-radial trajectory by turning on imaging gradients in all three orthogonal directions as shown in **Figure 2.9.1** [25]. The minimum TE is limited only by the duration of the RF excitation pulse and the time is needed to switch between the RF excitation and the data acquisition.

An array method of k-space for 3D UTE imaging with high resolution was 3D radial center-out acquisitions. The 3D radial center-out trajectory provides the shortest possible echo times and also very insensitive against motion and flow artifacts due to its inherent flow compensation. Sampling is performed already on the rising gradient ramp and therefore starts always from the center of k-space and continues to the surface of a sphere. The number of scans and directions of the readout gradient for each scan is calculated to achieve an even distribution of the "end points" at the sphere with a density that is required by the field of view.

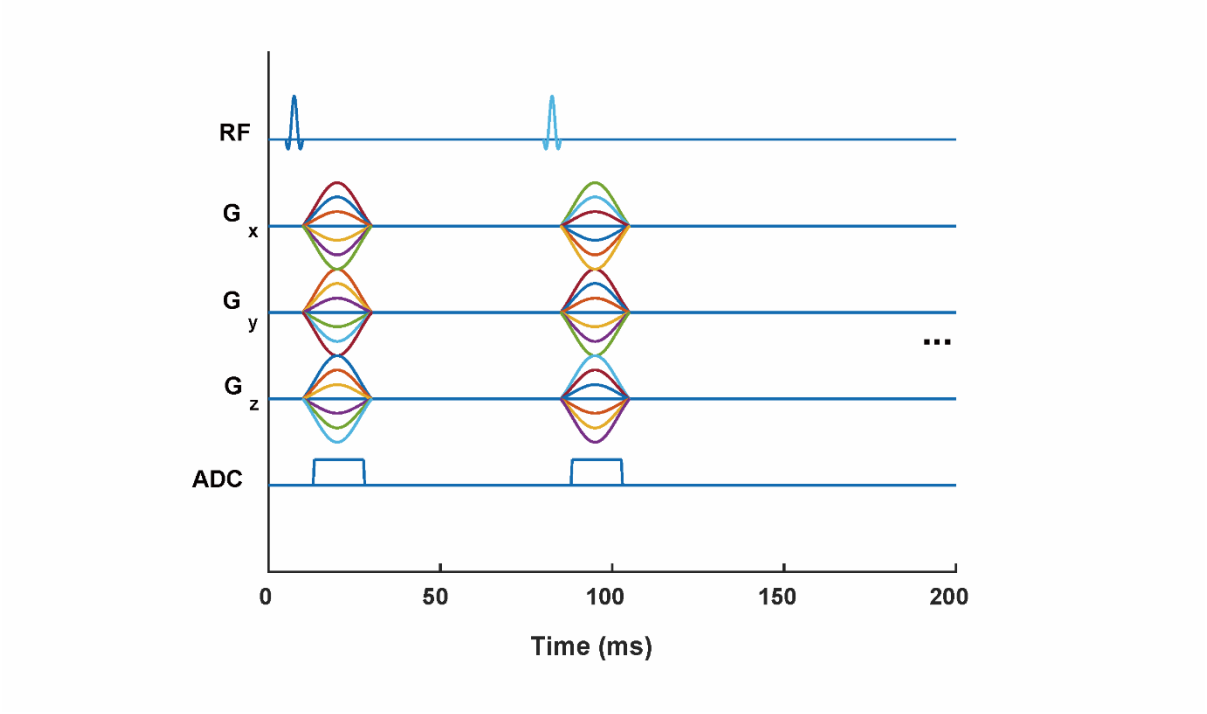

Figure 2.9.1 Pulse sequence diagram of 3D UTE.

As shown in **Figure 2.9.2**, radial k-space is converted into Cartesian k-space. So, the maximum signal was concentrated at the center of k-space because first echo after the excitation pulse was placed the center immediately. Before transverse magnetization was fully decayed, the signal with very short T_2^* was collected. So the UTE3D image from objects with very short T_2^* component has high signal intensity. One major drawback and corresponding advantage of this 3D radial acquisition method is the strong oversampling of inner k-space and down sampling in the outer k-space parts [26].

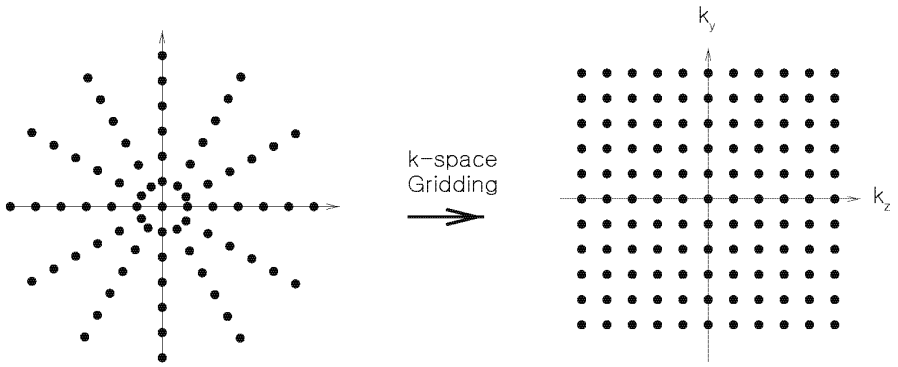

Figure 2.9.2 The radial k-space of 3D UTE and gridding method converting into Cartesian k-space.

2.10 Magnetic resonance angiography (MRA)

The fundamental MR angiography (MRA) has been used for obtaining vascular information such as vessel size and structure. For many decades, MRA techniques with contrast agent have been developed and implemented in research and clinical area for *in vivo* applications. Especially, the longitudinal (T_1) and transverse (T_2 or T_2^*) contrasts in MRA provide diverse and different information of same subject's vasculature. The assessments of vascular structure and function by using two types of contrast are important for monitoring vascular behavior [27, 28].

The TOF MRA as non-invasive MRI method has been used to visualize vasculature, this method provides only flow information within vessels such as arteries. This method is that back ground signal is suppressed by using slice-selective excitation pulses. In other words, the stationary tissue is saturated. The vessels with high flow velocity has strong signal intensity because incoming blood is free to the slice-selective excitation pulse. But the vessels with slow blood flow saturated by excitation pulse, those vessels have poor vessel visualization [29].

To visualize whole cerebral small vessels, CE-MRA was developed by using various MRI techniques. One of well-known CE-MRA methods is the use of T_1 contrast agent. T_1 contrast enhanced MRA with

contrast agent also tried to image vessels and has been successfully used to detect arteries and veins. The contrast agent used in CE-MRA is a compound containing gadolinium (Gd), which alters the T_1 property of the blood. The contrast agents are injected into a peripheral vein as a bolus. The vessel-to-tissue contrast is enhanced by a reduction in blood T_1 induced by injecting a contrast agent with 3D-gradient echo sequence, but the requirements for a fast acquisition, reasonable spatial resolution, and a high signal-to-noise ratio. And visualization of micro-vessels is limited by the lower vessel diameter than spatial resolution [30].

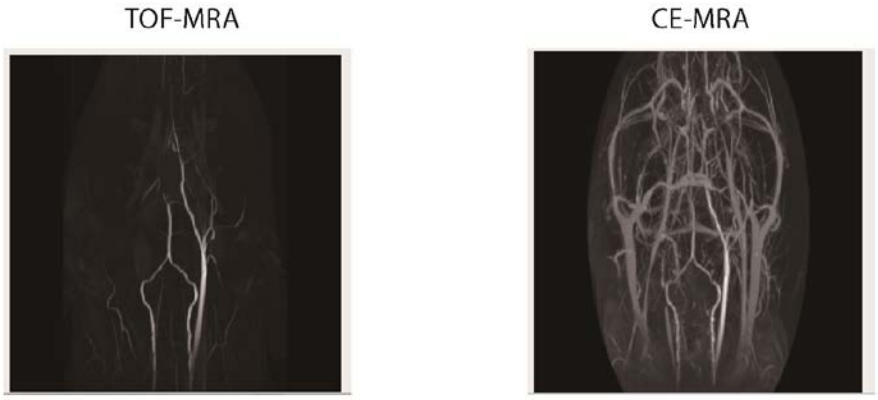

Figure 2.10.1 The rat head images of TOF- and CE-MRA.

Steady-state susceptibility contrast MRI is a contrast enhanced *in vivo* imaging technique that does directly visualize the vasculature and provides quantitative information about vascular morphology based on the behavior of the transverse magnetization [8, 31, 32]. The T_2 contrast agent creates magnetic field interference due to magnetic susceptibility ($\Delta\chi$) between the intra- and extra-vascular spaces. This difference in magnetic field affects water protons to precess at different Larmor frequencies and lead to loss of phase coherence. Consequently, the bulk transverse magnetization ultimately decays and transverse relaxation time decreases because of loss of phase coherence. Resultant MR signal decay by reduced transverse relaxation time is characterized by the transverse relaxation rate constants R_2 (for a spin echo experiment) and R_2^* (for a gradient echo experiment), respectively. The steady-state susceptibility contrast in these transverse relaxation rates (ΔR_2 and ΔR_2^*) rely on vascular morphology, the diffusion coefficient of water, and the characteristic frequency shift created by the intravascular contrast agent.

Recently, MRA with blood oxygen level-dependent (BOLD) effect was developed and widely used to visualize venous vessels [33, 34]. Using the gradient echo pulse sequence, the BOLD effect caused by changes of paramagnetic deoxyhemoglobin (dHb) in vessels. The hypo-intense venous signals were

detected and modulated by changing oxygen concentrations in inhaled gas. BOLD signal contrast also can describe the micro-vessel to magnify vessel size due to the susceptibility effect. The BOLD signal contrast was differently revealed by using spin echo and gradient echo [35]. Recently, MRI angiographic technique by using the BOLD effect investigate under specific level of carbogen (5% CO_2 + O_2) inhalation and is called by 3D gas ΔR_2^*-mMRA. In this method, veins and venules are revealed well and have high vessel-to-tissue contrast. When applied to studying post-stroke revascularization, the method vividly reveals the microvascular remodeling changes at 3 days after reperfusion [36].

Chapter 3. Dual contrast MRI with iron oxide nanoparticles

3.1 Dual MRI T_1 and T_2^* contrast with size-controlled iron oxide

3.1.1 Introduction

A number of MRI techniques have been developed and improved to obtain diagnostic imaging of abnormal vasculature and its function in neurological and oncological diseases [37, 38]. Selectively enhanced contrast of vascular signal with suitable blood pool MRI contrast agents improves quantitative analysis efficiency of related vascular parameters. Conventionally, a T_1-based positively enhanced contrast has been applied to extract conspicuous angiogram by enhancing signal intensity of intravascular region. T_2- and T_2^*-based negatively enhanced contrasts have been using to quantify vascular parameters and to realize hemodynamic effects [39-41]. Selecting the suitable contrast agents and the proper MRI strategies helps to evaluate relevant vascular parameters [42].

There are two types of intravascular MRI contrast agents for enhancing dual contrast using T_1 or T_2^* shortening mechanism. Generally, paramagnetic solution including gadolinium or manganese ion was used for obtaining positively enhanced contrast by shortening T_1 relaxation time [43-45]. On the other hand, SPION provides negatively enhanced contrast by dephasing effect in the susceptibility-induced inhomogeneous magnetic field [46, 47]. Actually, positively and negatively enhanced contrasts in MRI were affected to each other with strengths and drawbacks. The positively enhanced contrast offers spatial accuracy of MR signal which was induced by contrast agent but loses high CNR. In contrast, the negatively enhanced contrast increases CNR with high sensitivity, but lacks the position information of contrast agent.

To use positively and negatively enhanced contrast for vessel quantification, the SPION has been used recently as T_1 contrast agent because of the appropriate relaxivities and size of nanoparticle [28, 48-50]. As for point of intra-vascular contrast agent, characteristics of SPION are long circulation time in blood vessel and impermeability between intra- and extra-vasculature. The recent studies are shown that T_1 contrast agent was applied to obtain MRA with high resolution and to measure accurate evaluation of vessel parameters such as vessel branches, blood volume (BV) and average of vessel diameters [51, 52]. In this regard, it is possible that the errorless description of the SPION MRA with positively enhanced contrast provides increased MR image quality and accurate quantification.

For obtaining diagnostic accuracy and sensitivity, the MRI techniques of describing vasculatures using negatively and positively enhanced contrast have been conducted [53-57]. Especially, the hybrid nanoparticles have been synthesized to improve the ability of acquiring dual contrast [58, 59]. However, the

synthesis methods technically limited to quantify vascular parameters because the use of multiple contrast agents is likely to arise undesirable effects such as bio-distribution and unexpected doses in *in vivo* experiments. [60-62].

In this study, we verified the dual contrast effects of size-controlled exogenous SPION at specific MR imaging parameters. We also validated that both feasibility and benefits of the dual contrast T_1- and T_2^*-mode MR imaging through simulation results and comparison of longitudinal *in vivo* experiments. Instead of synthesizing the hybrid contrast agents, we used manipulation of pulse sequence and concentration of SPION for acquiring dual contrast of vascular signal. Despite of well-known ability of negatively enhanced contrast of SPION, this iron oxide nanoparticle can be effectively used for obtaining of positively and negatively enhanced contrasts simultaneously.

3.1.2 Materials and Methods

To set the optimal parameters of the simulation and achieve dual T_1- and T_2^*-contrast enhanced images with SPION, the MR characteristics of SPION were measured in 1.43 T Bruker Minispec (Bruker, Billerica, MA, USA) and 3 T human scanner (Philips Achieva, Best, the Netherlands). Following these measurements, the simulated signal enhancements in a vessel before and after the circulation of SPION were estimated by using MR imaging parameters of pulse sequences and measured relativities of SPION. Then *in vivo* CE-MRAs with high resolution of Gd-DOTA, Gd-PGC, and SPION were acquired to directly compare vessel-to-tissue contrasts in different contrast agents [63-66]. The Gd-DOTA is used as extravasating T_1-contrast agent and the Gd-PGC is used for conventional intra-vascular T_1-contrast agent. All images from those contrast agents were segmented and those qualities of blood vessel images were quantitatively compared. The BV and vessel diameter of six rats were extracted from longitudinal follow-up studies. The Institutional Animal Care and Use Committee (IACUC) of the Korea Basic Science Institute approved the animal experiments in this study.

Synthetization of SPION

The synthesis of dextran-coated iron oxides used in this work followed the method originally described by Molday and Ohgushi. The synthetization of SPION was described in detail as reported previously [44]. Simply explaining, a solution containing dextran, ferric chloride hexahydrate and ferrous chloride tetrahydrate were mixed to bond each one. And a 30% solution of ammonium hydroxide was included into a synthesized product to change the pH to 12. Then, the synthesized product was cleaned using hollow-fiber filtration cartridges until the free of dextran in colloid was eliminated. From product of iron oxide, monocrystalline iron oxide nanoparticles were remained by using ultrafiltration with hollow membrane cartridges. Synthesized dextran-coated iron oxides are characterized by their core size and hydrodynamic diameters for *in vivo* applications in this work. The hydrodynamic size distribution of synthesized SPION was obtained using a particle size analyzer (Microtrac, UPA-150, Largo, FL, USA) from a dynamic light scattering (DLS) measurement. For core size measurement of SPION, water-dispersible SPION were fell on a carbon-coated copper grid and dried. The transmission electron microscope (TEM, Jeol Ltd, Tokyo, Japan) was used for core size measurement of SPION at 200 kV acceleration voltage. The concentrations of SPION and Gd-PGC were estimated by using inductively coupled plasma optical emission spectrometry (Perkin Elmer, Shelton, CT, USA).

SPION characteristics and in vitro measurements of MR relaxivities

Using the MR instruments, the $R_{1,\,pre}$, $R_{1,\,post}$, $R_{2,\,post}$, $R_{2,\,pre}$, $R_{2,\,post}$, $R^*_{2,\,pre}$ and $R^*_{2,\,post}$ values were obtained at specific concentrations of various contrast agents. And the r_1, r_2, and r_2^* relaxivities were

derived by using measured relaxation rates and the following equations:

$$R_{1,post} = R_{1,pre} + r_1 \times C$$
$$R_{2,post} = R_{2,pre} + r_2 \times C \qquad (3.1.1)$$
$$R^*_{2,post} = R^*_{2,pre} + r^*_2 \times C$$

where $R_{1,\,pre}$, $R_{2,\,pre}$ and $R^*_{2,\,pre}$ are the relaxation rates in the absence of various contrast agents and $R_{1,\,post}$, $R_{2,\,post}$ and $R^*_{2,\,post}$ are the relaxation rates in the presence of various contrast agents. C is the concentration of the contrast agents.

For measurements of *in vitro* relaxivities, a Bruker Minispec MQ20 and a 3T MRI scanner were operated in this study. The pulse sequences of standard turbo inversion recovery (TIR) and CPMG were used by using time domain 1H-NMR measurements of a Bruker Minispec. The concentrations of SPION were adjusted by dilution with phosphate-buffered saline (PBS) and the relaxation rates of R_1 and R_2 were measured at corresponding concentrations of SPION. Different concentrations of Gd-DOTA, Gd-PGC, and SPION were prepared: Gd-DOTA 0.25–3 mM, Gd-PGC 0.16–5.06 mM and SPION 0.11–0.9 mM. Then the relaxivities r_1 and r_2 were fitted by using relaxation rates of R_1 and R_2 at 1.43 T, respectively. The MR relaxivities of Gd- DOTA, Gd-PGC, and SPION were also characterized by using *in vitro* phantom imaging at 3 T. The r_1 relaxivity was determined by using TIR pulse sequence and multi echo spin echo (MESE) sequence was used for r_2 relaxivity. The MR imaging parameters of the TIR pulse sequence were as follows: FA = 90°, TR = 3000 ms, TE = 10 ms, and inversion time (TI) = 50–2600 ms. The MR imaging parameters of the MESE sequence were as follows: FA = 90°, TR = 3900 ms, and TE = 17–70 ms. And multi echo gradient echo (MEGE) sequence was used for r_2^* relaxivity. The MR imaging parameters of the MEGE sequence were as follows: FA = 60°, TR = 3000 ms, and TE = 5–50 ms. The r_1, r_2, and r_2^* relaxivities were estimated from calculated relaxation rates of various contrast agents using a linear model, respectively.

In vivo measurements of MR relaxivities

For the measurements of *in vivo* relaxation rates, R_1 and R_2^* were obtained by using Look–Locker and MEGE sequences [67]. The MR imaging parameters of the Look–Locker sequence for obtaining T_1-map were as follows: FA = 7°, TR = 18 ms, TI = 52–852 ms, FOV = 50 × 50 × 20 mm^3, matrix = 256 × 256 × 10, slice thickness = 2 mm, ETL = 10, and NA = 1. The MR imaging parameters of the MEGE sequence were as follows: FA = 60°, TR = 3000 ms, TE = 7–37 ms, FOV = 50 × 50 × 20 mm^3, matrix = 256 × 256 × 20, slice thickness = 1 mm, ETL = 6, and NA = 2. To estimate *in vivo* r_1 and r_2^* values using **Equation 3.1.1**, the signal intensities were evaluated in the jugular vein near the rat's head and then multiple relaxation rates were calculated from signal intensities. The slopes of several relaxation

rates were fitted at various SPION concentrations (0 mM, 0.35 mM, 0.7 mM, 1.04 mM, and 1.38 mM).

Signal enhancement simulations

Based on measured relaxivities of *in vivo* r_1 and r_2^*, the simulated signal enhancements by SPION in a vessel were estimated by adjusting the TR, TE, and FA of MR imaging parameters and SPION concentrations. The signal intensities by the presence or absence of the SPION injections were calculated by using the following equation:

$$S = S_0 \frac{[1-e^{-TR\cdot R_1}]}{[1-\cos(\alpha)\cdot e^{-TR\cdot R_1}]} \cdot \sin(\alpha) \cdot e^{-TE\cdot R_2^*} \qquad (3.1.2)$$

where S_0 indicates the equilibrium magnetization and S indicates the signal intensity. α is flip angle. Finally, signal enhancement is calculated from signal intensities presence and absence of SPION using the following equation:

$$Enhancement = \frac{S_{post}-S_{pre}}{S_{pre}} \qquad (3.1.3)$$

where S_{pre} and S_{post} are signal intensities of the presence and absence of SPION. The calculated signal enhancement with adjustable MR imaging parameters at specific concentrations of SPION was represented using RGB color values to verify the positively and negatively enhanced contrast of vessel region in *in vivo* experiment.

In vivo CE-MRA

All MRAs of Sprague-Dawley (SD) rats (Orient Bio, Seongnam, South Korea) were acquired by using a volume coil on a 3 T MRI. The MRAs with Gd-DOTA were obtained from two rats. To directly compare MRAs with SPION and standard intra-vascular agent, the follow-up experiments with SPION (0 hours) and Gd-PGC (48 hours) were performed using six rats (185 g–195 g). All MR images before injection of various contrast agents were acquired firstly. The injection doses of Gd-DOTA and Gd-PGC were 100 μmol/kg and 43 μmol/kg for each rat, respectively. The first injection dose of SPION (5 mg/mL) which was circulated in SD rat's body through the peripheral vein was 44.8 μmol/kg and then MR images were obtained by using FLASH and UTE pulse sequences [68, 69]. After the first injection and acquisitions of the FLASH and UTE MRA, the SPION at a dose of 179.1 μmol/kg was injected secondly and MR images were obtained by using FLASH and UTE pulse sequences immediately. The *in vivo* concentration of SPION was evaluated by using body weight (BW)-based blood volume (BV, BV = 0.06 × BW + 0.77) [70]. The SPION concentration in the rat's blood vessels was to be ~0.71 mM

for the first injection and ~ 2.7 mM for the second injection of SPION. The MR imaging parameters of the FLASH sequence were as follows: FA = 25° and 40°, TR = 25 ms, TE = 3.6 ms, FOV = 120 × 120 × 46 mm^3, matrix = 480 × 480 × 46, and NA = 1. The MR imaging parameters of the UTE sequence were as follows: FA = 40°, TR = 25 ms, TE = 0.09 ms, FOV = 120 × 120 × 46 mm^3, matrix = 480 × 480 × 46, and NA = 1.

Imaging processing and statistical analysis of positive MRA

To extract vascular parameters, all MR images were applied by resize and registration algorithm. For converting an isotropic and high resolution, all MR images were resized by using cubic interpolation technique in ImageJ 1.46r [71]. And then affine and rigid image registration was performed to the resized images for the initial alignment. The final images were obtained by using a deformable transformation with mutual information in the Insight Toolkit, Ver. 2.4 to reduce motion artifacts [72]. The resultant processed vasculature images were acquired by using an Otsu threshold algorithm for extracting the initial segmented vessels [73]. Surface and volume rendering of processed vasculature images were obtained by using an in-house software based on VC++ and OpenGL.

The head region of rat in the segmentation image remains and the rest parts were cropped. The absolute BVs of the FLASH and UTE MRAs were calculated from the segmented vessels of rat head. And dividing the acquired absolute and the total BV of the FLASH and UTE MRAs was defined as the relative BV of the FLASH and UTE MRAs. The diameters of the vessels were estimated by using a blob-fitting method in free-software of ImageJ 1.46r [74, 75]. For blob fitting method, initial 3D blobs were located at center line of the segmented vessels. Then, the 3D blob was swollen until it reached the exterior vessel surface. Based on the diameter of the increased 3D blob, the vessel diameters were determined.

To validate the accuracy of segmentation and estimated diameters of vessel from the MRAs, the estimated vessel diameters of segmented rat carotid artery and jugular vein from UTE MRA were measured for comparing with those diameters from visual assessments after surgery [76, 77]. For extraction of the discernible vessel diameters with various contrast agents, histogram analysis was performed for comparison of vessel diameter distributions from segmentation of FLASH and UTE MRAs with Gd-PGC and SPION. To verify the normal distribution for statistical analysis, Shapiro-Wilk test was applied to vessel diameter distributions of MRAs groups with Gd-PGC and SPION. Then, *T*-test was used for verifying statistical differences of various vessel diameters from all combinational six ($_4C_2$) paired MRAs groups for each bin 500 μm of the vessel diameter histogram. Detailed descriptions of the study design and quantification process for extraction of vascular parameters are explained below and shown in **Figure 3.1.1**.

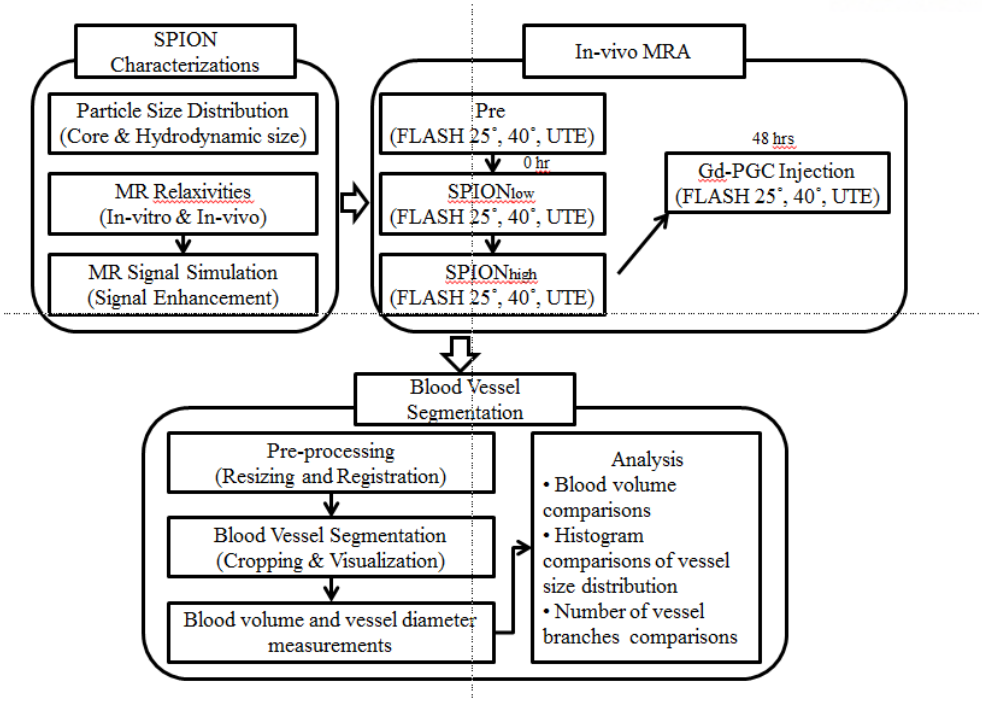

Figure 3.1.1 Study design and process flow chart

Dual-contrast MRA

For investigation of the complementary dual contrast benefits, the identical image slices of the head region along the coronal direction including multiple vessel branches, air-ways, and bones from FLASH and UTE MRAs with $SPION_{high}$ were compared. The number of detected vessel branches in the rat's head regions from FLASH and UTE MRAs was evaluated for verification of the direct advantage of single SPION injection. This comparison was performed without image registration because the FLASH and UTE MRAs were obtained sequentially. And erroneously regions of FLASH MRA with negatively enhanced contrast caused by susceptibility artifacts were compared and classified by same regions of UTE MRA with positively enhanced contrast.

3.1.3 Results

SPION characterization

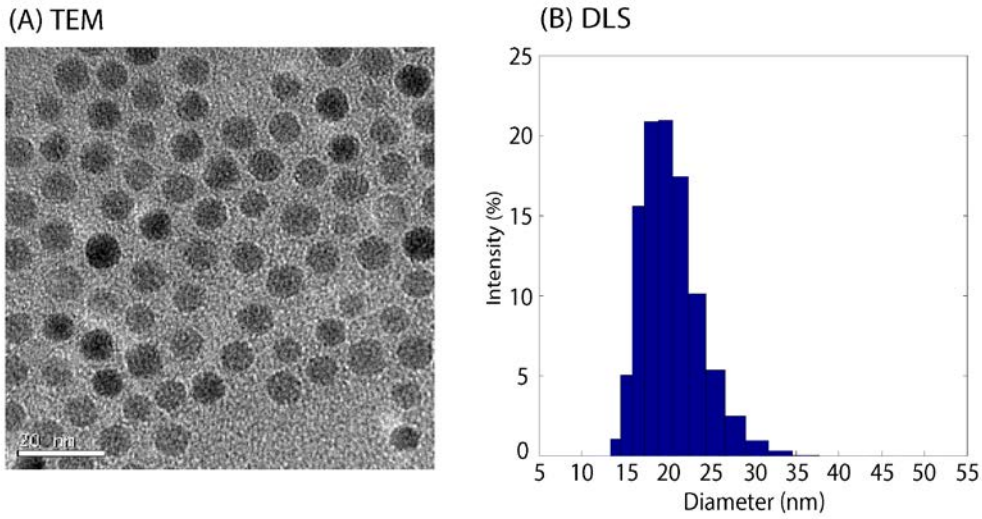

Figure 3.1.2 The characterizations of SPION: (A) the TEM image of SPION and (B) the distribution of SPION hydrodynamic diameters. The mean core and hydrodynamic sizes were approximately 7 and 20 nm, respectively.

The core size distribution of the SPION using the TEM was 5–10 nm as shown in **Figure 3.1.2A**. The average of hydrodynamic diameters of the SPION was 20 ± 7 nm by using DLS experiment as shown in **Figure 3.1.2B**. The nanoparticles were evenly spread with no doubt of clustering synthesized SPION as shown in TEM measurements. **Table 3.1.1** summarizes the *in vitro* r_1, r_2, and r_2^* values of Gd-PGC, Gd-DOTA, and SPION at 1.43 T and 3 T, respectively. The r_2 values of SPION at 1.43 T and 3 T were pretty much of the same at similar echo times, whereas the r_1 values of SPION decreased as magnetic field strength was increased. The *in vitro* r_2/r_1 ratios of SPION at 1.43 T and at 3 T were relatively larger than those of Gd-PGC and Gd-DOTA.

	Field	r_1 (mM^{-1} s^{-1})	r_2 (mM^{-1} s^{-1})	r_2^* (mM^{-1} s^{-1})	r_2/r_1
Gd-PGC	**3T**	7.21	9.14 (TE = 5.85ms)	11.25	1.3
Gd-DOTA	**3T**	3.77	5.25 (TE = 5.85ms)		1.4
SPION	**1.43T**	13.31	40.90 (TE = 5 ms)		3.1
	3T	6.84	39.68 (TE = 5.85ms)	49.50	5.8

Table 3.1.1. The relaxivities of Gd-PGC, Gd-DOTA, and SPION in the *in vitro* measurements.

To measure the *in vivo* relaxivities of SPION, $R_{1,\,pre}$, $R_{1,\,post}$, $R_{2,\,post}$, $R^*_{2,\,pre}$, and $R^*_{2,\,post}$ were estimated for a region of the rat's jugular vessel as indicated by white colored ROI in **Figure 3.1.3A-1** and **Figure 3.1.3B-1**. The fitted R_2^* relaxation rate before and after SPION injection (0.35 mM) were shown in **Figure 3.1.3A-2** and **A-3**. **Figure 3.1.3B-2** and **B-3** show the fitted R_1 relaxation rate from before and after SPION injection (0.35 mM). As shown in **Figure 3.1.3A-4**, these fittings were performed at five different concentrations of SPION in a vessel and *in vivo* r_2^* was obtained from the line slope between *in vivo* relaxation rates versus concentrations from **Equation 3.1.1**. The estimated *in vivo* r_2^* of SPION in blood vessels was 123.51 $mM^{-1}s^{-1}$ and was significantly elevated by comparing the corresponding *in vitro* value. Similarly, the corresponding *in vivo* r_1 was calculated to be 5.32 $mM^{-1}s^{-1}$ as shown in **Figure 3.1.3B-4**, which was close to the value of *in vitro* r_1.

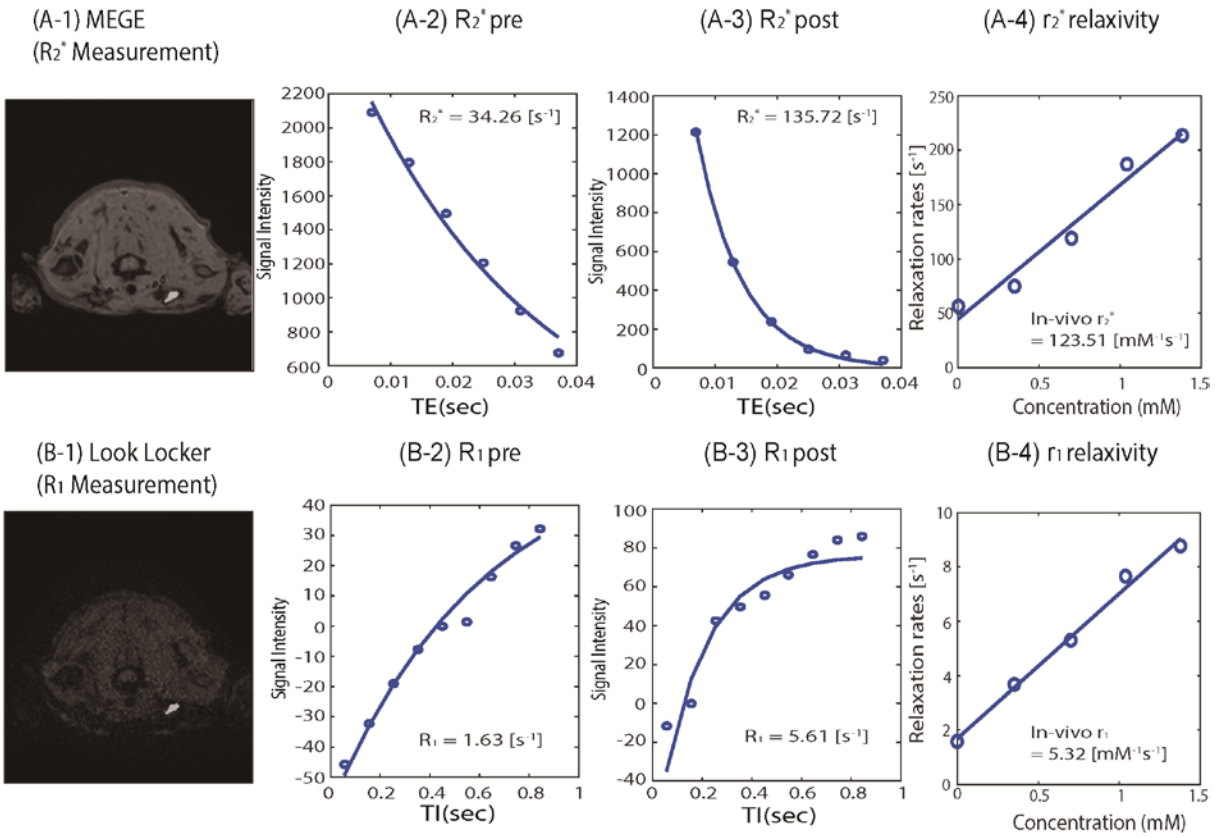

Figure 3.1.3 The measurements of *in vivo* relaxivities. (A-1) and (B-1) show representative T_2^*- and T_1-weighted MR images with axial direction. In panels (A-2, 3) and (B-2, 3), The fitting graphs of signal intensities before and after SPION injection were shown, respectively. The circle marks indicated the mean of signal intensity in jugular vein which was used as a ROI. In panels (A-4) and (B-4), estimated *in vivo* r_2^* and r_1 relaxivities are shown, respectively. For the relaxivities measurements, the different concentration of SPION was 0 mM, 0.35 mM, 0.7 mM, 1.04 mM, and 1.38 mM.

Signal enhancement simulations

The **Equation 3.1.2** and **3.1.3** were used for signal enhancement simulations. The signal enhancements before and after the SPION injections were calculated at multiple MR parameters. The values of *in vivo* r_1 and r_2^* from the signal of the jugular vessels were fed into the simulations. As shown in **Figure 3.1.4**, the three MR imaging parameters were adjusted to calculate signal enhancements as a function of SPION concentrations. Each signal enhancement was calculated as a function of TR at fixed TE 3.6 ms and FA 25°, TE at fixed TR 25 ms and FA 25°, and FA at fixed TE 3.6 ms and TR 25 ms, respectively. The nullified the signal enhancement was indicated by the solid black line. Four conditions with three imaging parameters of FLASH and UTE pulse sequences were investigated in the experiment and those are indicated by red and blue dots on the three plots.

The red and blue dots on each figure apparently represent that SPION can be used as a positively and negatively enhanced contrast agent. Generally, positive signal enhancement was large as the SPION concentration increased at a large FA, short TE, and short TR. As concentration of SPION with low FA, long TE, and long TR, the signal enhancement was decreased. From solid black lines on the three plots, the shift from positively to negatively enhanced contrast was obviously appeared. Especially, positive signal enhancement was generally provided within the extremely short TE range of UTE sequences.

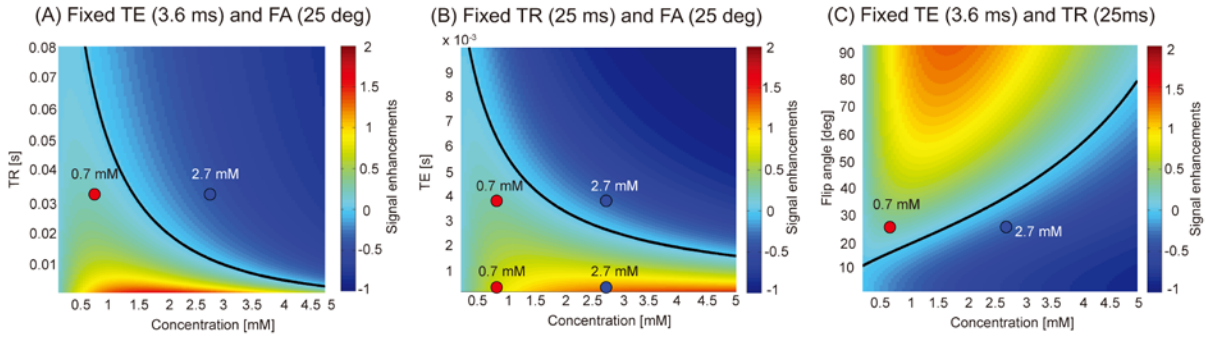

Figure 3.1.4 Simulations of calculated signal enhancement: signal enhancement using the steady-state signal equation is shown as a function of (A) TR at fixed FA and TE, (B) TE at fixed FA and TR, and (C) FA at fixed TE and TR. The red and blue dots on the plots are indicated as positively and negatively enhanced contrast experimentally. The solid black lines indicated nullified signal enhancement at the specific parameters.

In vivo MRA with Gd-DOTA, FLASH and UTE

In vivo MRAs in absence and presence of SPION and standard T_1-contrast agents were obtained by using FLASH and UTE pulse sequences. In **Figure 3.1.5**, the representative maximum intensity projection (MIP) images from FLASH and UTE MRA are shown in rats which were circulated with various contrast agents. The rat 1 was injected with Gd-DOTA and the MIP images in first and second rows of

Figure 3.1.5A-1 and **B-1** were obtained from FLASH and UTE MRA. The rat 2 was circulated by SPION (0 hours) and Gd-PGC (48 hours after the injection of SPION) for a follow-up study and the MIP images of first and second rows in **Figure 3.1.5A-2**, **A-3**, **A-4** and **B-2**, **B-3**, **B-4** also obtained from FLASH and UTE MRA after circulation of Gd-PGC, SPIONlow, and SPIONhigh, respectively. The doses of the injected various contrast agents were 100 μmol/kg for Gd-DOTA, 43 μmol/kg for Gd-PGC, 44.8 μmol/kg for $SPION_{low}$, and 179.1 μmol/kg for $SPION_{high}$. The injection doses of SPION were related to the nominal *in vivo* concentrations which were expected by using BW-based blood volume.

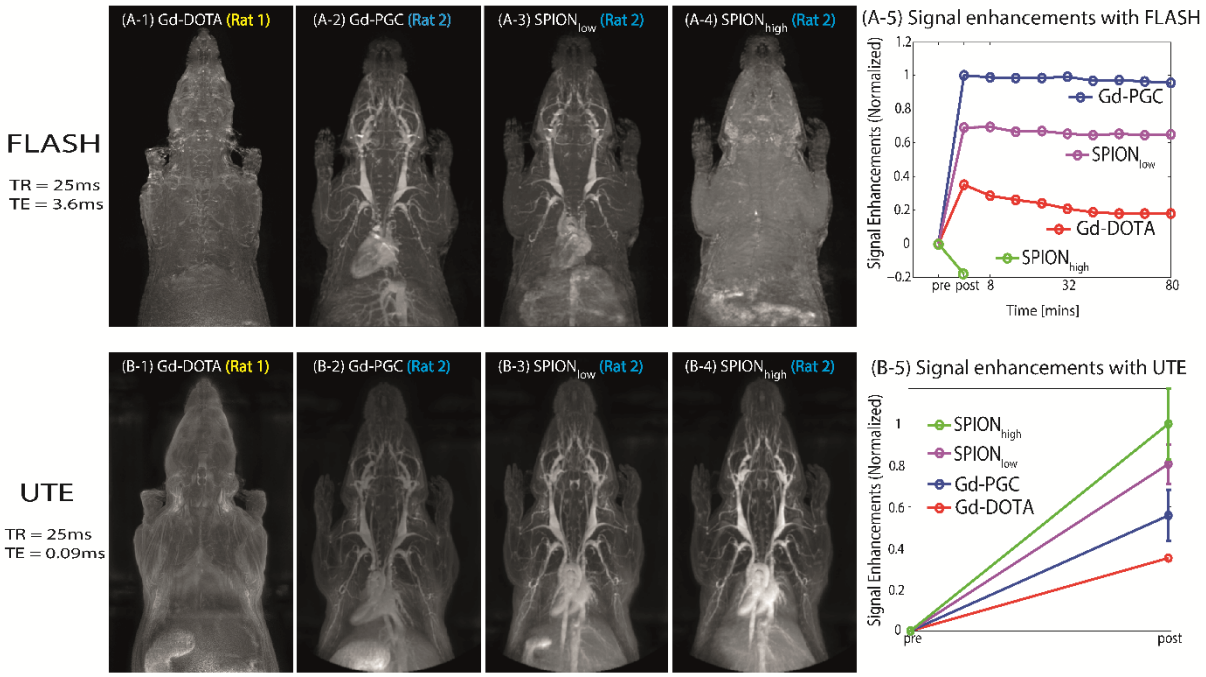

Figure 3.1.5 *In vivo* CE-MRA with various contrast agents. Panels (A-1), (A-2), (A-3), and (A-4) show MIP images by using FLASH sequence after injection of Gd-DOTA, Gd-PGC, $SPION_{low}$, and $SPION_{high}$, respectively. Panels (B-1), (B-2), (B-3), and (B-4) show MIP images by using UTE sequence after injection of Gd-DOTA, Gd-PGC, $SPION_{low}$, and $SPION_{high}$, respectively. Panels (A-5) and (B-5) show the signal enhancement versus time in the carotid artery of FLASH and UTE MRAs, respectively.

The MIP images of FLASH and UTE MRA with Gd-DOTA show no signal enhancements in vessel regions because of short circulation time of Gd-DOTA as shown in **Figure 3.1.5A-1** and **B-1**. So it is a limitation of the high resolution MRA with Gd-DOTA by using both FLASH and UTE pulse sequences. The MIP images of FLASH MRA with Gd-PGC and $SPION_{low}$ in the first column of **Figures 3.1.5** show positively enhanced vessels, respectively. The MIP image of FLASH MRA with $SPION_{high}$ do not show signal enhancement because of negatively enhanced vessels in a rat. The most of MIP images of

UTE MRA in the second row visualize vessels with positively enhanced contrast except for UTE MRA with Gd-DOTA. As shown in **Figure 3.1.4**, The red (positively enhanced enhancement) and blue (negatively enhanced enhancement) dots of simulation results were consistent with the experiment results of dose-dependent positively and negatively enhanced contrast behaviors of SPION at the provided MR imaging parameters.

In **Figure 3.1.5A-2** and **A-3**, the MIP images of FLASH MRA with Gd-PGC in the head region of the Rat-2 show the more delineate vessel structure than that with $SPION_{low}$. In **Figure 3.1.5A-4**, the MIP image of FLASH MRA with $SPION_{high}$ shows no positively enhanced vessels in head and body regions. On the other hand, MIP images of UTE MRA with Gd-PGC, $SPION_{low}$, and $SPION_{high}$ show no noticeable changes in visualization of depicting well-defined vasculatures, as seen in **Figure 3.1.5B-2**, **B-3**, and **B-4**. In addition, the aorta was not obviously noticeable in MIP images of FLASH MRA with Gd-PGC and SPION but MIP images of UTE MRA with Gd-PGC and SPION show a well-defined vasculature image of the aorta.

In **Figure 3.1.5A-5** and **B-5**, the signal enhancement changes of FLASH and UTE MRAs in the carotid artery were plotted, respectively. And plotted signal enhancements were averaged over six longitudinal studies. The signal enhancements by using the Gd-PGC and SPION were preserved for over 80 minutes as shown in **Figure 3.1.5A-5**. It seemed that SPION is suitable as blood pool contrast agents in the MRA with high resolution. The signal enhancement of FLASH MRA with Gd-DOTA was decreased by comparing to those with other contrast agents. This result is supported that Gd-DOTA is insufficient for use of blood pool contrast. The signal enhancement of FLASH MRA with Gd-PGC was greater than that with any other contrast agent. On the contrary, the signal enhancements of UTE-MRA with both $SPION_{low}$ and $SPION_{high}$ were significantly greater than that with Gd-PGC.

Blood vessel segmentation, blood volume, and vessel diameter of positively enhanced MRAs

To validate the accuracy of the vascular parameters of segmented MRAs with SPION, the volume renderings of segmented vessels were performed as shown in **Figure 3.1.6**. Then BV measurements of segmented MRA were performed for each contrast agent. **Table 3.1.2** summarizes the absolute and

Contrast agent	**Gd-PGC (n = 6)**		**$SPION_{low}$** (44.8 μmol/kg, n = 6)	
Units	Absolute BV (cc)	Relative BV (%)	Absolute BV (cc)	Relative BV (%)
FLASH (25°)	1.49 ± 0.07	11.65 ± 0.07	1.04 ± 0.13 (*)	8.00 ± 0.78 (*)
FLASH (40°)	1.44 ± 0.06	11.26 ± 0.06	0.94 ± 0.16 (*)	7.25 ± 0.94 (*)
UTE (40°)	1.49 ± 0.06	11.62 ± 0.06	1.68 ± 0.09 (**)	13.03 ± 0.69 (**)
UTE (40°)	N/A		$SPION_{high}$ (179.1 μmol/kg, n = 6)	
			1.76 ± 0.22 (**)	13.59 ± 1.38 (**)

Table 3.1.2 BV measurements of segmented vessels from six longitudinal follow-up studies.

relative BV with Gd-PGC and SPION. For FLASH MRA with $SPION_{high}$, the segmented vessel could not be obtained due to negatively enhanced blood vessel contrast. (*) and (**) indicate significantly difference of blood volume which was compared with corresponding Gd-PGC measurements, respectively from *T*-test. The relative and absolute BVs from UTE MRA with $SPION_{low}$ and $SPION_{high}$ were meaningfully larger than that with Gd-PGC because of the increased vessel signal enhancement by SPION. The vessel segmentation of MRA with SPION for six rats was apt to include more voxels near the boundary between vessel and tissue with as demonstrated in **Figure 3.1.5B-5**. The FLASH MRA with $SPION_{low}$ provides less BV when compared with that with Gd-PGC because of decreased vessel signals due to the strong T_2^* effect by SPION at long TE. This result was reasonable by visually and quantitative observation of slightly dim vessels as shown in **Figure 3.1.5A-5**.

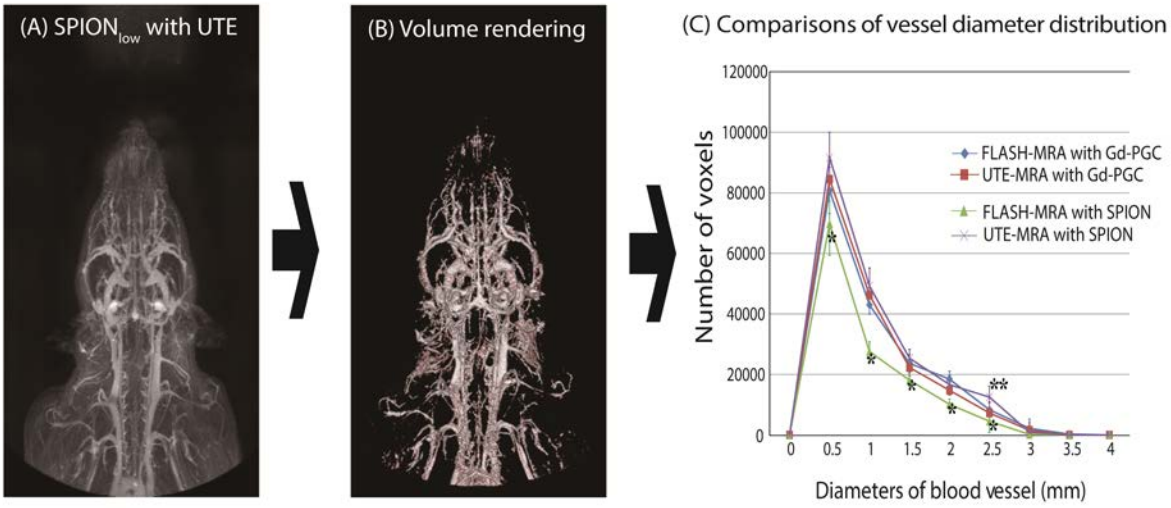

Figure 3.1.6 Visualization of segmented blood vessel: panel (A) shows an MIP image of UTE-MRA with $SPION_{low}$, which was the head region. And panel (B) shows the volume renderings of UTE-MRA with $SPION_{low}$. Histogram of vessel diameter distributions is shown in panel (C) for four combinations: UTE MRA with Gd-PGC, FLASH MRA with Gd-PGC, UTE MRA with SPION, and FLASH MRA with SPION. (*) and (**) refer to $p < 0.05$ determined by T-test.

In **Figure 3.1.6**, the blood vessel diameters of six rats in longitudinal studies were measured by using a blob-fitting method. Measured vessel diameters of carotid artery and jugular vein in the UTE MRA with SPION were 0.94 ± 0.21 mm and 2.09 ± 0.10 mm, respectively. Previously investigated vessel diameters from visually measurements of vessel after surgery were 1.17 ± 0.09 mm for carotid artery and 1.9 ± 0.2 mm for the jugular vein. It appears to be appropriate for the segmentation and quantification methods of MRAs with SPION in this work. As shown in **Figure 3.1.6C**, the vessel diameter distributions of six rats were acquired from FLASH and UTE MRAs with Gd-PGC and $SPION_{low}$. The

colored line of FLASH MRA with Gd-PGC (blue), UTE MRA with Gd-PGC (red), FLASH MRA with $SPION_{low}$ (green) and UTE MRA with $SPION_{low}$ (purple) represented the average voxel numbers of segmented vessel for each bin ranging between 0.5 mm and 2 mm, respectively. To confirm a normal distribution of each bin for all six combinations, Shapiro-Wilk test performed except for 2 mm-bin between UTE MRA with Gd-PGC and $SPION_{low}$ because of low count. There is no statistically significant (*T*-test, $p < 0.05$) difference except FLASH MRA with $SPION_{low}$. The vessel diameter counts in FLASH MRA with $SPION_{low}$ was marked with single asterisk in **Figure 3.1.6C** and statistically lower ($p < 0.05$) than the other measurements. UTE MRA with $SPION_{low}$ also presented larger vessel counts ($p < 0.05$) at 2.5 mm-bin and marked with double asterisk in **Figure 3.1.6C**. Although slightly larger voxel counts in small vessel (< 1 mm) was observed, UTE MRA with $SPION_{low}$ provides a consistent vessel size count compared to UTE MRA with standard intravascular T_1 contrast agent. This results show enhanced vessel-to-tissue contrast and slightly improved BV measurements.

Dual-contrast-enhanced images from SPION

To verify direct benefit of dual contrast, the head region, bones, and air-ways of FLASH and UTE MRA with $SPION_{high}$ were compared. As shown in **Figure 3.1.7**, the noticeable fine vessels in the head of the rat were detected in the FLASH MRA with negatively enhanced contrast, but UTE MRA with positively enhanced contrast was not visible fine vessels. Magnified head region of FLASH and UTE MRAs were shown in **Figure 3.1.7A-2** and **B-2** and the red lines for each MRA covered delicate vessels. The observable numbers of vessel branches were 3 and 3.5 with negatively enhanced contrast from FLASH MRA and were 1 and 2 with positively enhanced contrast from UTE MRA. This result showed the increased sensitivity of negatively enhanced contrast MRA in detecting well-defined vessels in the head region. However, the white arrows indicate erroneously darkening signal in the FLASH MRA, which can be distinguished by positively enhanced contrast from UTE MRA in the non-vessel region. As indicated by the white arrow in **Figure 3.1.7A-1** and **B-1**, the negatively enhanced contrasts were also erroneously provided in the airways and bones. Positively contrast enhanced UTE-MRAs with SPION were shown in **Figure 3.1.7A-3** and **B-3**. It can be considered as obvious vessel regions from UTE MRA with SPION. It can be applied to remove false-positively enhanced regions such as airways and bones from FLASH MRA alone.

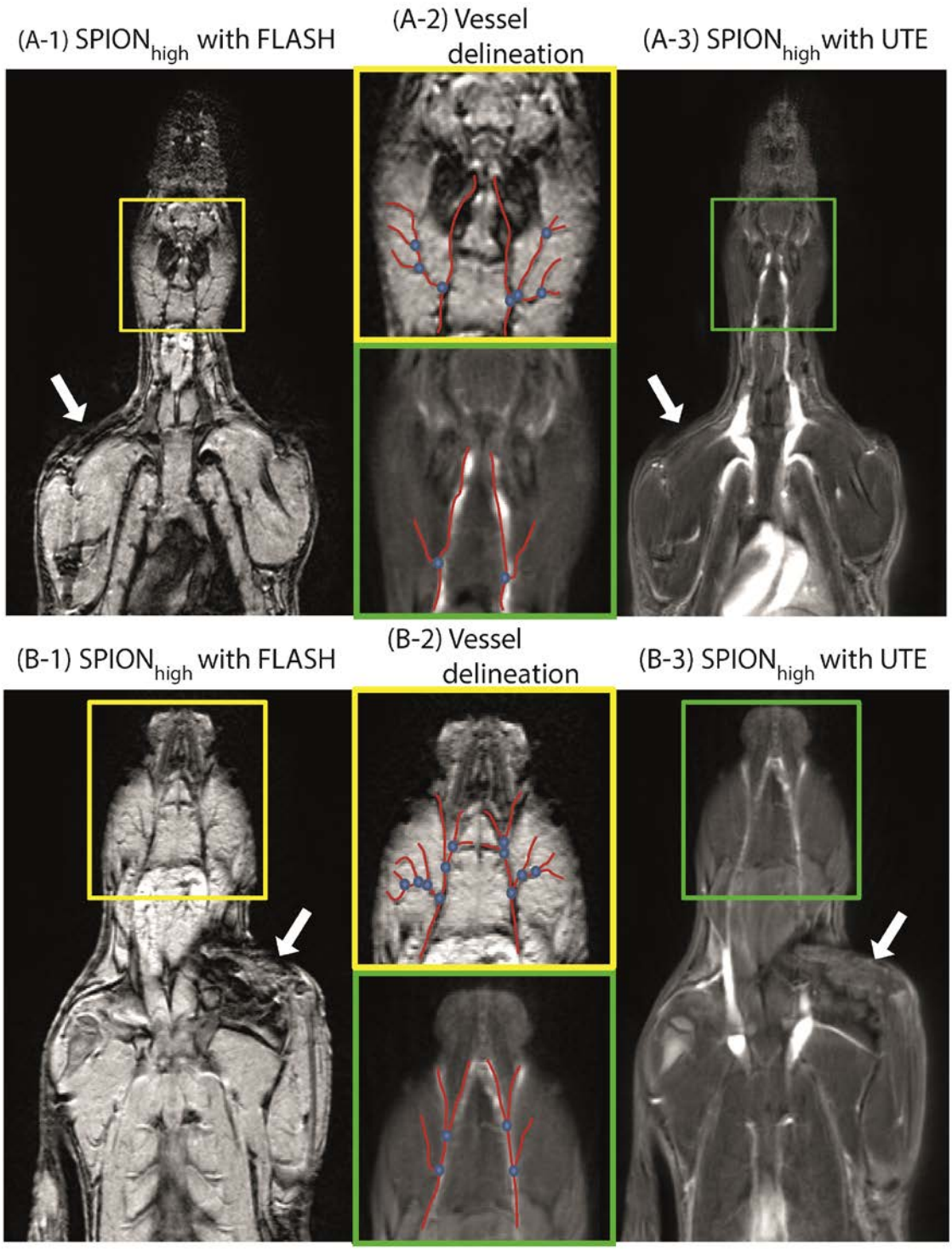

Figure 3.1.7 Dual positively and negatively enhanced contrast MRAs with SPION: panels (A-1) and (B-1) show negatively enhanced vessel-to-tissue contrasts of FLASH MRA after SPION$_{high}$ injection. Panels (A-3) and (B-3) show positively enhanced vessel-to-tissue contrasts of UTE MRA after SPIO-N$_{high}$ injection for corresponding rats. Panels (A-2) and (B-2) show well-defined vessels in the head region depicted by negatively and positively enhanced contrast.

3.1.4 Discussion and conclusions

We demonstrated that dual-mode MRA using a size-controlled SPION was possible at a particular dose of $SPION_{high}$; 179.1 μmol/kg by using 3 T MRI. The negatively and positively enhanced contrasts were provided with FLASH (TE = 3.6 ms) and UTE (TE = 0.09 ms). We predicted these experimental observations from the calculation by using steady-state signal intensity equation and the estimated *in vitro* and *in vivo* MR relaxivities of SPION. As the SPION concentration raised in the jugular vessel, the measured *in vivo* MR relaxation rate also increased. And the *in vivo* r_1 and r_2^* relaxivities were estimated from those fitted slope for signal enhancement simulations. The *in vivo* r_1 (5.32 $mM^{-1}s^{-1}$) of SPION was slightly lower than the *in vitro* r_1 (6.84 $mM^{-1}s^{-1}$), probably due to the underestimated *in vivo* intra-vascular concentration of SPION. The *in vivo* r_2^* (123.51 $mM^{-1}s^{-1}$) of SPION in the vessel was greater than the *in vitro* r_2^* (49.50 $mM^{-1}s^{-1}$) at 3 T because of the difference between the *in vivo* and *in vitro* environments. The *in vivo* r_2^* is intensely influenced by the magnetic susceptibility interference caused by the SPION and the background tissue. The reduced ratio of *in vivo* r_1/r_2^* of SPION will weaken the positively enhanced contrast at a fixed TE. Nonetheless, simulations and experiments at low and high doses of SPION by using both FLASH and UTE pulse sequences demonstrated that adjusting MR imaging parameters could be set to acquire positively enhanced contrast, particularly when an extremely short TE was applied.

CE-MRAs before and after the circulation of SPION and standard T_1-contrast agents were obtained by using FLASH and UTE pulse sequences. The vessel-to-tissue contrast of CE-MRA with Gd-DOTA was no change due to the rapid washout of the contrast agent in vessels of rodent. As for the signal intensity of the carotid artery with Gd-PGC and SPION, it showed that the conventional intra-vascular T_1 agent Gd-PGC gives the highest vessel-to-tissue contrast by using FLASH pulse sequence because of strong T_2^* decay of SPION. In case of FLASH and UTE MRAs with $SPION_{low}$ and UTE MRA with $SPION_{high}$, the positively enhanced contrast was shown in vessels of rodent. Whereas FLASH MRA with $SPION_{high}$ showed negatively enhanced contrast of vessels. The resultant vessel-to-tissue contrast of UTE MRAs with $SPION_{low}$ and $SPION_{high}$ were significantly higher than conventional intra-vascular T_1 agent Gd-PGC. Regarding the result that the r_1 relaxivities of Gd-PGC and SPION were similar at 3 T, the actual *in vivo* concentration of SPION is likely to be higher than that of Gd-PGC due to different *in vivo* clearance or distribution. It is also noteworthy that the enhanced contrast of the aorta region, including the aortic arch with both Gd-PGC and SPION was positively enhanced contrast in UTE-MRA but not in FLASH MRA. It is likely to elevate r_2^* in the aorta due to high concentration of the Gd-PGC and SPION, resulting in signal reduction for both contrast agents when the FLASH pulse sequence was used.

For quantitative analysis of the BV and vessel diameter, segmented vessels in FLASH and UTE MRAs

after injection of Gd-PGC and SPION were obtained. The agreement of estimated and previously reported vessel diameters of both carotid artery and jugular vein confirms the precision of the MRA with size controlled SPION and the process of segmented vessels implemented in this work. However, it should be noted that segmentation results along the slice direction with the anisotropic acquisition (0.25 × 0.25 × 1 mm^3) have influenced by partial volume averaging effect. This image voxel which was applied by interpolation and thresholding process may limit measurements of precise quantification of BV and vessel diameter. Future optimizations of MRA acquisitions with SPION and segmentations are necessitated for more robust quantification of various vascular parameters.

The blood volume of the UTE MRA with $SPION_{high}$ (1.76 ± 0.22 cc) was slightly larger than that with Gd-PGC (1.49 ± 0.06 cc) because of the increased vessel-to-tissue contrast. As shown in **Figure 3.1.5B-5**, many pixels in UTE MRA at the boundary between vessel and tissue are obviously visible and were consequently involved in segmented vessel. On the other hand, the BV of FLASH MRA with $SPION_{low}$ (0.94 ± 0.16 cc) was significantly lower than that with Gd-PGC. This result reflects the signal intensity reduction affected by the T_2^* effect of FLASH MRA with SPION because of the r_2^* relaxivity of SPION is higher than that of Gd-PGC. As shown in **Figure 3.1.6C**, the number of pixels for segmented vessels in the head region of FLASH MRA with SPION was consequently decreased because of reduced vessel-to-tissue contrast by T_2^*-effect. The BV measurements of FLASH MRA with $SPION_{low}$ were also reduced as shown in **Table 3.1.2**. The vessel diameter distribution of UTE MRA with SPION was similar compared with that estimated diameter of UTE MRA with Gd-PGC injection as shown in **Figure 3.1.6C**. And the BV measurements of UTE MRA with Gd-PGC and $SPION_{low}$ were also similar. Based on measurement of UTE MRA with Gd-PGC, the accuracy of positively enhanced MRA with SPION and improved sensitivity by SPION were demonstrated by showing the overall consistency in diameter distribution and the slight rise of the count in UTE-MRA with $SPION_{low}$, respectively.

The negatively enhanced contrast MRA by using FLASH sequence with the $SPION_{high}$ provided delineated vasculature in the head region as shown in Figure **3.1.7A-2** and **B-2**. Increased detected well-defined vessels from negatively enhanced contrast MRA can be comprehended because the induced magnetic field variations by susceptibility artifact caused by SPION spread out to external-vascular regions by influencing the phase accumulation loss of nearby protons around the vessels. So, the improved sensitivity for thin and small vessels was obtained from negatively enhanced contrast MRA by using FLASH pulse sequence, and the positively enhanced contrast MRA by using UTE pulse sequence decreased the deceptive contrast resulting from erroneously decreased signal intensity in T_2^*-weighted images by using FLASH pulse sequence. The co-registration of two dual contrast MRAs with SPION provided complementary information and also presents the opportunity of co-registering positively enhanced contrast conventional MRA and MRI methods with negatively enhanced contrast for measuring vessel size and relative cerebral blood volume (rCBV). The vessel diameter and calculated rCBV using

MRA with SPION would also be much more precise than those acquired from MRA with Gd-DOTA. The leakage of Gd-DOTA could misevaluate vessel size and rCBV measurements. Also, the increased potential application of SPION as a positive signal-enhancing contrast agent may include T_1-based MRA measurements of vascular parameters such as water exchange rate and absolute cerebral blood volume (aCBV).

Our study is a preclinical imaging method because the SPION that we used has not yet clinically permitted. The recent development of FDA-approved Feraheme (AMAG Pharmaceuticals, Lexington, MA, USA) as a sort of iron oxide nanoparticles has been clinically enabled for the therapy of iron-deficiency anemia and being employed in MRI [78-80]. Furthermore, SPION or FDA-approved iron oxide nanoparticle may enable the clinical applications by using the described method of dual contrast with a SPION.

In summary, our simulations and *in vitro* and *in vivo* experiments demonstrated the dual contrast acquisition with size controlled iron oxide by using presented FLASH and UTE pulse sequences. By taking advantage of both measurements of positively and negatively enhanced contrast for the many-sided characterization of vasculature using a SPION, the potential usages of the suggested dual contrast may develop for observing of vascular response and progression in longitudinal studies of various oncological and neurodegenerative diseases or therapies.

3.2 UTE–ΔR_2–ΔR_2^* combined MR whole-brain angiogram using dual-contrast superparamagnetic iron oxide nanoparticles

3.2.1 Introduction

In previous study, dual contrast MRAs with SPION show a potentiality of imaging cerebral micro-vessels by both longitudinal (R_1) and transverse (ΔR_2^*) relaxation-based MRAs. Especially, spin (ΔR_2) and gradient (ΔR_2^*) echo-based MRAs are being developed for the visualizing of the cerebral micro-vasculature in rodent by using the conjunction with exogenous blood pool contrast agents [40, 41, 81-89]. On the experimental observation, the cerebral vasculatures such as intra-cortical penetrating arterioles and venules were detected in ΔR_2 and ΔR_2^* MRAs, but those were not visible in conventional T_1-contrast weighted MRA [52, 90-93].

The ΔR_2 and ΔR_2^* MRAs provide higher sensitivity of micro-vessels when those MRAs compared with general T_1-contrast weighted MRA as a Gd-based contrast agent. This result shows that intra-vascular SPION affects intra- and extra-vascular signal decay to increase transverse relaxation rate by diffusible protons in the susceptibility-induced magnetic field (especially at higher field strengths, > 7 T). Particularly, the sensitivity of fine vessels in ΔR_2^* MRA with restricted spatial resolution is higher than that in ΔR_2 MRA due to strong loss of phase coherence. So, the ΔR_2 MRA is generally preferred because the rodent brain vessels of ΔR_2^* MRA were suffered by strong signal dephasing. This erroneously signal reduction was well-known as the vessel size overestimation and air-tissue interface artifact.

T_1-weighted MRA presents precise information of vasculature without signal contribution from extra-vascular regions, and is unaffected from undesirable signal dephasings which was called by air–tissue interface artifacts [94, 95]. Specially, the T_1-weighted MRA by using UTE pulse sequence minimizes the T_2- and T_2^*-relaxation decay by SPION and improves positively enhanced vessel-to-tissue contrast [36, 96].

Consequently, systematical comparisons of UTE (R_1), ΔR_2, and ΔR_2^* MRAs on the same target were required. The synergistic combinations of different MRAs was tried if it is possible [97-99]. Furthermore, this systematic evaluation and complementary merger of different MRAs will be considered for applications of brain disease model [69, 100, 101].

In this study, the finite perturber method (FPM) simulation of the extra-vascular signal variation was performed for investigating behavior of ΔR_2 and ΔR_2^* values for various cylinder-shaped vessel models with changing vessel diameters to quantitatively evaluate issues of both their sensitivity and vessel diameter overestimation in different MRAs. The advantages from the synergistic combinations of ΔR_2 and ΔR_2^* values were also observed. Next, UTE, ΔR_2, and ΔR_2^* MRAs were serially obtained by using

UTE, FLASH, and TSE pulse sequences with SPION. We directly compared the strengths and weaknesses of UTE, ΔR_2, and ΔR_2^* MRAs in visualizing and quantifying cerebral vessels by the existence of intra-vascular SPION. A synergistic combination of three MRAs was followed and resulting UTE-ΔR_2-ΔR_2^* combined MRA was produced. Finally, vascular parameters were extracted for comparison with each MRA. The advantages and disadvantages of each MRA were described and the synergistically merged UTE-ΔR_2-ΔR_2^* MRA was applied to validate the reduction of air–tissue interface artifact at the specific brain region and increased CNR for cerebral vessels in normal and tumor bearing rats.

3.2.2 Materials and Methods

Monte Carlo (MC) simulation

To examine the benefits from the synergistic multiplication of ΔR_2 and ΔR_2^*, Monte-Carlo simulations were performed. Cylinder-shaped vessel models with various diameters were created in a 3D space. To maximize the magnetic susceptibility mismatch, the direction of the Cylinder-shaped vessel was located perpendicularly to the main axis of susceptibility-induced magnetic field. The magnetic field strength was fixed at 7 T. The susceptibility-induced magnetic field in the extra-vascular region was shifted by the susceptibility interference in the presence of intra-vascular SPION filling the vessel and was estimated by using the FPM from a previously explained process [102-104].

Figure 3.2.1A shows the diffusible protons for each region in the 3D matrix for calculation of the values of ΔR_2 and ΔR_2^*. The m was represented as a region encircling the vessel surface. For the ΔR_2 and ΔR_2^* calculations, the SPION magnetic susceptibility ($\Delta\chi$) was 3×10^7 in CGS units and this value was converted into the dose of 240 μmol Fe/kg [102]. Afterward, 500000 protons were located randomly in the susceptibility-induced magnetic field shift space and the number of diffusible protons was enough for reproducible simulation results. All protons diffused with each increment of TE and stopped with the final increment of 5 ms and 15 ms for ΔR_2 and ΔR_2^* simulations, respectively. The diffusion length ($\sqrt{2D\Delta t}$) was defined as the standard deviation of movement of all protons. The time step of diffusion (Δt) was 0.2 ms and the diffusion coefficient (D) was 1×10^5 cm^2/s. As shown in **Figure 3.2.1A**, the susceptibility-induced magnetic field shift space was divided to estimate the values of ΔR_2 and ΔR_2^* as a function of distance from surface of the cylinder-shaped vessel. The accumulated phase of diffusible protons within each region m during time t in the susceptibility-induced shift of magnetic field space was calculated by below equation:

$$\varphi_{m,n}(\mathrm{t}) = \sum_{i=1}^{t/\Delta t} \gamma \Delta B(P_{mn}(i\Delta t))\Delta t \qquad (3.2.1)$$

where Δt is the time step of diffusion, t is the final increment of TE, γ is the gyromagnetic ratio for a proton (2.675×10^8 rad/T/s), $P_{mn}(t)$ is the location of the nth proton at time t within specific region m, $\Delta B(P_{mn})$ is the susceptibility-induced shift of magnetic field at location P_{mn} within specific region m. The signal intensities were evaluated by using the average of all added phase of total diffusible N spins for each region m:

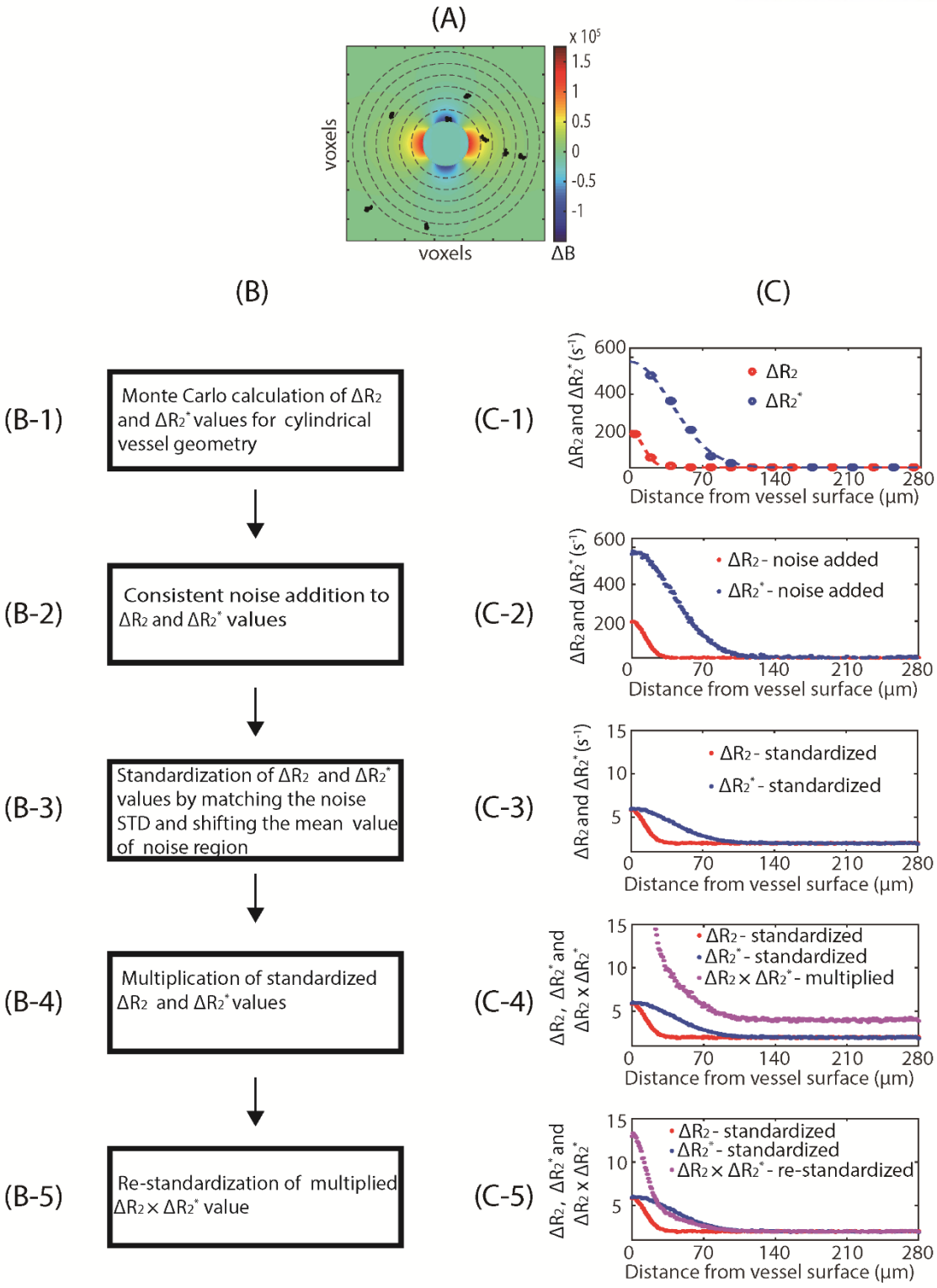

Figure 3.2.1 Simulation description and work flow for standardization of ΔR_2, ΔR_2^* and $\Delta R_2 \times \Delta R_2^*$. (A) Diffusible spins in the susceptibility-induced shift of magnetic field space with a cylinder-shaped vessel. (B) Process chart for ΔR_2, ΔR_2^* and $\Delta R_2 \times \Delta R_2^*$ standardization. (C) The results of step-wise simulation following the process chart in (B).

$$S_m(t) = \frac{1}{N}\sum_{n=1}^{N} e^{i\varphi_{mn}(t)} \qquad (3.2.2)$$

For simulation by using spin echo signal, the accumulated phase of each diffusible proton was calculated by subtraction of proton phase before and after the π pulse [105]. The resultant ΔR_{2m} and ΔR_{2m}^* for each region m were calculated as follows:

$$\Delta R_{2m}, R_{2m}^* = -\frac{\ln(S_m(TE))}{TE} \qquad (3.2.3)$$

The values of ΔR_{2m} and ΔR_{2m}^* were defined as the center of each region m. The protons diffusing across the adjacent regions were excepted for computation of relaxation rates. **Figure 3.2.1B** and **C** illustrates the workflow for standardization of the calculated values of ΔR_2, ΔR_2^* and $\Delta R_2 \times \Delta R_2^*$. The standardizing process was required to compare and synergistically combine different MRAs. First of all, the estimated values of ΔR_2 and ΔR_2^* for region m from FPM simulations were fitted by using a Gaussian with a function of distance from surface of the cylinder-shaped vessel as shown in **Figure 3.2.1B-1** and **C-1**. Second, the values of ΔR_2 and ΔR_2^* was added to white random noise, as shown in **Figure 3.2.1B-2** and **C-2**. Particularly, the standard deviation of ΔR_2^* in the noise region was set to be three times greater than that of ΔR_2. In the standard deviation from ΔR_2^* at TE 5 ms and ΔR_2 at TE 15 ms by using **Equation 3.2.3**, the experimental noise magnitudes of ΔR_2 and ΔR_2^* MRAs were similar with simulation results. Third, each amplitude was adjusted and moved to quantitatively compare and multiply ΔR_2 and ΔR_2^* as shown in **Figure 3.2.1B-3** and **C-3**. Each amplitude was adjusted for matching the standard deviations of ΔR_2 and ΔR_2^* of the no signal region away from surface of the cylinder-shaped vessel, so that consistent standard of the threshold can be used for both groups. The shifting of ΔR_2 and ΔR_2^* prevented miscalculation by small numbers close to zero in the noise region. Fourth, standardized ΔR_2 and ΔR_2^* values were multiplied each other, as shown in **Figure 3.2.1B-4** and **C-4**. Finally, the re-standardization for multiplied ΔR_2 and ΔR_2^* values was performed to compare quantitatively of ΔR_2, ΔR_2^* and $\Delta R_2 \times \Delta R_2^*$, as shown in **Figure 3.2.1B-5** and **C-5**.

Cell and animal preparation

The IACUC of the Ulsan National Institute of Science and Technology approved this study. To perform *in vivo* MR experiments, eleven Sprague–Dawley (SD) rats were used. The six SD rats were investigated for vasculature of normal SD rat's brain. The remaining of SD rats were injected with C6 glioma (ATCC CCL-107) cells into their left hemisphere of the brain as follows. For injection of C6 glioma cells into the brain, frozen cell stock were melted and preserved in Dulbecco's modified Eagle

medium (DMEM, 450 ml) with penicillin–streptomycin (PS, 5 mL) and 10% fetal bovine serum (FBS, 50 mL). The melted C6 glioma cells were placed in an incubator with 100% humidity and 5% CO_2 at 37 °C. After culture, the DMEM was eliminated and the suspension of C6 glioma cells with PBS was made for injection into rat brains. The rat was positioned in a Lab Standard stereotaxic instrument (Stoelting Co., Wood Dale, IL, USA) with micro-infusion pump. The scalp incision was performed along the middle line of the rat's head. A burr hole with 0.5 mm diameter was made in the skull at anterior 1.5 mm, lateral 3 mm and depth 2mm from the bregma. The suspension of 1.5×10^6 C6 glioma cell with PBS was slowly inserted into the brain regions of the striatum and cortex by using a micro-infusion pump and a Hamilton syringe (Hamilton, Reno, NV, USA). After the end of the injection, the needle for C6 glioma cell injection was slowly removed for 30 min and the scalp was sutured.

MRI acquisition protocol

All MR images were obtained with a 7 T animal MRI scanner (Bruker, Ettlingen, Germany) using a volume coil. The anesthesia for animals was maintained with a mixture of 70% nitrous oxide, 30% oxygen with 1.5% isoflurane. And the body temperature of animals was kept with 37 ± 1 °C by using linked an animal bed and a warm-water circuit. To determine ΔR_2 and ΔR_2^* MRAs, T_2- and T_2^*-weighted images were obtained before and after circulation of SPION. T_1-weighted image for UTE MRA was acquired after injection with SPION. SPION was administrated at a dose 120 μmol Fe/kg for UTE MRA, 240 μmol Fe/kg for ΔR_2^* MRA and 360 μmol Fe/kg for ΔR_2 MRA. In other words, SPION of 120 μmol Fe/kg was injected sequentially. The features of SPION for the MRAs have been widely investigated in a prior study. The relaxivities of r_1 and r_2 of SPION at 7 T were 2.36 $mM^{-1}s^{-1}$ and 32.94 $mM^{-1}s^{-1}$, respectively. The acquiring images after SPION injection was postponed for 1–2 min until the distribution of SPION in the vessels was stable. The MR imaging parameters for the UTE sequence were as follows: FA = 20°; TR = 12 ms; TE = 0.012 ms; FOV = 30 × 30 × 60mm^3; matrix size = 384 × 384 × 384. The MR imaging parameters for the FLASH sequence were as follows: FA = 20°; TR = 80 ms; TE = 5.27 ms; FOV = 30 × 30 × 33.12 mm^3; matrix size = 384 × 384 × 212. The MR imaging parameters for the TSE sequence were as follows: TR = 2000 ms; effective TE = 15 ms; TSE factor = 4; FOV = 30 × 30 × 33.12 mm^3; matrix size = 384 × 384 × 212.

MRA processing for vessel segmentation and quantification

Image processing and associated analysis to segment and quantify vasculatures were performed using MATLAB (R2014b, The Math Works Inc., Natick, MA, USA). All MR images were applied by pre-process to compare and combine ΔR_2, ΔR_2^*, and UTE MRAs. ΔR_2 and ΔR_2^* values were normalized based on the signal intensity of the UTE MRA for standardization of the signal intensity histogram. Described procedure of the generation steps for standardization was explained as shown in **Figure 3.2.2**.

First, the signal intensities of the all MR images were normalized by using the average value of signal intensity in the temporalis muscle (TM) [106]. The TM region presented no noticeable increasing signal variation by SPION, and this normalization by an average of TM signal compensated for any signal bias of MR images. All MR images were covered by whole brain ROI which was obtained by using the method of intensity-based ROI extraction from the TSE image before SPION injection. Second, voxel-wise ΔR_2 and ΔR_2^* maps were estimated using the following equation:

$$\Delta R_2^* \text{ and } \Delta R_2 = \frac{1}{TE}\ln\left(\frac{S_{pre}}{S_{post}}\right) \qquad (3.2.4)$$

where TE is the echo time, and S_{pre} and S_{post} are the signal intensities before and after SPION injection with spin echo for ΔR_2 and gradient echo for ΔR_2^*. Third, the values of ΔR_2 and ΔR_2^* were estimated to standardize the those by using the related values of UTE MRA as shown in below equation:

$$S_{transf(\Delta R_2,\ \Delta R_2^*)}(x,y,z) = \left[S_{\Delta R_2,\ \Delta R_2^*}(x,y,z) \times A\right] + \left(\mu_{UTE} - \mu_{\Delta R_2,\ \Delta R_2^*}\right) \qquad (3.2.5)$$

where $S_{\Delta R2*,\Delta R2}(x,y,z)$ and $S_{transf(\Delta R2*,\Delta R2)}(x,y,z)$ are the signal intensities of input and transformed MRA, respectively [107, 108]. μ_{UTE} and $\mu_{\Delta R_2,\ \Delta R_2^*}$ are modes of UTE and input MRA. The mode means the value at the peak of each histogram. Standard deviations of signal intensities were calculated from values within a 30% range of each mode as criteria. The value of A was adjusted until the variance between the standard deviation of UTE and input signal intensity reduced below 0.001. This standardization between UTE, ΔR_2, and ΔR_2^* MRAs is necessary step to consistently compare each MRA. It can be feasible to apply same threshold value to all MRA and simultaneously segment vessels for all MRAs. Fourth, standardized ΔR_2 and ΔR_2^* MRAs were multiplied for the synergistic combination. To extract the brain surface, canny edge-detection method was applied to brain ROI [109]. The brain surface of multiplied ΔR_2 and ΔR_2^* MRAs were substituted with that of the UTE MRA. The processing equation for UTE-ΔR_2-ΔR_2^* combined MRA is described by:

$$\text{UTE}_{surface\ \&\ inner\ area} + \left[\Delta R_2^* \times \Delta R_2\right]_{inner\ area} \qquad (3.2.6)$$

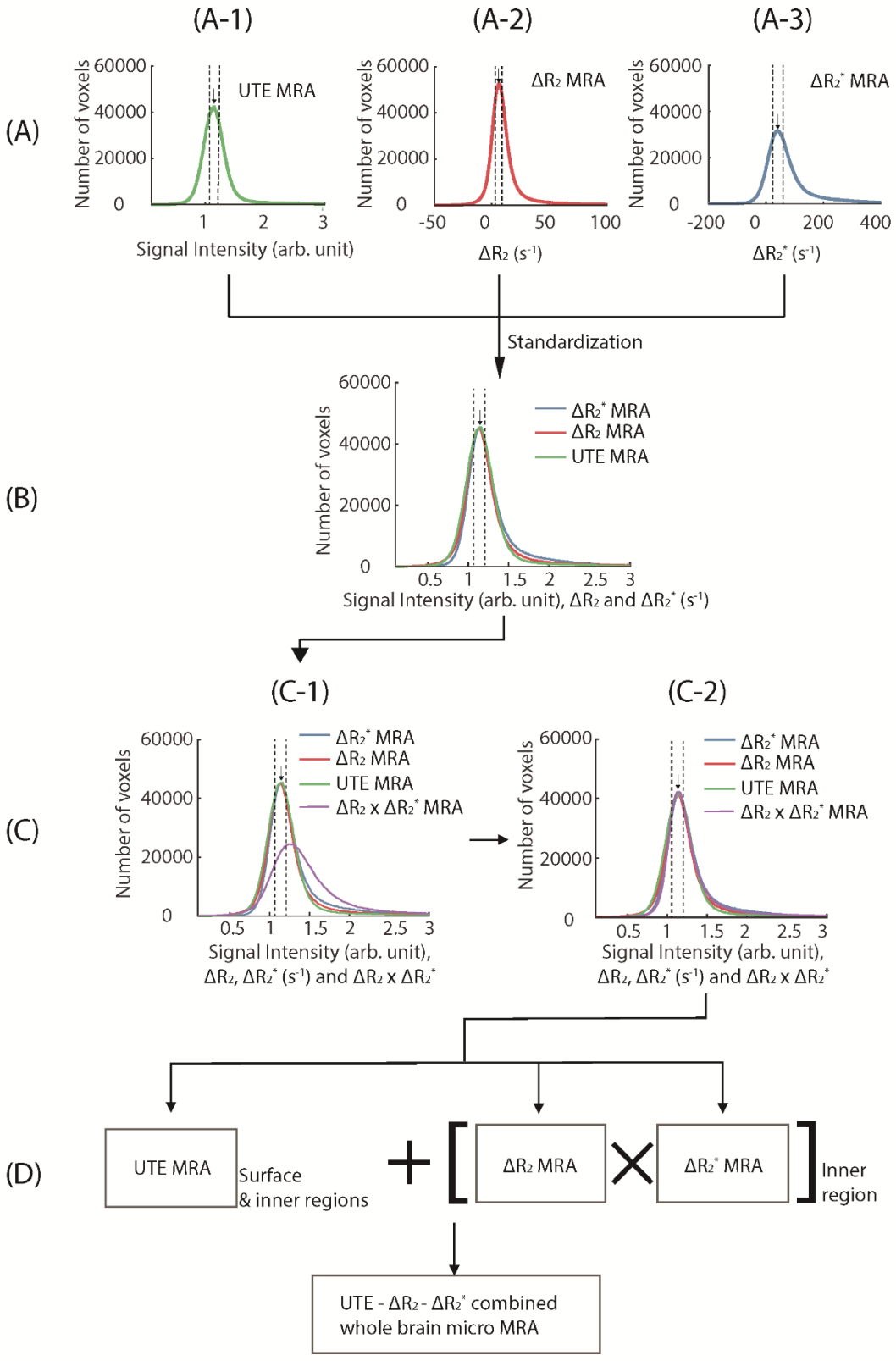

Figure 3.2.2 Schematic diagram of the standardization of each of UTE-, ΔR_2-, and ΔR_2^*-MRA.

The re-standardization of UTE-ΔR_2-ΔR_2^* combined MRA was performed to quantitatively compare each MRAs. This combination procedure of different MRAs is motivated from the investigation that the UTE MRA represented precise vessel on the brain surface with positively enhanced contrast, whereas the ΔR_2 and ΔR_2^* MRAs in the inner brain provided well-visible micro-vessels with expanded sizes of micro-vessels.

Lastly, the volume renderings of all MRAs were performed by using 3D Slicer (free software). The parts of bluish areas show tissue regions of the brain and the yellowish areas show vessels as shown in following MRA figures. The outside views of all MRAs were provided to visualize vessels on the surface area. Each MRA with a slab range of 2 mm thickness is shown with inside views to show inner vessels of the brain, containing cortex region of a rat's brain.

For the quantitative evaluation of vascular parameters from the various MRAs, the CNRs, vessel node/branch count and total vessel length per branch of each MRA were obtained. For the segmentation of vessels, 95% of the UTE signal intensity of the maximum value in the intensity histogram was set as a threshold value for the surface region, and a threshold value of 90% of the UTE signal intensity was used for the inner region of all MRAs. The threshold value for the surface region was higher than that for the inner region because the relatively small vessels with lower contrast were existed in the inner region. The CNRs of the vessel to tissue contrast were estimated by using the following equation:

$$\mathrm{CNR} = \frac{Vessel\ \ S.I. - Tissue\ \ S.I.}{Tissue\ \ std.} \qquad (3.2.7)$$

Tissue SI and Vessel SI were defined as average of standardized values of the each MRA in the tissue and vessel regions of the brain, respectively. Tissue std refers to the standard deviation of standardized values of the each MRA in the tissue regions of the brain. For the quantitative evaluation of the tumor region in rat brains, the tumor region ROI was obtained from the combined MRA using a seeded region growing algorithm with a threshold value set as 90% of the UTE signal intensity. The ROI in the ipsilateral tumor region was the same as that for the contralateral non-tumor brain region. As shown in **Figure 3.2.3**, the ROI of tumor region was mirrored on contralateral non-tumor regions. Then, CNRs by using the two ROIs were calculated and compared for analysis of the difference between non-tumor and tumor regions.

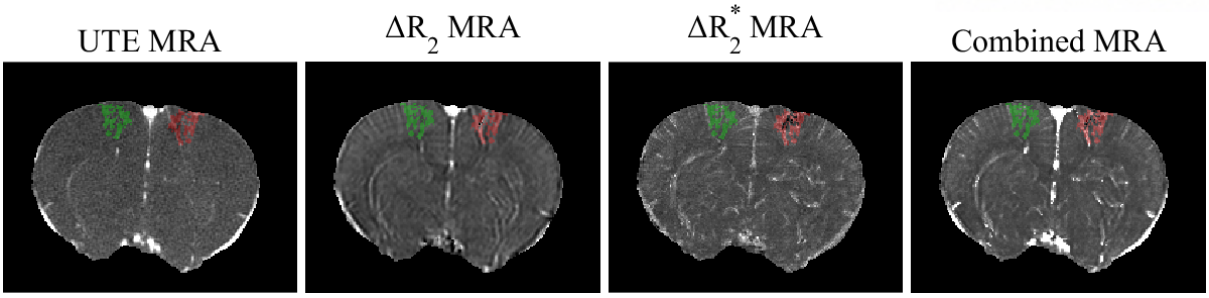

Figure 3.2.3 The ROI of the tumor region (green color) and the mirrored non-tumor region (red color)

To acquire the vascular parameters, segmented vessels of the brain were skeletonized by using a thinning algorithm [110]. The skeletonized vessels were transformed into a vessel network topology expressed by vessel nodes and branches [111]. The vessel branches are defined as lines of the skeletonized vessels, and contact point of two or more branches was indicated as a node. In the inner region, the cortex region with plentiful vessels was chosen by applying a cortex region ROI using the skeletons vessels. Total vessel length was evaluated by summing total skeletonized vessels. By dividing the total vessel length and the vessel branch count, total vessel length per branch was calculated.

3.2.3 Results

MC simulation

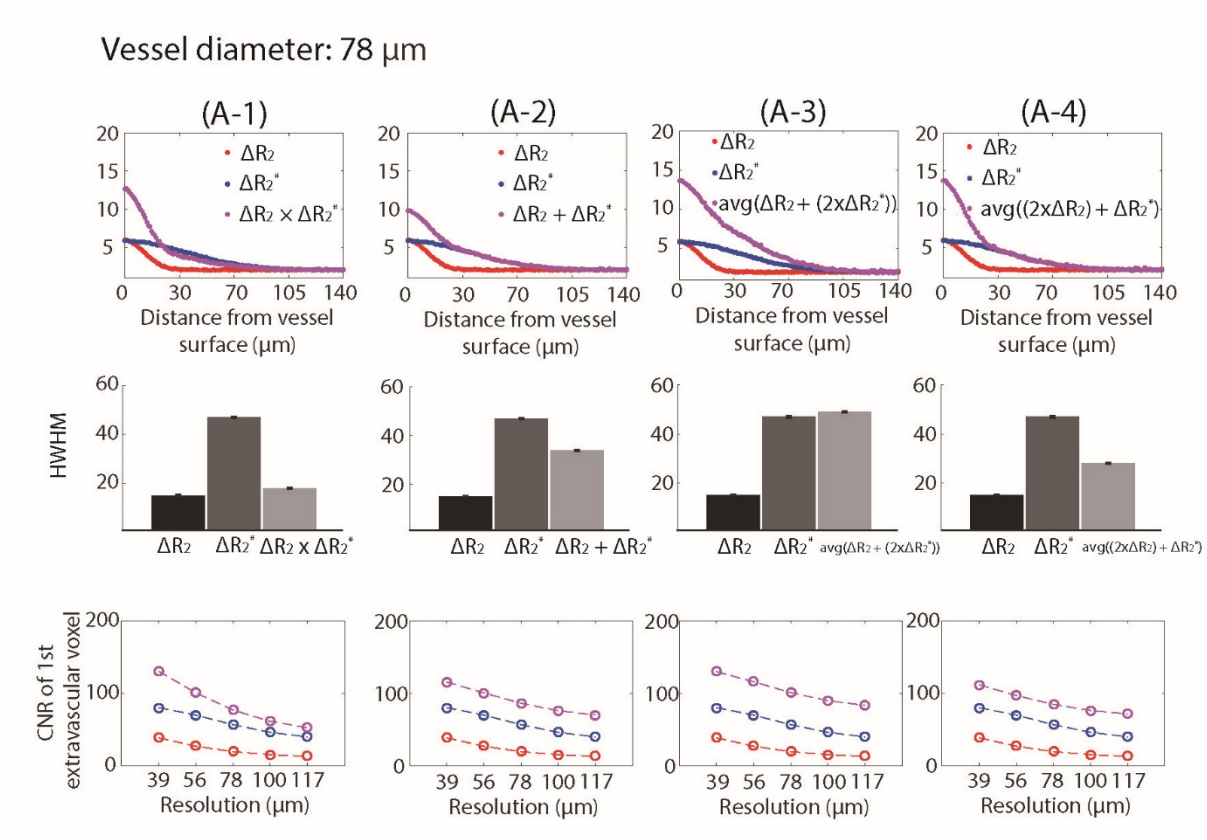

Figure 3.2.4 The behaviors of (A-1) $\Delta R_2 \times \Delta R_2^*$, (A-2) $\Delta R_2 + \Delta R_2^*$, (A-3) average of ΔR_2 and $2\times\Delta R_2^*$ and (A-4) average of $2\times \Delta R_2$ and ΔR_2^*.

To verify the effectiveness of multiplication ΔR_2 and ΔR_2^* in the purpose of reducing the size overestimation issue of ΔR_2^* MRAs, the investigation of the application possibility of some other operations to ΔR_2 and ΔR_2^* MRAs was performed. The results for summation and weighted average was shown in Figure **3.2.4**. The behaviors of $\Delta R_2 \times \Delta R_2^*$, $\Delta R_2 + \Delta R_2^*$, average of ΔR_2 and $2\times\Delta R_2^*$, and average of $2\times \Delta R_2$ and ΔR_2^* were plotted. The reason of the multiplication of ΔR_2 and ΔR_2^* can be understood by the results of HWHM (Half-width half-maximum) value for each case. To minimize vessel size overestimation, the information of vessel size in ΔR_2-MRA was very helpful. The HWHM of $\Delta R_2 \times \Delta R_2^*$ was closer to that of ΔR_2 than that of any other operations with enhanced CNR over conventional ΔR_2 and ΔR_2^* without necessity of imposing any arbitrary weighting factors.

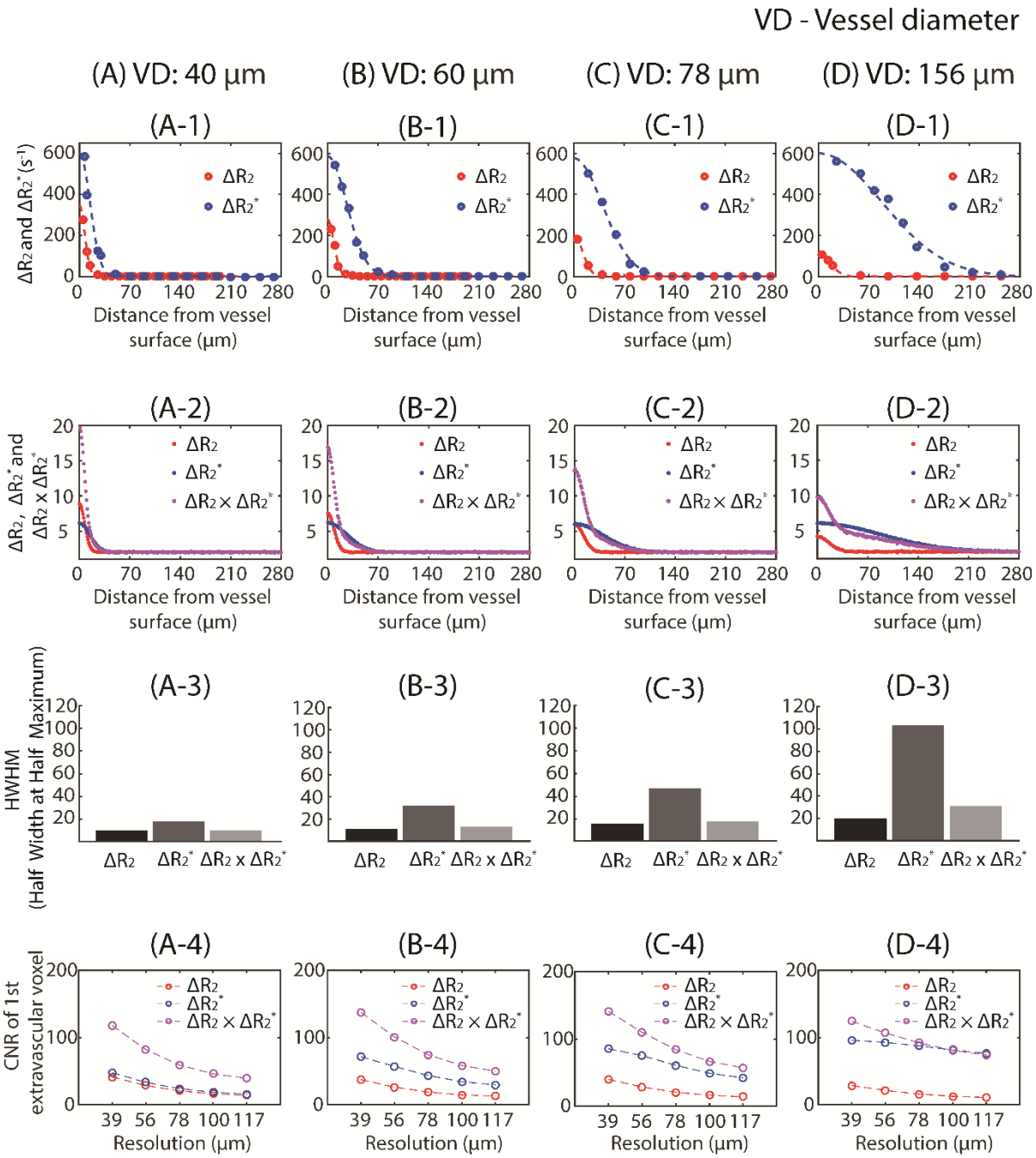

Figure 3.2.5 Simulation results with vessel diameters of 40, 60, 78 and 156 μm, respectively. (A-1), (B-1), (C-1), and (D-1) show the behaviors of ΔR_2 and ΔR_2^* with several vessel diameters. (A-2), (B-2), (C-2) and (D-2) show related standardized ΔR_2, ΔR_2^*, and $\Delta R_2 \times \Delta R_2^*$. (A-3), (B-3), (C-3) and (D-3) show the HWHM of ΔR_2, ΔR_2^*, and $\Delta R_2 \times \Delta R_2^*$. (A-4), (B-4), (C-4) and (D-4) show the CNRs of the first value of ΔR_2, ΔR_2^*, and $\Delta R_2 \times \Delta R_2^*$.

Figure 3.2.5 shows the behaviors of ΔR_2, ΔR_2^*, and $\Delta R_2 \times \Delta R_2^*$ with different vessel diameters as the distance away from the surface of cylinder shaped vessel. The red, blue, and purple lines correspond to behaviors of ΔR_2, ΔR_2^*, and $\Delta R_2 \times \Delta R_2^*$, respectively. In the behaviors of ΔR_2, the width of decay becomes slightly broader but the highest amplitude decreases with increasing vessel diameters. In the behaviors of ΔR_2^*, the highest amplitude is maintained at a similar level, whereas the width of decay drastically increases as vessel diameters increase as shown in **Figure 3.2.5A-1**, **B-1**, **C-1**, and **D-1**.

Standardized ΔR_2, ΔR_2^*, and $\Delta R_2 \times \Delta R_2^*$ values are superimposed together in **Figure 3.2.5A-2**, **B-2**, **C-2**, and **D-2** for various vessel diameters. The highest amplitudes of $\Delta R_2 \times \Delta R_2^*$ were drastically higher than that of individual ΔR_2 and ΔR_2^*, and the HWHM behaviors of $\Delta R_2 \times \Delta R_2^*$ followed that of ΔR_2^*, representing both increase of sensitivity for micro-vessels and reduction of observable vessel diameter overestimation by using the combining process of $\Delta R_2 \times \Delta R_2^*$.

Quantitatively, the HWHM values of ΔR_2, ΔR_2^*, and $\Delta R_2 \times \Delta R_2^*$ are shown in **Figure 3.2.5A-3**, **B-3**, **C-3**, **D-3** for various vessel diameters. The CNRs at the first voxel in the vessel surface were also estimated at various image resolutions as shown in **Figure 3.2.5A-4**, **B-4**, **C-4**, and **D-4**. The CNR value of the first voxel was calculated by average value of each decay curve within the related spatial resolution.

UTE, ΔR_2, ΔR_2^* and combined MRAs

A representative raw image of UTE after SPION circulation is shown in **Figure 3.2.6A**, and raw images of TSE and FLASH before and after SPION circulation are shown in **Figure 3.2.6B-1**, **B-2** and **Figure 3.2.6C-1**, **C-2**. The surface vessels of the brain with dorsal and lateral view from same subject were illustrated in **Figure 3.2.7**. In **Figure 3.2.7B-1**, observed vessel of ΔR_2^* MRA on the brain surface indicated by the white arrow was larger than of ΔR_2 MRA. Although vessels of ΔR_2^* MRA on the brain surface were seen better than those of ΔR_2 MRA, some vessels of ΔR_2^* MRA on the brain surface were messy and the description of vasculature was unclear due to strong air-tissue interface artifacts in and around the brain surface. The sizes of visible vessels of ΔR_2^* MRA on the brain surface also were seemed to overestimate their sizes when compared with the size of vascular structure on the brain surface from ΔR_2 MRA and UTE MRA, as shown in **Figure 3.2.7B-2** by indicated as the white arrows. Overall, vascular structures on the surface region from ΔR_2 and ΔR_2^* MRAs were hardly seen because of subtraction discrepancy of images before and after SPION injection.

Contrastively, the brain vasculatures on the surface of UTE MRA (**Figure 3.2.7A-3** and **B-3**) seemed to well-defined the arterial and venous on the brain surface than those of ΔR_2 and ΔR_2^* MRAs (**Figure 3.2.7A-1**, **B-1**, **A-2**, and **B-2**). For this reason, the surface of UTE-ΔR_2-ΔR_2^* combined MRA was primarily replaced with that of UTE MRA. Multiplication of ΔR_2 and ΔR_2^* MRAs on the brain surface did not improve the description, as shown in **Figure 3.2.7A-4** and **B-4**. The vessels of the surface region in

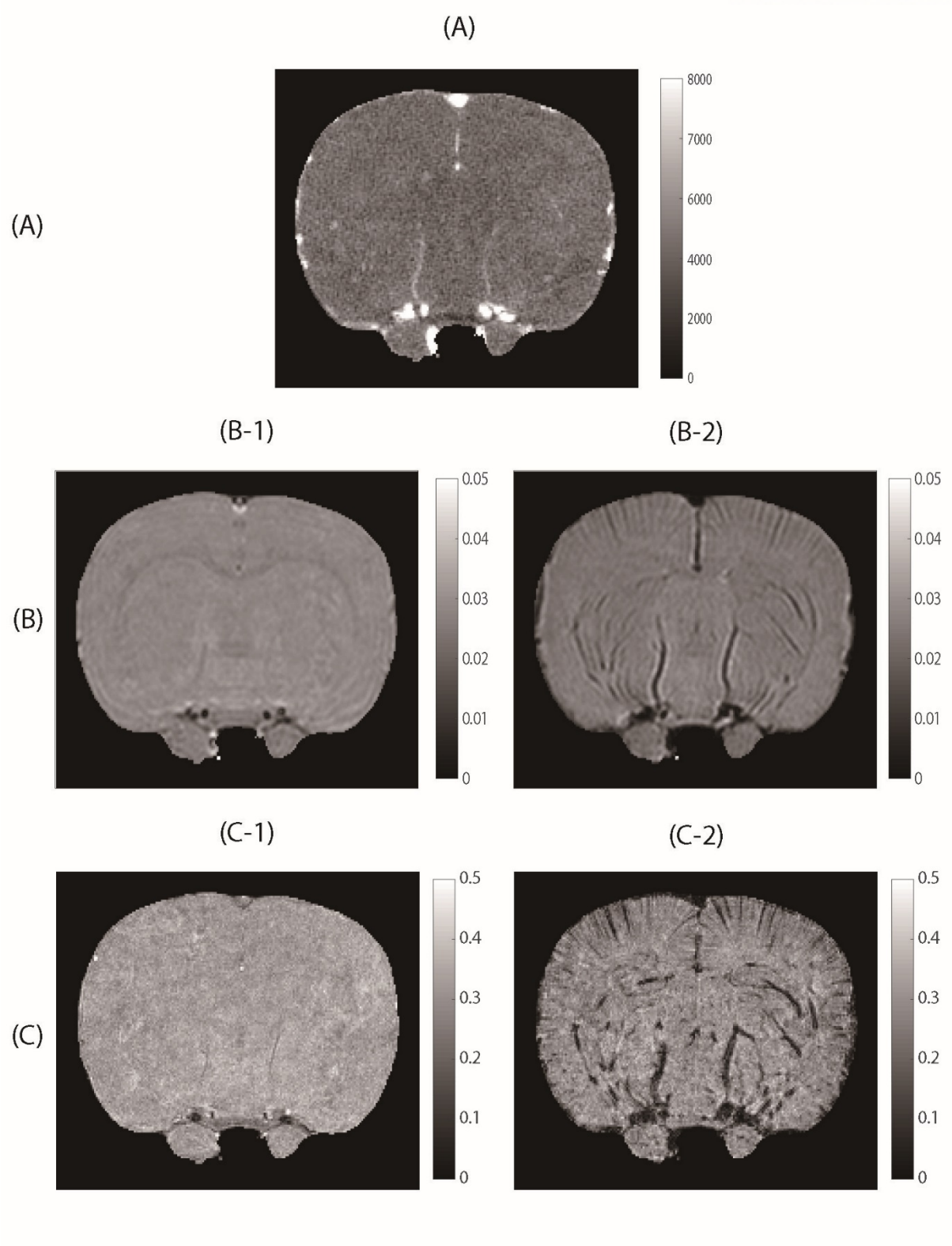

Figure 3.2.6 Anterior-to-posterior view of a normal rat: (A) Post-injection T_1-weighted image from UTE. (B-1) and (B-2) TSE pre and post-injection T_2-weighted images. (C-1) and (C-2) FLASH pre and post-injection T_2^*-weighted images.

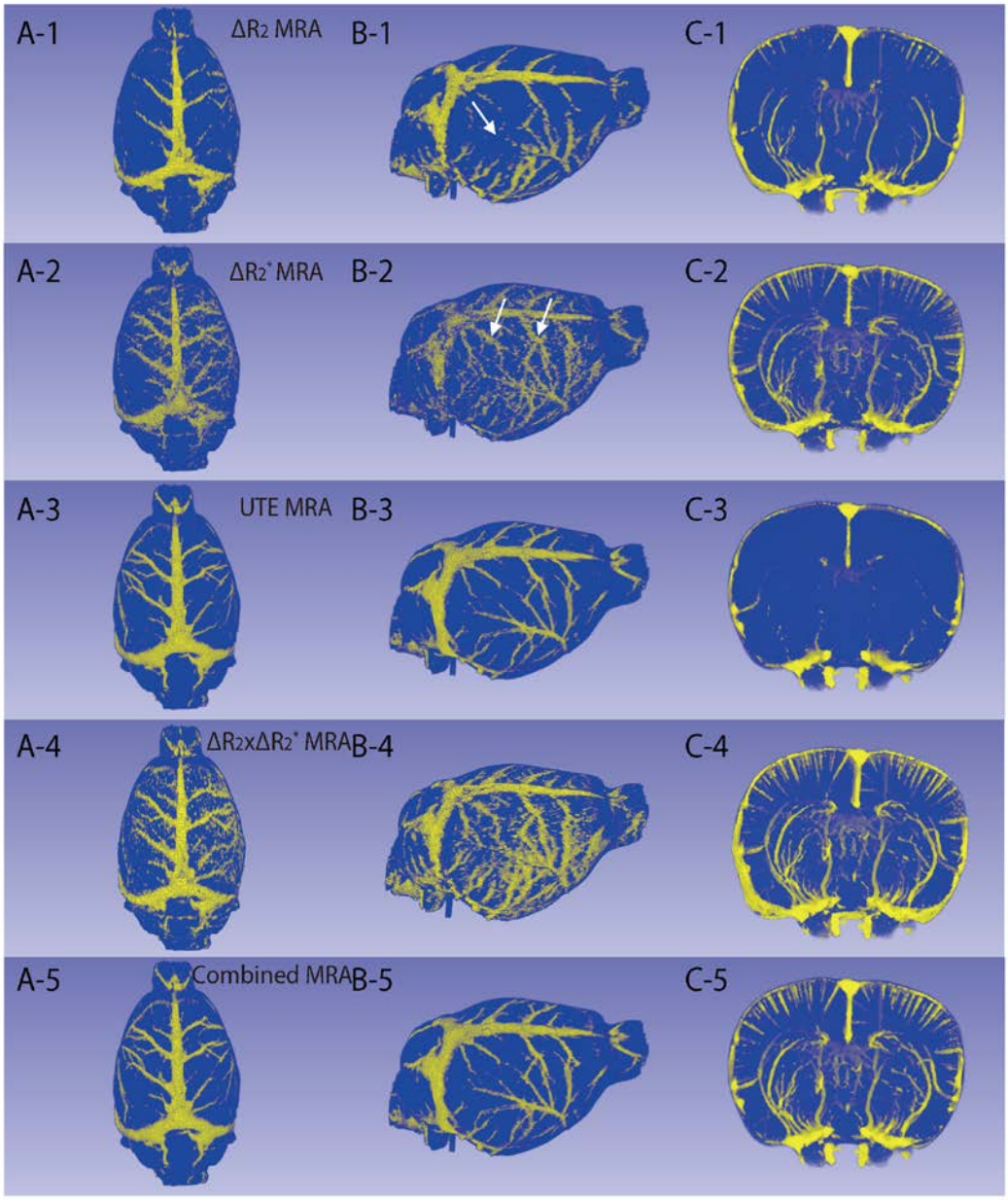

Figure 3.2.7 MRA of a normal rat brain from three orthogonal views. (A-1), (A-2), (A-3), (A-4), and (A-5) show ΔR_2, ΔR_2^*, UTE, $\Delta R_2 \times \Delta R_2^*$ and UTE + $\Delta R_2 \times \Delta R_2^*$ combined MRAs along the dorsal and ventral direction, respectively. (B-1), (B-2), (B-3), (B-4), and (B-5) show ΔR_2, ΔR_2^*, UTE, $\Delta R_2 \times \Delta R_2^*$ and UTE + $\Delta R_2 \times \Delta R_2^*$ combined MRAs with lateral views, respectively. (C-1), (C-2), (C-3), (C-4), and (C-5) show ΔR_2, ΔR_2^*, UTE, $\Delta R_2 \times \Delta R_2^*$ and UTE + $\Delta R_2 \times \Delta R_2^*$ combined MRAs along the anterior posterior direction with 2 mm thick slab sections, respectively. The white arrow in (B-1) represents the ambiguous region from the surface region of ΔR_2 MRA; the white arrows in (B-2) represent the over-estimated vessel diameters on the surface region of ΔR_2^* MRA.

$\Delta R_2 \times \Delta R_2^*$ MRA were hardly defined due to increased air-tissue interface artifacts in and around the surface of the rat's brain.

In **Figure 3.2.7C,** deep brains of each MRA with thickness of identical slab are shown along the anterior-to-posterior direction. As shown in **Figure 3.2.7C-1** and **C-2**, the number of detected vessels in the cortex of ΔR_2^* MRA was remarkably greater than that in the cortex of ΔR_2 MRA due to the relatively smaller diameters of the vessels than the spatial resolution of 3D MRA in the cortex region. The choroidal arterioles and cortical penetrating vessels from UTE MRA were hardly detected. However, the region of the arterial circle of willis in the deep brain from UTE MRA was showing well. The method of multiplying ΔR_2 and ΔR_2^* MRAs and adding UTE MRA was based on these observed results for complementation of the vessel sensitivity and the overestimated vessel diameters of ΔR_2 and ΔR_2^* MRA. As shown in **Figure 3.2.7C-4**, inner region of $\Delta R_2 \times \Delta R_2^*$ MRA was similar to that of UTE-ΔR_2-ΔR_2^* combined MRA. The resulting UTE-ΔR_2-ΔR_2^* combined MRA is shown in **Figure 3.2.7C-5**, synergistic complementation of the individual MRAs.

To precisely evaluate each MRA, the analysis by using line profile was applied to various brain regions. As shown in **Figure 3.2.8A-2**, the overestimation of vessel diameter in ΔR_2^* MRA (blue) was obvious in comparison with that in ΔR_2 MRA (red) for a comparatively large vessel diameter. The combined UTE-ΔR_2-ΔR_2^* MRA (yellow) shows enhanced vessel-to-tissue contrast and compensated vessel diameter, as reported by the simulation results. As shown in **Figure 3.2.8A-3**, the relatively smaller vessels in the cortex region were hardly observed in UTE (green) and ΔR_2 MRA (red), but were noticeable in ΔR_2^* MRA (blue) and combined UTE-ΔR_2-ΔR_2^* MRA (yellow). Also, it was related to the simulation results for smaller vessels. The improvement of vessel-to-tissue contrast and reduction effect of vessel diameter overestimation were visible in the cerebellum region as shown in **Figure 3.2.8B-2**. The cortical region illustrated in **Figure 3.2.8C-2**, the line profile (green) of UTE MRA demonstrated that the regions of the vessel and brain tissue were indistinguishable, but the line profiles of ΔR_2 and ΔR_2^* MRAs exhibited difference between values of the tissue and vessel of the brain. The line profile of UTE-ΔR_2-ΔR_2^* combined MRA showed that vessel-to-tissue contrast of observed whole vessels were higher than any of the MRAs. Nonetheless, the reduction effect of vessel diameter overestimation was ambiguous for the smaller vessels because that effect tends to reduce for smaller vessels according to the simulation results. In addition, the values of ΔR_2 and ΔR_2^* MRA from region of the arterial circle of willis were vague, but these vessel regions can be described visibly in UTE MRA.

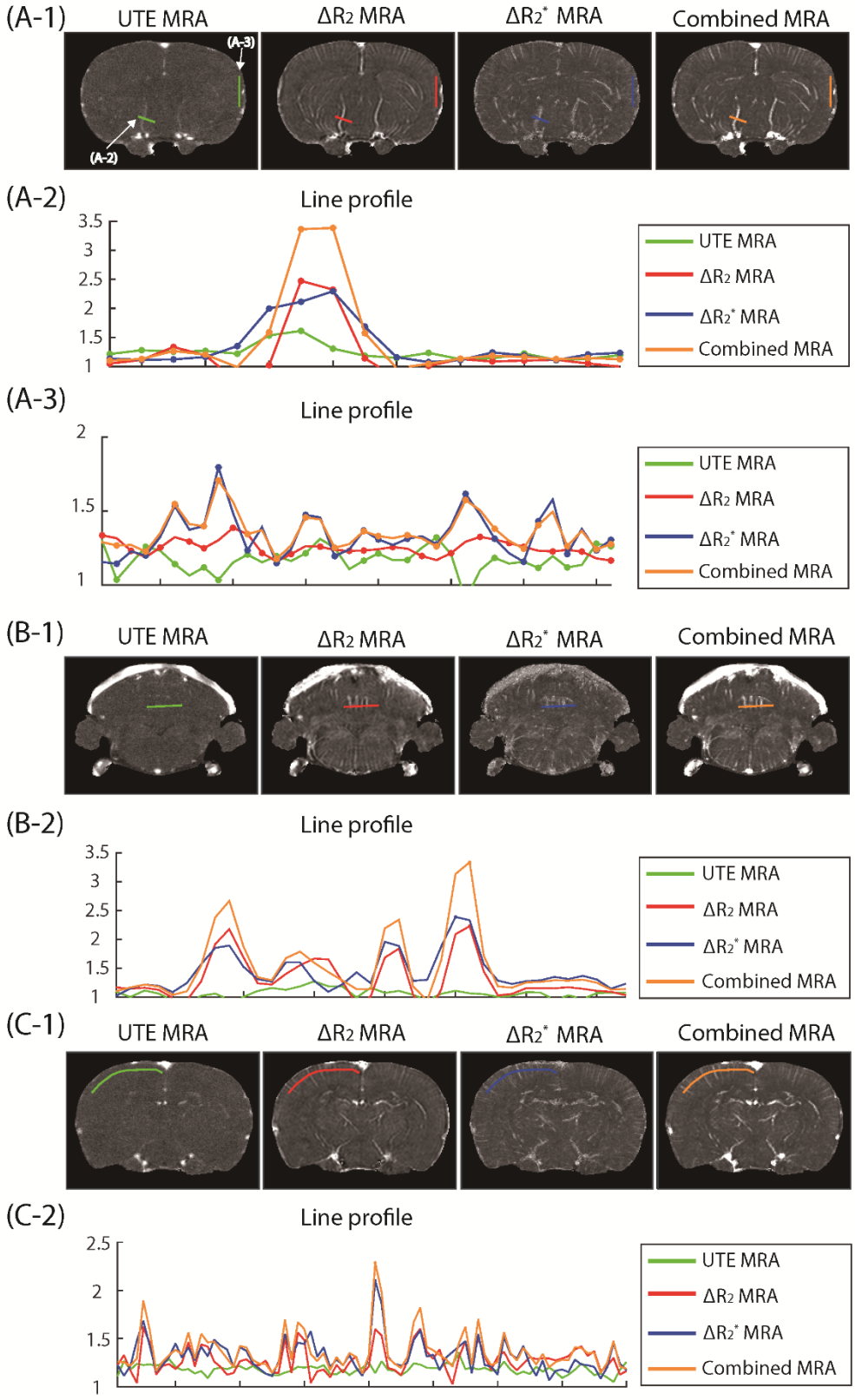

Figure 3.2.8 Comparison of line profiles from UTE (green), ΔR_2 (red), ΔR_2^* (blue), and UTE-ΔR_2-ΔR_2^* combined (yellow) MRA in various brain regions.

Quantification of vessel parameters for individual and combined MRAs

For comparison of vascular parameters of each MRAs, CNR, vessel node/branch count, and, total vessel length per branch for the whole brain regions were summarized in **Figure 3.2.10A** and **Figure 3.2.10B**. The CNRs were estimated by using a vessel segmented mask as shown in **Figure 3.2.9A-1** and **B-1** and other parameters were evaluated by using skeletonized vessel as shown in **Figure 3.2.9A-2** and **B-2**.

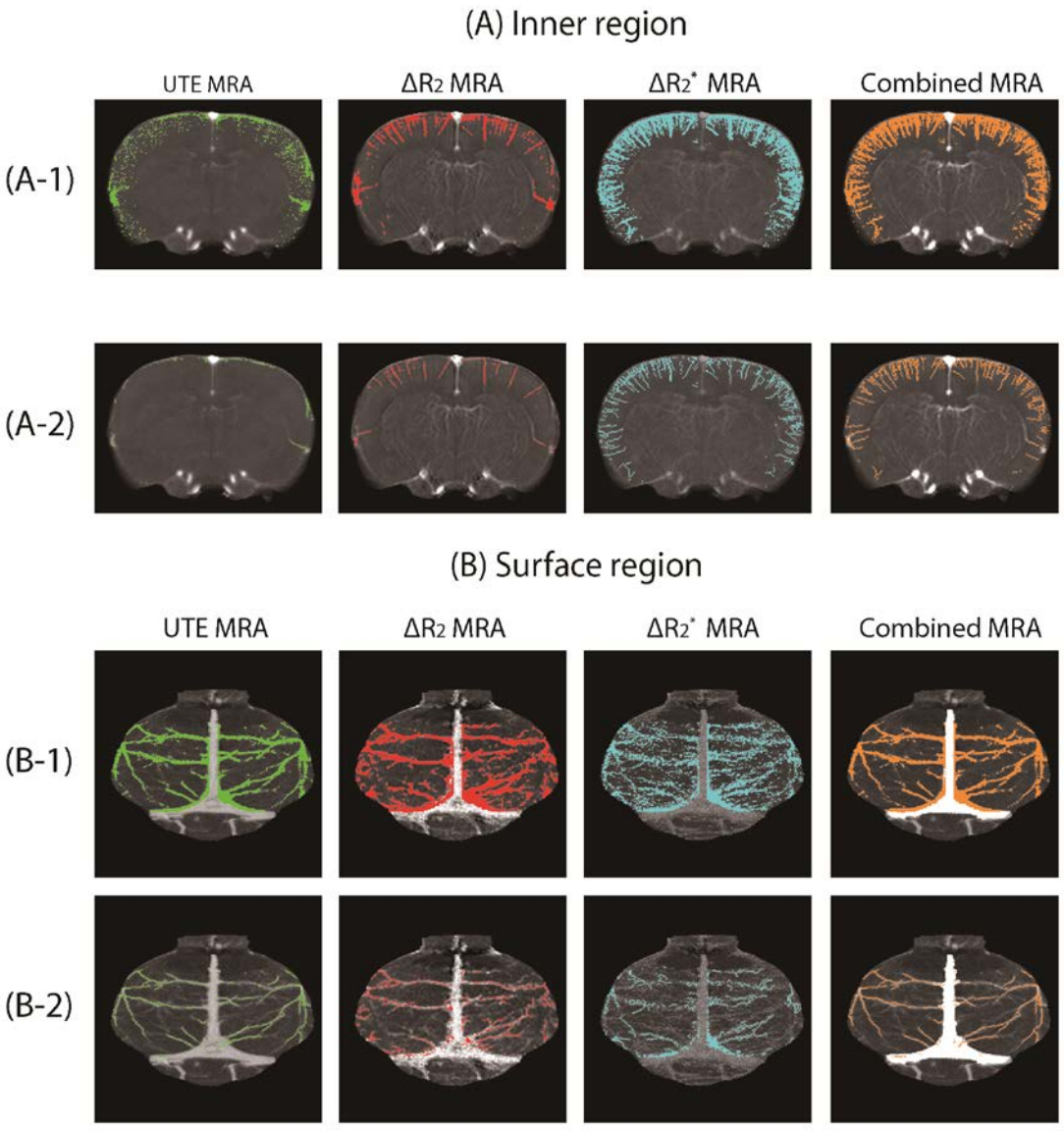

Figure 3.2.9 Vessel segmentation of inner and surface regions. (A-1) Vessel segmentation of the inner region (cortex) of the brain with 90% thresholding. (A-2) Corresponding skeletonized vessel network topology of the inner region (cortex) of the brain. (B-1) Vessel segmentation of the surface region of the brain with 95% thresholding. (B-2) Corresponding skeletonized vessel network topology of the surface region of the brain.

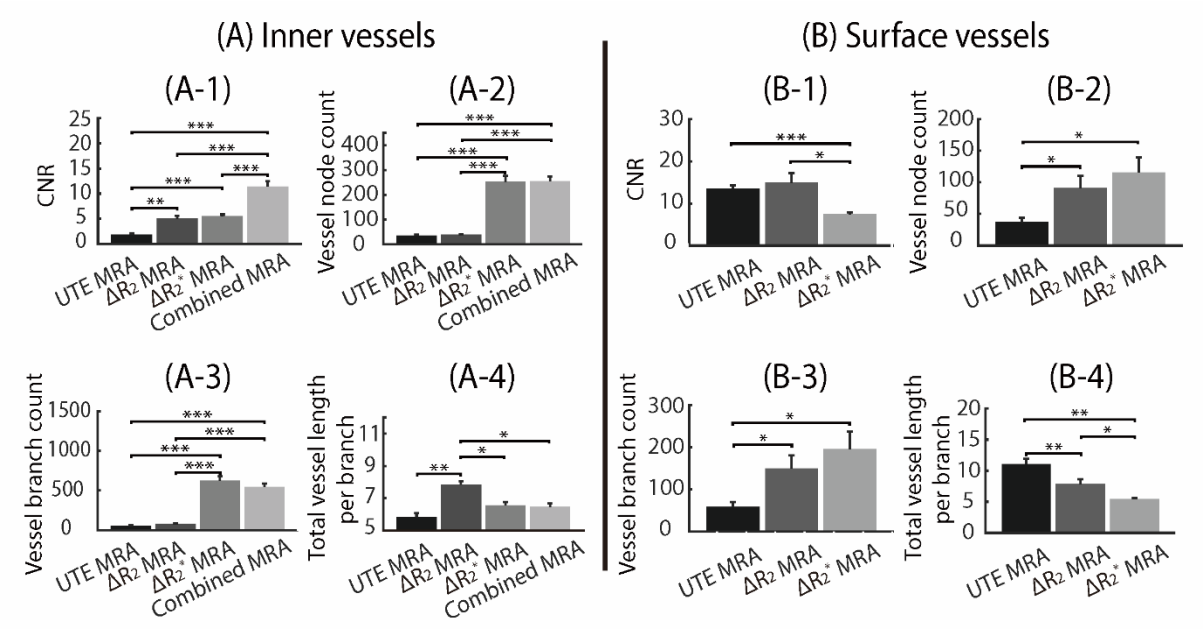

Figure 3.2.10 Quantification of vascular parameters in whole brain. (A) The vessel parameters of the inner brain region for UTE-, ΔR_2-, ΔR_2^*-, and UTE-ΔR_2-ΔR_2^* combined MRAs. (B) The vessel parameters of the brain vessel on the surface region for UTE-, ΔR_2-, and ΔR_2^*-MRA. For statistical analysis, Paired t-tests were performed to compare between individual and combined MRAs. One asterisk (*) indicates a p-value less than 0.05 ($p < 0.05$). Two asterisks (**) indicate p-values smaller than 0.01 ($p < 0.01$). Three asterisks (***) indicate p-values smaller than 0.001 ($p < 0.001$).

In the brain inner region, the CNR of the UTE-ΔR_2-ΔR_2^* combined MRA was greater than those of the individual MRAs and this result directly confirms from the analysis by using line profile as shown in **Figure 3.2.8**. The vessels of the inner region from UTE MRA provided the lowest CNR because those of the inner region were rarely noticed, as shown in **Figure 3.2.10A-1**. The node and branch count of vessel from ΔR_2^* and UTE-ΔR_2-ΔR_2^* combined MRAs were greater than those from UTE and ΔR_2 MRAs, as shown in **Figure 3.2.10A-2** and **A-3**. As shown in **Figure 3.2.10A-4**, only ΔR_2 MRA showed a statistic difference in total vessel length per branch because comparative long vasculatures were detected. **Table 3.2.1** summarizes the vascular parameters of the inner region for the six rat's brains.

For the surface region of the brain, the CNRs of UTE and ΔR_2 MRAs were greater than those of ΔR_2^* MRA. This is likely to an effect of the sporadic vessels of ΔR_2^* MRA caused by air-tissue interface artifacts. Correspondingly, node and branch count of ΔR_2^* MRA were statistically greater than for the other MRAs. But this result probably was related to air-tissue interface artifacts. On the other hand, the total vessel length per branch inclined to decrease in the order of UTE, ΔR_2, and ΔR_2^* MRAs and represents that vessel of UTE MRA on the surface were relatively longer than other MRAs, as described

in **Figure 3.2.10B-4**. **Table 3.2.2** summarizes the vascular parameters of the surface region for the six rat's brains.

		Rat 1	Rat 2	Rat 3	Rat 4	Rat 5	Rat 6
CNR	UTE MRA	1.48	3.13	2.24	1.29	1.44	1.68
	ΔR_2 MRA	5.18	6.32	7.23	4.37	2.71	4.20
	ΔR_2^* MRA	5.57	6.58	6.16	4.60	3.99	5.93
	Combined MRA	11.47	14.11	14.94	10.07	7.27	10.68
Vessel node count	UTE MRA	38	23	45	52	34	25
	ΔR_2 MRA	35	30	48	41	43	38
	ΔR_2^* MRA	336	172	271	185	288	263
	Combined MRA	264	168	271	284	325	212
Vessel branch count	UTE MRA	60	48	62	74	42	47
	ΔR_2 MRA	79	34	95	72	87	82
	ΔR_2^* MRA	823	481	710	389	668	651
	Combined MRA	601	370	590	567	678	470
Total Vessel length per branch (Total vessel length)	UTE MRA	5.30 (318)	6.88 (330)	5.10 (316)	6.39 (473)	5.74 (241)	5.64 (265)
	ΔR_2 MRA	8.56 (676)	7.44 (253)	7.13 (677)	8.29 (597)	7.56 (658)	8.16 (669)
	ΔR_2^* MRA	6.57 (5409)	7.01 (3370)	6.71 (4764)	5.65 (2198)	6.15 (4109)	7.28 (4737)
	Combined MRA	6.61 (3971)	7.11 (2631)	6.93 (4090)	5.72 (3242)	5.76 (3902)	6.71 (3153)

Table 3.2.1 Summary of vascular parameters for UTE-, ΔR_2-, ΔR_2^*-, and UTE-ΔR_2- ΔR_2^* combined MRAs of the inner brain region for all normal rats.

		Rat 1	Rat 2	Rat 3	Rat 4	Rat 5	Rat 6
CNR	UTE MRA	11.66	15.05	12.13	11.43	13.85	16.79
	ΔR_2 MRA	16.69	16.22	20.76	10.71	4.77	20.31
	ΔR_2^* MRA	7.87	7.76	8.12	6.01	5.98	8.98
Vessel node	UTE MRA	32	27	71	23	49	20
	ΔR_2 MRA	142	19	105	90	144	47

count	ΔR_2^* MRA	195	22	120	149	145	64
Vessel branch count	UTE MRA	57	58	105	33	76	23
	ΔR_2 MRA	225	28	173	143	249	78
	ΔR_2^* MRA	330	38	207	268	238	92
Total Vessel length per branch (Total vessel length)	UTE MRA	11.93 (680)	15.26 (885)	9.48 (995)	9.61 (317)	10.01 (761)	10.13 (233)
	ΔR_2 MRA	6.54 (1471)	11.75 (329)	8.46 (1464)	7.20 (1029)	6.37 (1585)	6.69 (522)
	ΔR_2^* MRA	5.38 (1777)	5.13 (195)	5.83 (1207)	4.64 (1244)	5.64 (1343)	5.80 (534)

Table 3.2.2 Summary of vascular parameters for UTE-, ΔR_2-, ΔR_2^*-, and UTE-ΔR_2- ΔR_2^* combined MRAs of the surface brain region for all normal rats.

MRA of brain tumor

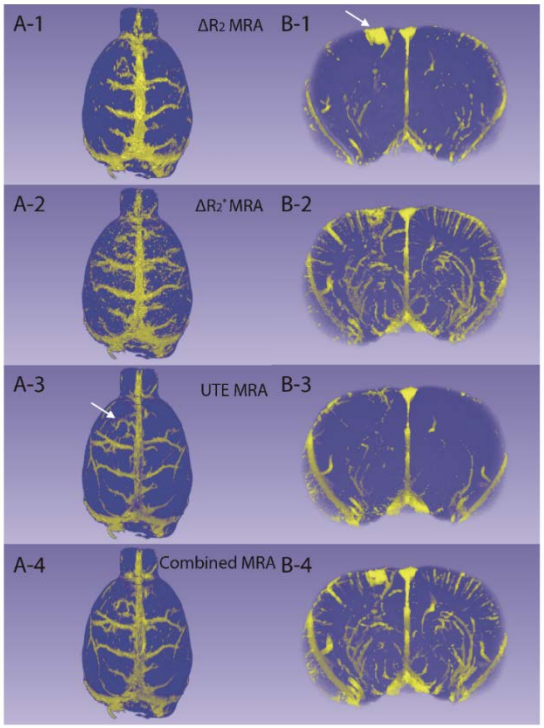

Figure 3.2.11 MRA of a C6 tumor bearing rat in external and internal views: panels (A-1), (A-2), (A-3), and (A-4) show dorsal views of UTE-, ΔR_2-, ΔR_2^*-, and UTE-ΔR_2-ΔR_2^* combined MRAs, respectively. Panels (B-1), (B-2), (B-3), and (B-4) show posterior-to-anterior views of UTE-, ΔR_2-, ΔR_2^*-, and UTE-ΔR_2-ΔR_2^* combined MRAs, respectively, with 1.56 mm thick slab selections. White arrows indicate tumor peripheral vasculature in the surface region from UTE MRA.

In the **Figure 3.2.11A**, the tumor peripheral vasculature of UTE MRA on the brain surface was detected and delineated better than with ΔR_2 and ΔR_2^* MRAs, as indicated by white arrow. The vessel-to-tissue contrast of the tumor region in the cortex region were dissimilar between each MRAs, as shown in **Figure 3.2.11B**. The region of tumor vasculature in the cortex of ΔR_2 and ΔR_2^* MRAs was broadly revealed as shown in **Figure 3.2.11B-1** and **B-2**. But, it was hard to differentiate the tumor edge of ΔR_2^* MRA alone due to the signal reduction of the T_2^* image before SPION injection by the strong T_2^* effect. The contrast of tumor region from ΔR_2 MRA was greater than those from UTE and ΔR_2^* MRAs. The contrast of tumor in the cortex region of UTE MRA was relatively low as shown in **Figure 3.2.11B-3**. Consequently, the UTE-ΔR_2-ΔR_2^* combined MRA provided both well-defined peripheral vessels of tumor on the surface and improved contrast of tumor region in the cortex, as shown in **Figure 3.2.11A-4** and **B-4,** respectively.

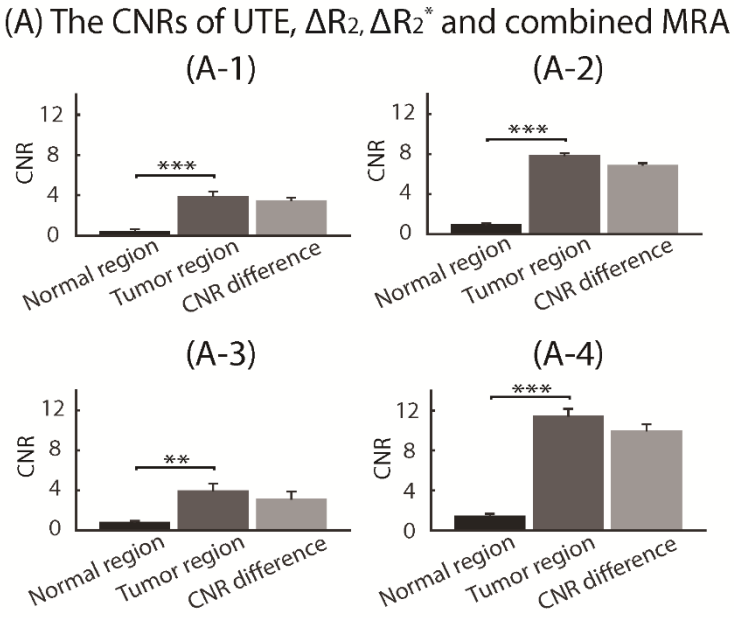

Figure 3.2.12 Comparison of CNRs between intra-cortical normal and tumor brain regions for (A-1) UTE-, (A-2) ΔR_2-, (A-3) ΔR_2^*- and (A-4) UTE-ΔR_2- ΔR_2^* combined MRAs of C6 tumor rats: the CNR and CNR difference from tumor region of UTE-ΔR_2-ΔR_2^* combined MRA were the highest.

Based on the results of the above analysis, CNRs were extracted from both normal and tumor regions of rats to evaluate the distinguishability of tumor and non-tumor from each MRA. As seen in **Figure 3.2.12**, the highest CNR value in tumor region was acquired from UTE-ΔR_2-ΔR_2^* combined MRA. Furthermore, the CNR difference of the normal and tumor regions was highest from UTE-ΔR_2-ΔR_2^* combined MRA for all four rats, as summarized in **Table 3.2.3**.

At 6 days after cell injection	C6 Rat 1			C6 Rat 2			C6 Rat 3			C6 Rat 4		
	CNR_n	CNR_t	CNR_d	CNR_n	CNR_t	CNR_d	CNR_n	CNR_t	CNR_d	CNR_n	CNR_t	CNR_d
UTE MRA	0.38	4.40	4.02	1.12	5.12	4.00	0.19	3.39	3.19	0.02	2.82	2.80
ΔR_2 MRA	1.21	8.40	7.19	0.64	7.90	7.26	1.05	7.87	6.82	1.03	7.41	6.38
ΔR_2^* MRA	1.02	5.04	4.03	0.87	1.85	0.98	0.94	3.76	2.81	0.51	5.31	4.79
Combined MRA	1.66	12.79	11.13	1.99	12.01	10.02	1.20	9.23	8.04	1.11	11.94	10.82

Table 3.2.3 Summary of CNRs of normal tissue (CNR_n), ipsilateral tumor (CNR_t), difference between normal tissue and tumor (CNR_d) for UTE-, ΔR_2-, ΔR_2^*-, and UTE-ΔR_2- ΔR_2^* combined MRAs for the inner region of tumor-bearing rats.

For comparison of the longitudinal results of CNRs in normal and tumor region, all MRAs with same object were obtained at three time points (6, 9, and 12 days) after the injection of the c6 tumor cell into the rat's brain as shown in **Figure 3.2.13**. Although CNRs was no change in normal region, the increasing trend of CNR in the tumor region of rat was observed from ΔR_2 and UTE-ΔR_2-ΔR_2^* combined MRAs as time progressed and the highest CNR difference also show in UTE-ΔR_2-ΔR_2^* combined MRA. On the other hand, the CNR of ΔR_2^* MRA in tumor region was consistently decreased, because the signal of tumor region of T_2^* before SPION injection was affected by growing complexity of tumor microvessels.

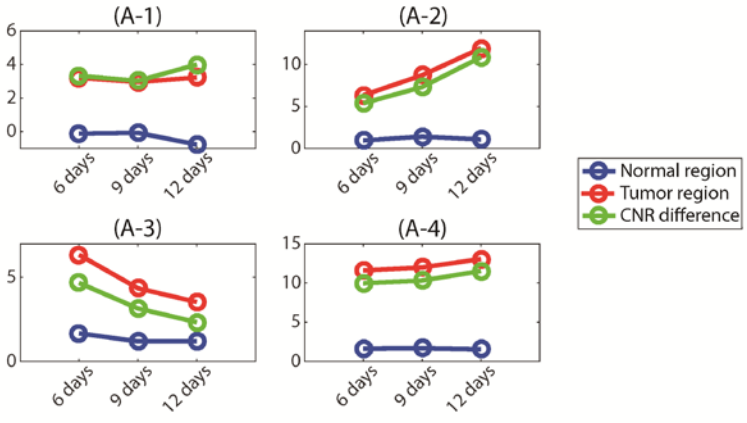

Figure 3.2.13 Changes of CNRs in normal and tumor regions of brain for the longitudinal study. (A-1) The CNRs of UTE-, (A-2) ΔR_2-, (A-3) ΔR_2^*-, and (A-4) UTE-ΔR_2-ΔR_2^* combined MRAs in C6 tumor rat. The CNR of the tumor region and CNR difference from UTE-ΔR_2-ΔR_2^* combined MRA were the highest and gradually increased as time goes.

As shown in **Figure 3.2.14A**, **B,** and **C**, MR anatomical images of tumor bearing rat of post UTE-, pre/post TSE, and pre/post FLASH acquisitions were shown by sequential time points after C6 tumor cell injection. Corresponding maps from ΔR_2, ΔR_2^*, combined (UTE+ $\Delta R_2 \times \Delta R_2^*$), and $\Delta R_2^*/\Delta R_2$ were shown (D-H). The enhanced contrast of UTE, ΔR_2, and ΔR_2^* images in the tumor region (white arrow) started to show up at 6 days after the cell injection.

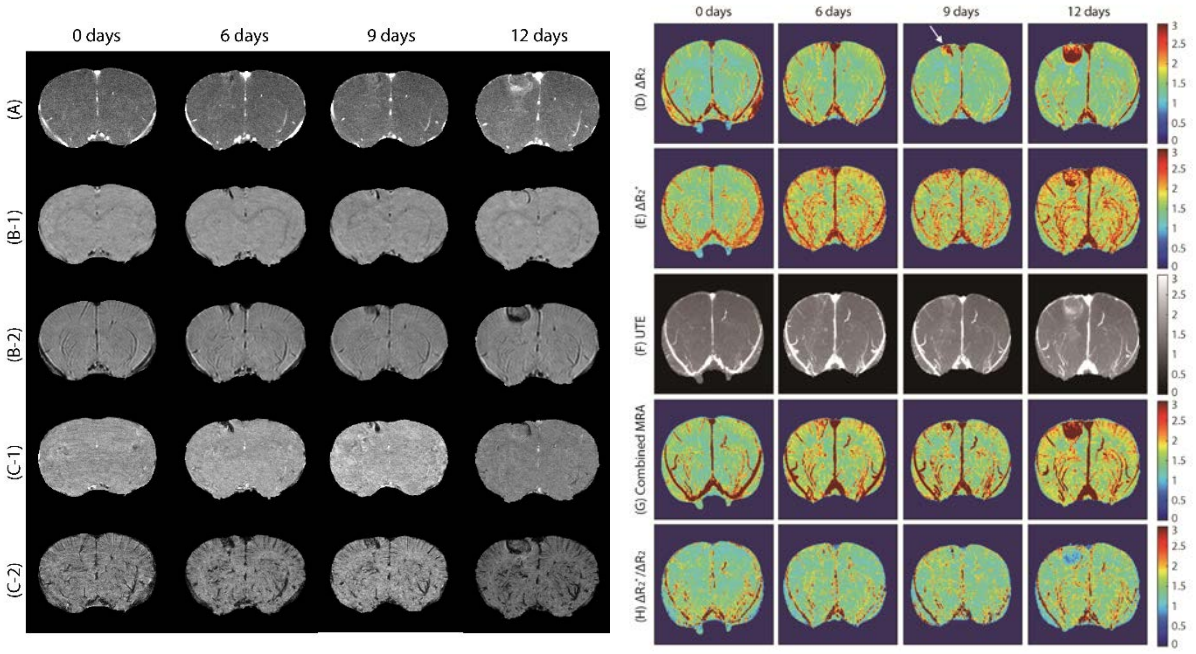

Figure 3.2.14 Longitudinal (0~12 days) anterior-to-posterior view of a C6 tumor bearing rat brain: (A) T_1-weighted UTE image after SPION injection. (B-1) and (B-2) T_2-weighted TSE images before and after SPION injection, respectively. (C-1) and (C-2) T_2^*-weighted FLASH images before and after SPION injection, respectively. (D) ΔR_2 map, (E) ΔR_2^* map, (F) UTE, (G) combined UTE + $\Delta R_2 \times \Delta R_2^*$ map and (H) conventional vessel size $\Delta R_2^*/\Delta R_2$ map as time progresses (1.56 mm thick slab sections). White arrow indicates the tumor region.

As time progresses, variations of vasculature in the left cortex region were increased. The contrast of tumor region was different according to each MRA. The signal reduction in tumor region of T_2 image after SPION injection was higher compared with those of UTE and T_2^* image after SPION injection. Although the relatively low enhanced contrast of UTE image in tumor region was appeared, peripheral tumor vessels were well-differentiated by enhancing with SPION due to only affected existence of contrast agent. And peripheral tumor vessel seems like relatively larger vessel than inner tumor vessel due to slightly high contrast in 12 days. The tumor region of ΔR_2^* map was difficult to distinguish tumor region. And the tumor region of UTE MRA was shown alike transverse relaxation based MRAs at 12

days after C6 tumor cell injection. Additionally, values of $\Delta R_2^*/\Delta R_2$ result in the our MRAs show lower than values of normal tissue as shown in **Figure 3.2.14H**. This may be from small vessel sprouts in tumor angiogenesis or it may result from extravasating SPION. The combined MRA at 12 days shows large enhancement, while $\Delta R_2^*/\Delta R_2$ shows the lowest values.

3.2.4 Discussion and conclusions

By using benefits of the dual contrast ability of SPION, the direct advantages of the UTE-ΔR_2-ΔR_2^* combined MRA were visualized and verified by quantification and comparison of vascular parameters from normal and tumor-bearing rat brains. The UTE MRA offered visualization of distinct vasculature on the brain surface regardless of air–tissue interface artifacts. The arterial region of the inner brain was also accurately represented with the high-dose feeding. The combination of deep brain regions from ΔR_2 and ΔR_2^* MRA increased the CNR of penetrating micro-vessels. As a result, the UTE-ΔR_2-ΔR_2^* combined MRA overall enhanced accuracy and sensitivity in the whole brain and obtained improved distinguishability of normal and tumor regions.

The HWHM and CNR of ΔR_2 and ΔR_2^* were similar at the 40 μm vessel diameter. The CNR of ΔR_2 is increasing as vessel diameter increases, while that of ΔR_2^* is staggering. The HWHM of ΔR_2^* values are rapidly increasing as vessel diameter increases. The CNR of both ΔR_2 and ΔR_2^* is decreasing as the resolution increases from the averaging effect of Gaussian like curve away from the cylinder-shape vessel surface. And the HWHM of ΔR_2^* was larger as the vessel diameter increased. These results show the vessel diameter overestimations from ΔR_2^* MRA. Regarding the limitation of feasible 3D spatial resolutions, it is important to study the aspects of the CNRs at various image resolutions. The CNR of ΔR_2^* was greater than that of ΔR_2 at various spatial resolutions, representing the high sensitivity of micro-vessel of ΔR_2^* MRA. Especially, the vessels of ΔR_2^* MRA are more detectable when the spatial resolution of the 3D MRA is slightly higher than vessel diameters.

The 3D imaging protocol with high resolution and manipulation of the contrast agent by concentration are keys to this method. The use of SPION with a prolonged half-life in vessels will help to manipulate the dose of SPION between pulse sequences for 3D MRA with high resolution. The UTE MRA was feasible for a low dose of SPION to maximize T_1 effect, while ΔR_2 MRA was needed a high dose of SPION to maximize T_2 effect. The dose of SPION of ΔR_2^* MRA will be appropriate due to excessive T_2^* effect with gradient-echo. The detected vessels in the cortex and higher signal than the threshold value from uneven tissue region by low TR were affected to give a similar count of vessel node and branch changes between UTE and ΔR_2 MRAs. For the increasing of detecting vessel accuracy, more scan time was needed to expand TR.

The limitations and feasible development of each MRA can be showed as follows. Although arteries and veins on the surface region from UTE MRA with T_1 contrast were defined well. But cortical arterioles and venules in deep brain were hardly detected because vessel size was lower than voxel resolution or low sensitivity by receive coil. This is main result of the insufficient volume coil for segmentation of micro-vessels. Resolution improvement of UTE3D with reduced acquisition time by using cryogenic and surface coils and sampling optimization may further increase sensitivity of smaller vessels in deep

brain [112, 113].

ΔR_2 MRA is widely applied to the visualization of micro-vessels in deep brain for the reason that it is less sensitive to vascular geometric distortions and air-tissue interface artifacts. So ΔR_2 MRA is free from vessel diameter overestimation [41]. However, the number of vessel branches for ΔR_2 MRA was significantly less than that for ΔR_2^* MRA. A additional cause for this observation may be blurring image artifacts from the TSE factor for acceleration 3D acquisitions by using spin echo [114-116]. Future acquisition optimization of ΔR_2 MRA will necessitate the diminished blurring artifact by using reduction of TSE factor, which may enhance sensitivity under a reasonable total acquisition scan time.

ΔR_2^* MRA provided outstanding sensitivity for micro-vessels, but is often evaded due to serious over-estimation of actual vessel diameter and air–tissue artifacts as presented by the line profile analysis and visualization of MRA. The overestimation problem of vessel diameter will depend on the decided threshold values in the process of vessel segmentation for all MRAs. The enhancement of CNR from the multiplication of ΔR_2 and ΔR_2^* MRAs should raise threshold values for vascular segmentation and ease vessel diameter overestimation of ΔR_2^* MRAs for comparatively large vessels as proved by FPM simulation and experiment. Also, susceptibility weighted imaging and quantitative susceptibility mapping techniques can be applied to obtain phase information and can also be implemented to substitute ΔR_2^* MRA. Processing of the UTE-ΔR_2-ΔR_2^* combined MRA is almost automatable, however, disconnection problems of interconnecting region between surface and inner vessels may be possible. Especially, small vessels from segmentation of each MRA may be a little dissimilar. The algorithms for suitable edge detection and patching may improve these discrepancies when merging various MRAs.

FPM simulation was implemented for the influence evaluation of the extra-vascular signal affected by comparatively large (>40 μm) vessels with limited spatial resolution. Nonetheless, it is attractive for comparing the suggested combined multi-contrasts and conventional parameters for micro-vasculature, such as the CBV or vessel size index ($\Delta R_2^*/\Delta R_2$) for capillaries (<10 μm). The extra-vascular signal influence of the ΔR_2^* MRA reduces as the vessel diameter decreases. And the $\Delta R_2 \times \Delta R_2^*$ may improve the sensitivity for small vessels, as seen in **Figure 3.2.14**, particularly for tumor angiogenesis. The significantly increased CNR of the tumor region from UTE-ΔR_2-ΔR_2^* combined MRA and the improved combined mapping may indicate this advantage as shown in **Figure 3.2.14**. Higher sensitivity in ΔR_2 and lowered $\Delta R_2^*/\Delta R_2$ verified the presence of micro-vessels in tumor regions at 12 days as shown in **Figure 3.2.14H**. However, SPION may have extravasated into the C6 tumor interstitium as previously reported [117, 118]. The unclear vasculature and slightly expanded contrast may also SPION extravasation effect in the tumor region. Additional work is required for wide-ranging confirmation between these situations.

In summary, *in vivo* animal experiments in this study demonstrated the representative characteristics of longitudinal and transverse relaxation-based MRAs with SPION as blood pool contrast agent and

UTE-ΔR_2-ΔR_2^* combined MRA. By merging the advantages of both positively and negatively enhanced contrast MRAs for many-sided description of vasculature using SPION, the proposed UTE-ΔR_2-ΔR_2^* combined MRA showed increased vascular sensitivity in the inner area and well-defined vessels on the brain surface area. The proposed UTE-ΔR_2-ΔR_2^* combined micro-MRA of whole brain may link the gap between conventional micro-vascular quantification and MRA, and can be used for consist monitoring of brain vasculature and follow-up studies to increase treatment effects.

Chapter 4. Evaluation of developed contrast agent for *in vivo* animal model

4.1 Lumazine Synthase Protein Nanoparticle-Gd(III)-DOTA Conjugate as a T_1 contrast agent for high-field MRI

4.1.1 Introduction

From a developing MRI contrast agent perspective, it is important to develop improved relaxivity of MRI contrast agents at higher magnetic fields. It is expected to drastically increase SNR and resolution in the high magnetic fields (> 7 T) [119]. However, it is generally observed that spin-lattice relaxation time (T_1) increases and converges for different tissues as the magnetic field strength increases. So, the contrast of T_1-weighted image at higher magnetic field (> 7 T) reduces when the same imaging parameters used at conventional 1.5 or 3 T [120, 121]. The observation of r_1 relaxivity decrease of MRI contrast agents at higher magnetic field necessitates development of efficient *in vivo* compatible positive with good relaxivity characteristics because MRI contrast agent is critical for the sensitivity and specificity of MRI examination [122-125].

Protein cage nanoparticles have been developed as nanoscale delivery vehicles for therapeutic reagents. And these particles extensively studied as supramolecular templates for the conjugation of small molecule contrast agents such as the chelated paramagnetic gadolinium ion. These macromolecule-based contrast agents are frequently used as a positive contrast agent for MRI and known as significantly higher r_1 relaxivity due to increased correlation time and decreased local motion [43, 126-132]. However, effectively useable *in vivo* MR contrast agents are a rarity because it is hard to maintain high r_1 relaxivity (> 10 $mM^{-1}s^{-1}$) with appropriate r_1/r_2 ratio (0.5 ~ 1) at high magnetic field [133-136]. With the increased application of MRI in higher magnetic fields, there is a need to maintain high r_1 relaxivity at high magnetic field.

In this study, lumazine synthase was used as nanoscale template for conjugates. And it was isolated from by hyperthermophile Aquifex aeolicus (AaLS). The developed nanoscale template evaluated its potential as an *in vivo* MR contrast agent at the magnetic field strength of 7 T. For our application, Gd(III)-chelating agent complexes were attached at position 108 with cysteine (R108C). It is known to be exposed on the exterior surface of AaLS.

The r_1 and r_2 relaxivities of Gd(III)-DOTA-AaLS-R108C were obtained at 1.43 T and 7 T with multiple phantoms. Tumor bearing mouse were prepared and Gd(III)-DOTA-AaLS-R108C was injected into

the mouse for *in vivo* experiments at 7T magnetic field. The signal behaviors and T_1 relaxation time were observed and compared with the Gd-DOTA (DOTAREM) and Gd(III)-DOTA-AaLS-R108C for both vascular and tumor regions.

4.1.2 Materials and Methods

Cell and animal models.

Six-week-old female BALB/c nude mice weighing 20–25 g (Harlan Laboratories) were used for the MRI experiments. Squamous cell carcinoma (SCC) -7 cells were cultured in RPMI1640 medium with 10% (v/v) fetal bovine serum and 1% (w/v) penicillin-streptomycin in 37 °C under conditions of 5% CO_2. To generate a tumor-bearing mouse model, 1×10^6 SCC-7 cells in phosphate-buffered saline (PBS) were injected subcutaneously into the right flank of nude mouse. When the tumor volume reached approximately 100 mm^3, the mice were used for the MRI experiments. All animal studies were performed in compliance with the guidelines of the local ethics committee for animal care and use, and were approved by the IACUC of Ulsan National Institute of Science and Technology.

Relaxivity Measurements

For measurements in vitro relaxivities of the Gd(III)-DOTA-AaLS, a Bruker Minispec MQ20 1.43 T and 7 T animal MRI scanner were used. The pulse sequences of standard inversion recovery (IR) and CPMG were used at magnetic field strength 1.4 T. The concentrations of Gd(III)-DOTA-AaLS were adjusted by dilution with phosphate-buffered saline (PBS) and six different Gd concentrations of Gd(III)-DOTA-AaLS-R108C were 0.074, 0.037, 0.0185, 0.00925, 0.004625, and 0 mM. The IR sequence parameter for the T_1 relaxation times of the Gd(III)-DOTA-AaLS was as follow: IR delay ranging = 0–20000 ms. The CPMG sequence parameters for T_2 relaxation times of the Gd(III)-DOTA-AaLS were as follow: echo spacing (TE) = 1 ms and recycling time (TR) = 1.5 s.

Also, the MR relaxivities of Gd(III)-DOTA-AaLS-R108C was characterized by using in vitro phantom imaging at magnetic field strength 7 T. the T_1 relaxation time was estimated using a TSE pulse sequence at variable repetition times. And the MESE pulse sequence was used for measurement of the T_2 relaxation time. The MR imaging parameters of TSE pulse sequence for the T_1 relaxation time were as follows: FA = 90°, TR = 20–5000 ms, TE = 7.6 ms. The MR imaging parameters of MESE sequence for T_2 relaxation time were as follows: FA = 90°, TR = 5000 ms, TE = 20–1000 ms. The longitudinal and transverse relaxivity were determined by measuring the T_1 relaxation times and T_2 relaxation times of six different Gd concentrations of Gd(III)-DOTA-AaLS-R108C (0.074, 0.037, 0.0185, 0.00925, 0.004625, and 0 mM). Both relaxivities r_1 and r_2 were calculated from the slope of the relaxation rate R_1 ($1/T_1$) and R_2 ($1/T_2$) as a function of concentration (mM) of contrast agent, respectively.

In vivo experiments scanner, animal, and contrast agent

All *in vivo* experiments were performed under approved IACUC of the Ulsan National Institute of Science and Technology. All total 6 male nude mice (20~25g) with tumor were used in this study. Four

mice were injected intravenously with 350 μl of Gd(III)-DOTA-AaLS-R108C (concentration: 17.143 mM) as a bolus into the tail vein. All tumor-bearing mice (the tumor volume, ~ 100 mm^3) were scanned on 7 T MRI animal scanner using a transceiver RF volume coil with diameter 40 mm for mouse body under anesthesia with 1.0-1.5% isoflurane. Radio frequency power and receiver gain was kept for each *in vivo* scan. And, two mice were used with 350 μl of DOTAREM (concentration: 17.857 mM) as a reference group.

To evaluate ability of vascular imaging and tumor targeting efficacy of Gd(III)-DOTA-AaLS-R108C, RAREVTR (RARE with variable repetition time TR) and 3D FLASH sequence were performed before and at six time points (1, 2, 3, 7, 12 and 30 hours) after the intravenous injection of the contrast agent at a dose of 0.3 mmol/kg. The T_1-map and high resolution 3D MRA were obtained, respectively. The MR imaging parameters of RAREVTR were set as follows: FA = 90°, TR = 8 values in the range of 280-5000 ms, TE = 6 ms, FOV = 30 × 30 mm^2, slice thickness = 1 mm, matrix size = 128 × 128. The MR imaging parameters of 3D FLASH were set as follows: FA = 20°, TR = 13 ms, TE = 2.1 ms, FOV = 30 × 30 × 30 mm^3, matrix size = 256 × 256 × 256. MRAs were reconstructed using MIP and T_1-maps were generated by a mono-exponential fitting method by using Matlab (R2014b, The Math Works Inc., Natick, MA, USA).

4.1.3 Results

Relaxivity measurements with phantoms

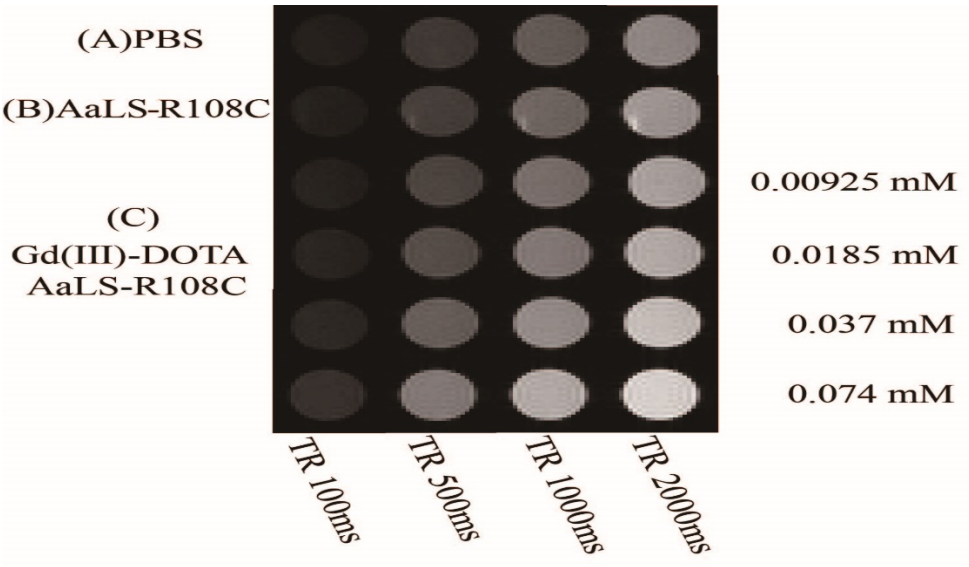

Figure 4.1.1: T_1-weighted *in vitro* phantom images. (A) PBS control, (B) AaLS-R108C only and (C) Gd(III)-DOTA-AaLS-R108C with increasing concentrations at 7 T. All images were obtained using a RAREVTR sequence at 4 TR values (100, 500, 1000, and 2000 ms).

For evaluation the ability of Gd(III)-DOTA-AaLS-R108C as an appropriate T_1 contrast agent of *in vivo* experiment at high magnetic field, T_1-weighted images were acquired by the different concentration phantoms on a magnetic field strength 7 T with a volume coil. The 4 TR values of RAREVTR pulse sequence were 100, 500, 1000, and 2000 ms. The T_1-weighted phantom images of PBS, AaLS-R108C only and Gd(III)-DOTA-AaLS-R108C were shown in **Figure 4.1.1**. The PBS control and AaLS-R108C only do not have significant signal difference as a function of TR because T_1 values does not change between them. On the other hand, Gd(III)-DOTA-AaLS-R108C shows brighter image at short TRs compared to those of that PBS control and AaLS-R108C-only due to decreased T_1 values.

As the Gd concentration is increased, the decreased T_1 values of Gd(III)-DOTA-AaLS-R108C contribute to contrast enhancement and brighter images were obtained at short TRs. To compare with conventional DOTAREM, the signals of RAREVTR at values of multiple TR were plotted together. The Gd concentrations were 0.004625, 0.00925, 0.0185, 0.037, and 0.074 mM. The saturation recovery signals of Gd(III)-DOTA-AaLS-R108C and DOTAREM were shown in **Figure 4.1.2**. Decreased T_1 values of Gd(III)-DOTA-AaLS-R108C were obvious at the same concentration and the r_1 relaxivity of Gd(III)-DOTA-AaLS-R108C was larger than that of conventional DOTAREM.

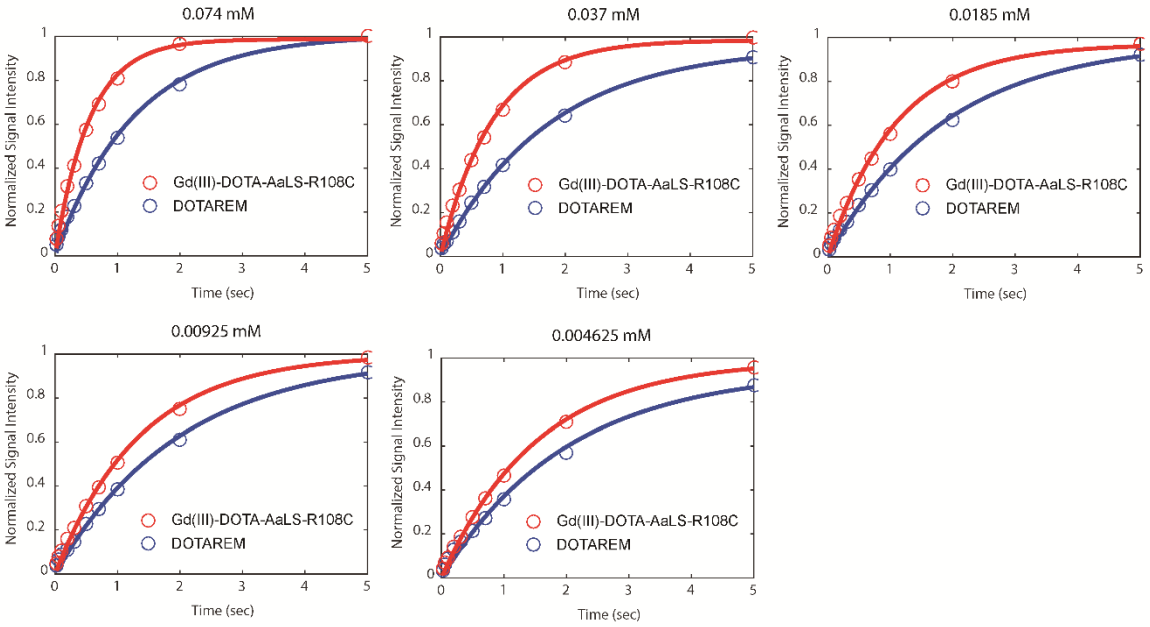

Figure 4.1.2: The comparison of relaxation time for Gd(III)-DOTA-AaLS-R108C and conventional DOTAREM. The saturation recovery signal with RAREVTR at multiple TR values were plotted together at identical Gd concentrations of Gd(III)-DOTA-AaLS-R108C and DOTAREM. Increased R_1 values were apparent for Gd(III)-DOTA-AaLS-R108C.

In **Figure 4.1.3A-1** and **C-1**, the slope of T_1 measurement became steeper on both magnetic field strength 1.43 T and 7 T as the concentrations of Gd(III) increased. This results showed that the net magnetization of Gd(III)-DOTA-AaLS-R108C recovers back rapidly. As concentrations of Gd(III) increased, T_2 relaxation times also decreased in **Figure 4.1.3A-2** and **C-2**. Gd(III)-DOTA-AaLS-R108C showed higher r_1 relaxivity. As shown in **Figure 4.1.3A-3**, The r_1 and r_2 relaxivites were 30.24 $mM^{-1}s^{-1}$ and 41.42 $mM^{-1}s^{-1}$ under 1.43 T (37 °C), respectively. As shown in **Figure. 4.1.3C-3**, the relaxivity of Gd(III)-DOTA-AaLS-R108C decreased under room temperature at 7 T. At 7 T, the r_1 and r_2 relaxivites of Gd(III)-DOTA-AaLS-R108C were 16.49 $mM^{-1}s^{-1}$ and 31.86 $mM^{-1}s^{-1}$. However, the measured r_1/r_2 values of Gd(III)-DOTA-AaLS-R108C were maintained acceptably by 0.73 and 0.52 at 1.43 T and 7 T, respectively. This results indicated that Gd(III)-DOTA-AaLS-R108C regards as the appropriate T_1 contrast agent at high magnetic field. The T_1 and T_2 relaxation time measurements of untreated AaLS-R108C at same conditions were shown in **Figure 4.1.3B-1** and **B-2** at 1.43 T. The r_1 and r_2 relaxivities of untreated AaLS-R108C were 0.37 $mM^{-1}s^{-1}$ and 1.29 $mM^{-1}s^{-1}$ at 1.43 T. Also, T_1 and T_2 relaxation time measurements were shown in **Figure 4.1.3D-1** and **D-2** at 7 T and r_1 and r_2 relaxivities of untreated AaLS-R108C were 1.02 $mM^{-1}s^{-1}$ and 3.14 $mM^{-1}s^{-1}$, respectively. The relaxivities of untreated AaLS-R108C were measured as reference as shown in **Figure 4.1.3B-3** and **D-3**.

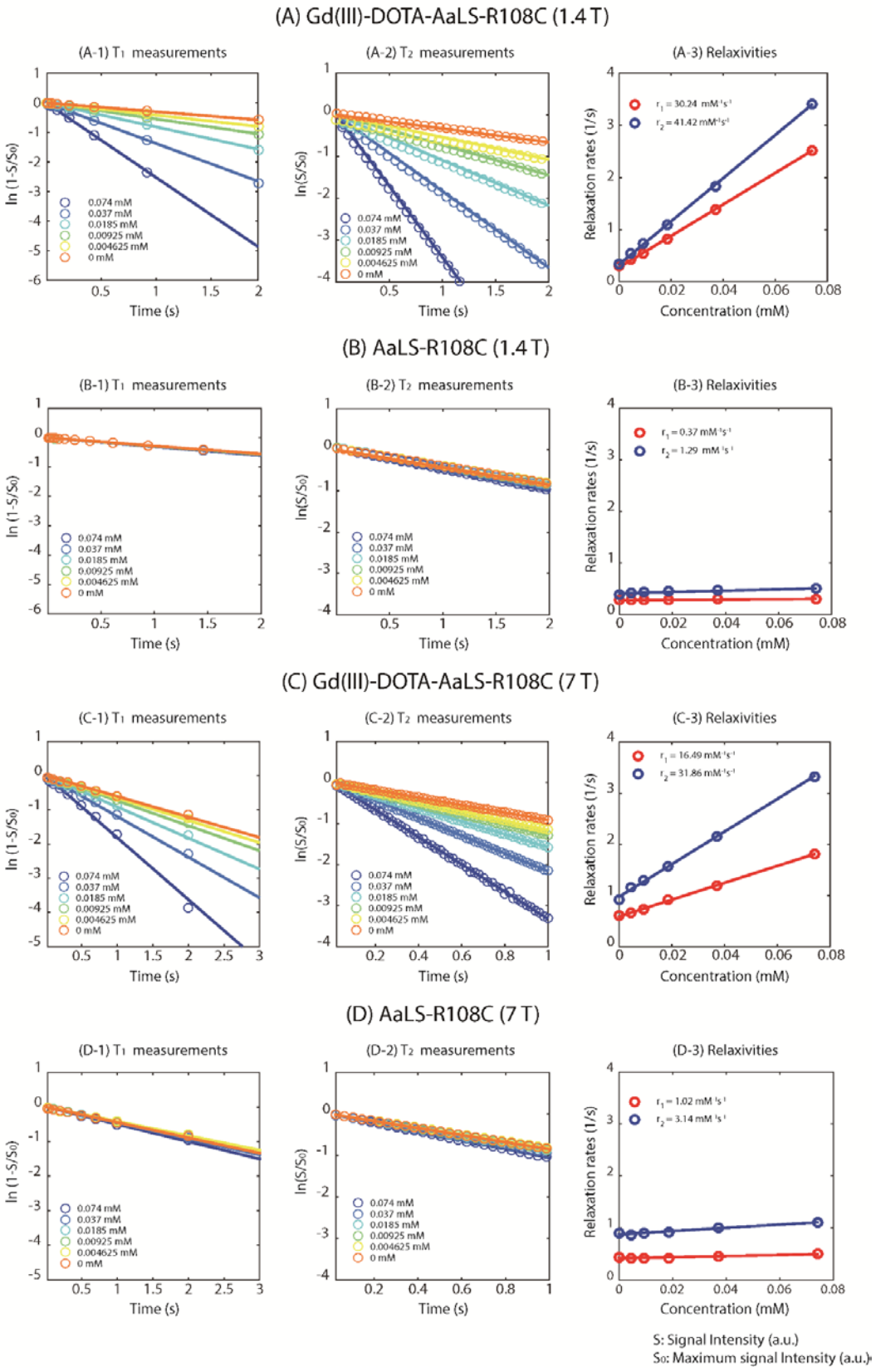

Figure 4.1.3: Measurements of T_1 and T_2 relaxation times of Gd(III)-DOTA-AaLS-R108C at (A)1.4 T and (C) 7 T. Measurements of T_1 and T_2 relaxation times of AaLS-R108C at (B)1.4 T and (D) 7 T.

In vivo characterizations

T_1 maps of tumor-bearing mice were obtained for evaluation of newly developed Gd(III)-DOTA-AaLS-R108C accumulation efficacy in the tumor region. To compare directly, the longitudinal experiments and analysis with same conditions were performed by using with Gd(III)-DOTA-AaLS-R108C and conventional DOTAREM. To obtain regionally averaged T_1 values, ROI analysis was performed. The T_1 values of the tumor region of mice in presence of Gd(III)-DOTA-AaLS-R108C was consistently decreased after the time point of ~7 h. As shown in **Figure 4.1.4A** and **4.1.4B**, T_1 maps before and 30 h after the injection of Gd(III)-DOTA-AaLS-R108C were showed. The T_1 fitting result was shown in **Figure 4.1.4C** at both time points, respectively. In both T_1 maps and corresponding raw T_1 fitting results, The T_1 values in the tumor region of mice were decreased at 30 h after the injection of Gd(III)-DOTA-AaLS-R108C.

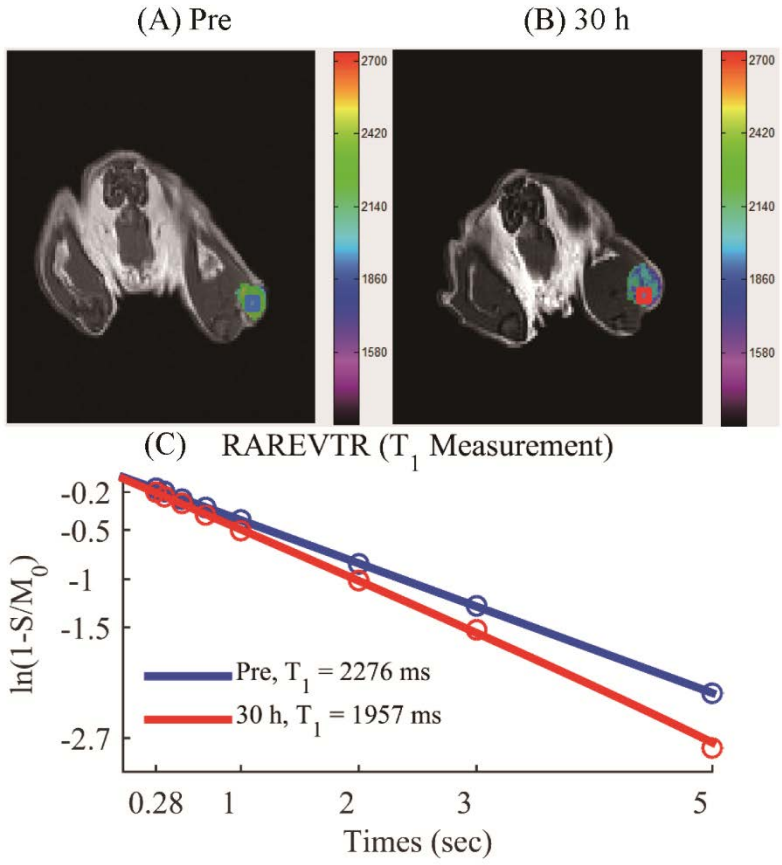

Figure 4.1.4: Representative T_1 map and fitting quality. (A) Representative T_1 map before injection of Gd(III)-DOTA-AaLS-R108C, (B) Representative T_1 map after 30 h Gd(III)-DOTA-AaLS-R108C injection and (C) T_1 fittings of ROI over the tumor prior to (blue square) and 30 h (red square) after injection of Gd(III)-DOTA-AaLS-R108C.

At sequential time points, MIP images of tumor bearing mice before and after the injection of Gd(III)-DOTA-AaLS-R108C were shown in the first column of **Figure 4.1.5A**. Directly after the injection of contrast agents, signal intensity of blood vessels were brightened because of drastically decreased T_1 values. As time goes on, positively enhanced contrast of blood vessel reduced. The positively enhanced contrast in the tumor region was observed 7h after the injection of contrast agent. Decreased T_1 values in tumor regions were verified through T_1 maps as shown in the second column of **Figure 4.1.5B**. In the third column of **Figure 4.1.5C**, the median-shift of the T_1 histogram for the whole 3D tumor volume was observed. shown. As shown in **Figure 4.1.5D**, **E** and **F**, same analysis was applied to results with conventional DOTAREM. Signal intensities of blood vessels were also increased immediately after the injection and the enhanced contrast was diminished as time progressed. The T_1 values in the tumor region was obvious to 2 h after the injection of DOTAREM, and then the T_1 values recover back to original values 7 h after DOTAREM injection.

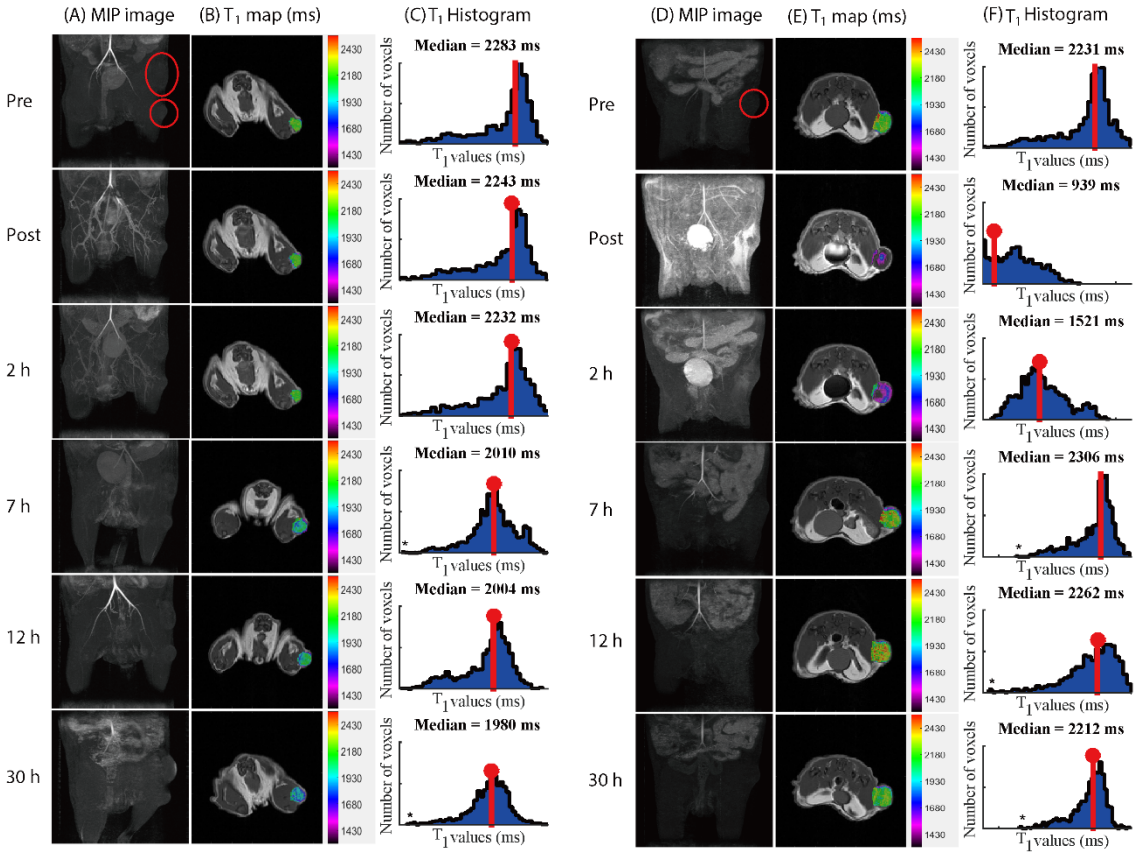

Figure 4.1.5: Representative (A) 3D MIP images, (B) T_1-maps, and (C) histogram of T_1 values at various time points after injection of Gd(III)-DOTA-AaLS-R108C. Representative (D) 3D MIP images, (E) T_1-maps, and (F) histogram of T_1 values at various time points after injection of conventional Gd-DOTA.

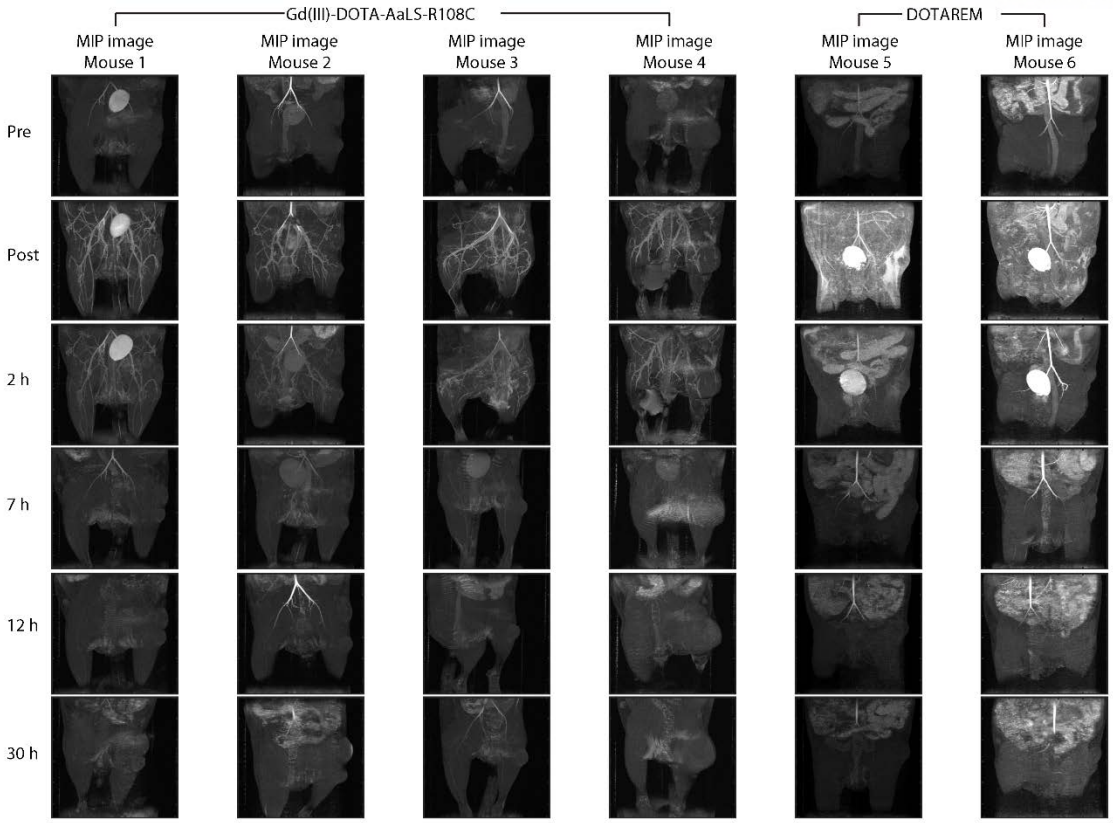

Figure 4.1.6: Longitudinal maximum intensity projection (MIP) images before and after injections of Gd(III)-DOTA-AaLS-R108C (n=4) and DOTAREM (n=2)

Longitudinal maximum intensity projection (MIP) images before and after the injections of Gd(III)-DOTA-AaLS-R108C (n = 4) and DOTAREM (n = 2) were shown in **Figure 4.1.6**. Bright femoral arterial regions before the injection in the Gd(III)-DOTA-AaLS-R108C look bright due to time of flight (TOF) effect. It is well known that TOF contrast is independent on the position of the mouse with respect to magnetic field direction. So this effect is independent of the injected contrast agent as shown with full MRA for six mice. However, it is clear that Gd(III)-DOTA-AaLS-R108C enhanced MRA show improved vessel-to-tissue contrast compared to corresponding DOTAREM enhanced MRA right after the injection as shown in **Figure 4.1.6** at 2 hours.

The results of ROI analysis were shown in **Figure 4.1.7A** and **B**. The signal enhancements in the arterial vessel region were measured after injections of Gd(III)-DOTA-AaLS-R108C and conventional DOTAREM. The variations of signal enhancement with both contrast agents in artery region were a similar trend. The maximized signal enhancements were observed from both contrast agents, immediately after injection of contrast agents. As time goes on, this signal enhancement decreased. The arterial signal enhancement from Gd(III)-DOTA-AaLS-R108C was slower than that from conventional DOTAREM. This result probably was caused by size and hydrophilic surface of Gd(III)-DOTA-AaLS-

R108C and it has prolonged intravascular residence time. After 7 h injection with DOTAREM and Gd(III)-DOTA-AaLS-R108C, both of arterial signal enhancements were significantly decreased, respectively.

As shown in **Figure 4.1.7C** and **D**, temporal variations of T_1 values with Gd(III)-DOTA-AaLS-R108C and DOTAREM in both tumor and muscle regions were plotted. For Gd(III)-DOTA-AaLS-R108C, the averaged T_1 value in the muscle on the other side thigh showed no meaningful variation at any time point. However, in tumor region, the averaged T_1 value slowly decreased up to 2 h after injection of Gd(III)-DOTA-AaLS-R108C and statistically decreased after 7 h post-injection ($p < 0.05$). For DOTAREM, the T_1 value in the tumor region was increased to the minimum value at point directly after the injection, and then rapidly rebounded and returned to its original level at 7 h. T_1 value in muscle region showed a similar trend to T_1 in tumor, with relatively reduced changes.

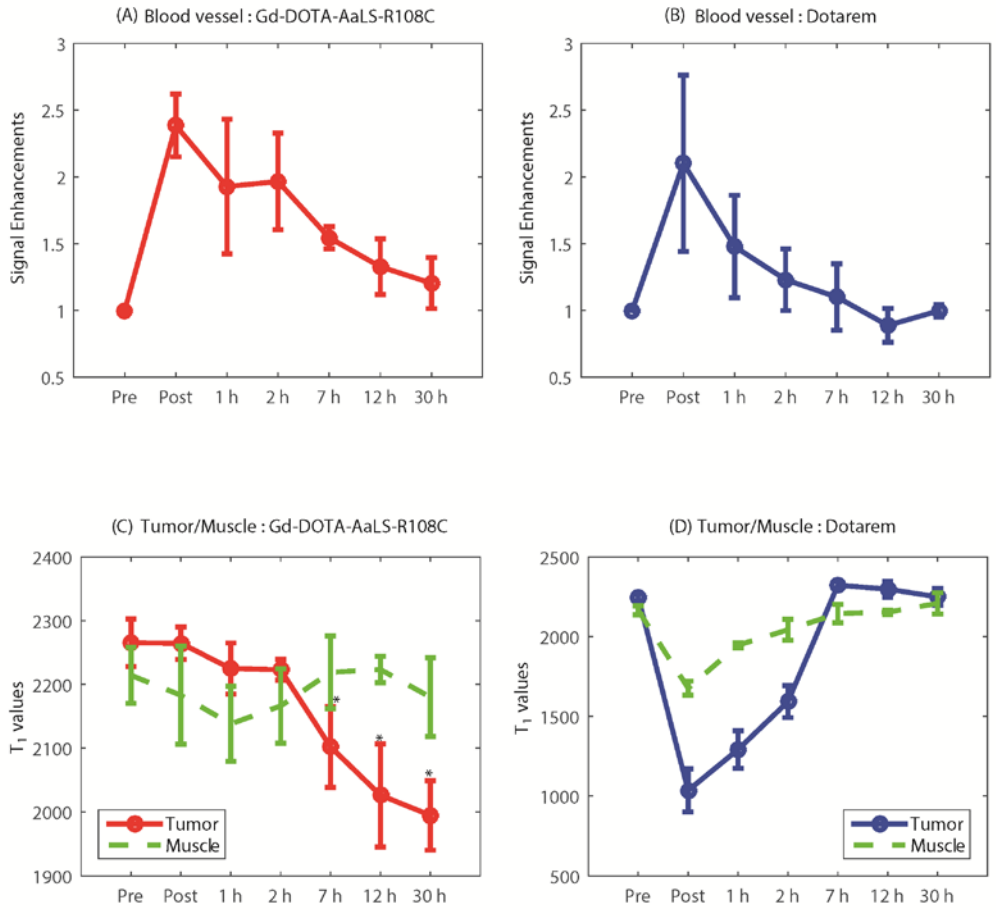

Figure 4.1.7: Temporal changes of signal enhancement and T_1 values in arterial region. Temporal signal enhancement after injection of (A) Gd(III)-DOTA-AaLS-R108C and (B) Gd-DOTA. Temporal variation of median T_1 values in tumor and muscle regions after the injection of (C) Gd(III)-DOTA-AaLS-R108C and (D) Gd-DOTA, respectively. (* represents the statistical significance with $p < 0.05$).

4.1.4 Discussion and conclusions

The developed Gd(III)-D OTA-AaLS-R108C has high T_1 relaxivity in high magnetic field because its large cage architecture is the slow tumbling rate. As the magnetic field is increased, the r_1/r_2 ratio tends to decrease significantly. This conventional results often represent a problem when macromolecular contrast agents were used at high field. In this study, the r_1/r_2 ratio of Gd(III)-DOTA-AaLS-R108C was measured 0.52 at 7T and this result is optimal as a T_1 contrast agent. It appears that the attachment of the Gd-chelating agent affects overall relaxivity, but the exact mechanism is unexplained at this point. Future simulation of relaxivity may shed more light on these experimental observations.

The MIP images of *in vivo* experiment after the injection of Gd(III)-DOTA-AaLS-R108C show well-defined vasculature, as shown in **Figure 4.1.6**. The MIP images with Gd-DOTA was not appear diminished vasculature because Gd-DOTA exhibited fast leakage in a rodent model for vasculature imaging, The MIP images with Gd(III)-DOTA-AaLS-R108C as intravascular contrast agent was shown proper robust MR angiography at 7 T. The temporal tendency of signal enhancement in the region of arterial vessel shows that vasculature signal enhancement is achieved within 2 h of intravenous injection of Gd(III)-DOTA-AaLS-R108C.

As the longitudinal relaxation rate (R_1) in tumor is generally known to be proportional to Gd(III) concentration, the absolute T_1 ($1/R_1$) map of tumor and muscle regions on the other hind leg enables the monitoring of temporal variations in Gd(III) accumulation of both regions, with minimized animal repositioning and slice mismatch errors occurring in longitudinal follow up studies. In other words, decreasing absolute T_1 values in tissue should reflect increasing Gd(III) concentration of the corresponding region. The T_1 value of the tumor decreased after the injected Gd(III)-DOTA-AaLS-R108C gradually migrated to the tumor region. A statistically significant decline in T_1 value was observed 7 h after Gd(III)-DOTA-AaLS-R108C injection, which coincides with a significant drop in signal enhancement in the arterial region. Compared to the short retention time (< 2 h) of DOTAREM, due to its relatively small size and low molecular weight, Gd(III)-DOTA-AaLS-R108C showed a prolonged retention time in tumor. A consistent T_1 value in the other hind leg muscle away from the tumor supported the tumor-specific migration of Gd(III)-DOTA-AaLS-R108C, presumably due to the enhanced permeability and retention effects of the tumor [137, 138]. These observations could be considered as the results of the abnormal characteristics of tumor tissue. In general, it is known that tumor tissues exhibit leaky vasculature and ineffective lymphatic drainage due to rapid and defective angiogenesis [139]. Hence, the tumor vasculature easily permits adequate sized macromolecules in plasma to escape from the tumor vessels and accumulate in tumor tissue for a specific time. Meanwhile, although the long retention time of Gd(III)-DOTA-AaLS-R108C in tumor could be a strength in applications relating to anti-tumor therapy or drug delivery, it may raise toxicity concerns due to the release of free Gd(III) from prolonged

retention, and further *in vivo* toxicity study should be followed.

This study demonstrates that newly developed Gd(III)-DOTA-AaLS-R108C could be successfully applied as a positive T_1 MR contrast agent at high field, and utilized as a high-resolution vascular imaging agent, active within 2 h of injection. Its prolonged retention time in tumors may be a key advantage for a potential theranostic nanoplatform, as well as for future scientific investigations of optimized MRI T_1 contrast agent at higher magnetic field.

Chapter 5. Concluding remarks

In this thesis, I dealt with two subjects. The one is to find inherent properties and applications of dual contrast for MRI imaging. Dual contrast enhanced imaging in MRI is presented as a way of compensating potential troubles when contrast enhanced image by using contrast agent was acquired from the same object. This dual contrast was applied to verify feasibility of the visualization and quantification of rodent micro-vasculatures in the *in vivo* study. The other is evaluating newly developed contrast agent through *in vitro* and *in viv*o experiments. The newly developed contrast agent used in this study was successfully demonstrated as a positive T_1 MR contrast agent at high magnetic field, and utilized to accumulate in tumor region.

In Chapter 2, the characteristic of SPION was introduced for explaining use in MRI application. Then, the essential concepts of two relaxation contrasts and methods of obtaining these contrasts for 3D MR images were presented to comprehend results of this research. And the basic of MRI imaging was explained by using the equation and figure. Especially, the principles of the FLASH, TSE, and radial UTE techniques for 3D imaging was described because these three pulse sequences were used in this research. Finally, the MR angiography (MRA) in MRI is described to understand features of contrast enhanced vasculature images by various MRA methods.

In Chapter 3, single sized controlled contrast agent was used for obtaining dual contrast in MRI. This contrast agent was widely used in pre-clinical research and called by SPION or MION. The dual contrast was obtained by adjusting SPION concentration and MR imaging parameters for *in vivo* animal experiment. Although the dual contrast enhanced images may provide depiction inconsistency in some anatomical regions, but diverse information from this inconsistency was helped to improve acquired image quality and comprehend anatomy and physiology of the object.

Based on observation of dual contrast enhanced images, the dual contrast was utilized to visualize rodent brain's vasculature with high resolution in the second study. The positively and negatively enhanced contrast brain MRAs showed those strengths and weaknesses. To complement shortcomings of each MRA, combined MRA was generated and robust *in vivo* whole-brain MRA was visualized by minimizing various artifacts.

In Chapter 4, I characterized and evaluated newly developed contrast agent with high r_1 relaxivity at 7 T magnetic field. The ability of the enhanced contrast of developed contrast agents at high magnetic field was confirmed by *in vitro* phantom and *in vivo* MRA experiments. From *in vitro* phantom experiment, the feasibility of use as T_1-contrast agent in MRI was proved by comparison with reference and developed contrast agent without Gd ion. For *in vivo* tumor bearing mouse experiments, the results of 3D MRA and T_1 map according to sequential time points demonstrated the usefulness of developed contrast agent for vascular imaging within 2 hours after intravenous injection and targeting tumor region

in the SCC-7 flank tumor model by observation of a significant reduction in T_1 values in the 7 hours after intravenous injection.

References

1 BENDERBOUS, S., COROT, C., JACOBS, P. & BONNEMAIN, B. 1996. Superparamagnetic agents: physicochemical characteristics and preclinical imaging evaluation. *Academic radiology,* 3**,** S292-S294.

2 VARALLYAY, P., NESBIT, G., MULDOON, L. L., NIXON, R. R., DELASHAW, J., COHEN, J. I., PETRILLO, A., RINK, D. & NEUWELT, E. A. 2002. Comparison of two superparamagnetic viral-sized iron oxide particles ferumoxides and ferumoxtran-10 with a gadolinium chelate in imaging intracranial tumors. *American Journal of Neuroradiology,* 23**,** 510-519.

3 CORNELL, R. M. & SCHWERTMANN, U. 2003. *The iron oxides: structure, properties, reactions, occurrences and uses,* John Wiley & Sons.

4 STEPHEN, Z. R., KIEVIT, F. M. & ZHANG, M. 2011. Magnetite nanoparticles for medical MR imaging. *Materials Today,* 14**,** 330-338.

5 HODGES, D. C. Clinical MR Imaging: A Practical Approach.

6 STABI, K. L. & BENDZ, L. M. 2011. Ferumoxytol use as an intravenous contrast agent for magnetic resonance angiography. *Annals of Pharmacotherapy,* 45**,** 1571-1575.

7 IV, M., TELISCHAK, N., FENG, D., HOLDSWORTH, S. J., YEOM, K. W. & DALDRUP-LINK, H. E. 2015. Clinical applications of iron oxide nanoparticles for magnetic resonance imaging of brain tumors. *Nanomedicine,* 10**,** 993-1018.

8 TROPRES, I., GRIMAULT, S., VAETH, A., GRILLON, E., JULIEN, C., PAYEN, J. F., LAMALLE, L. & DECORPS, M. 2001. Vessel size imaging. *Magnetic resonance in medicine,* 45**,** 397-408.

9 VARALLYAY, C. G., MULDOON, L. L., GAHRAMANOV, S., WU, Y. J., GOODMAN, J. A., LI, X., PIKE, M. M. & NEUWELT, E. A. 2009. Dynamic MRI using iron oxide nanoparticles to assess early vascular effects of antiangiogenic versus corticosteroid treatment in a glioma model. *Journal of Cerebral Blood Flow & Metabolism,* 29**,** 853-860.

10 BROWN, R. W., CHENG, Y.-C. N., HAACKE, E. M., THOMPSON, M. R. & VENKATESAN, R. 2014. *Magnetic resonance imaging: physical principles and sequence design,* John Wiley & Sons.

11 LEVITT, M. H. 2001. *Spin dynamics: basics of nuclear magnetic resonance,* John Wiley & Sons.

12 RIDGWAY, J. P. 2010. Cardiovascular magnetic resonance physics for clinicians: part I. *Journal of cardiovascular magnetic resonance,* 12**,** 1.

13 TOFTS, P. 2005. *Quantitative MRI of the brain: measuring changes caused by disease,* John Wiley & Sons.

14 BOULBY, P. A. & RUGG-GUNN, F. 2003. T2: the transverse relaxation time. *Quantitative MRI of the brain. Wiley, Chichester***,** 143-202.

15 GRANDINETTI, P. J. 2011. *Nuclear Magnetic Resonance for the People*.

16 BAIN, A. D. 1990. The choice of parameters in an NMR experiment. Application to the inversion-recovery T1 method. *Journal of Magnetic Resonance (1969),* 89**,** 153-160.

17 PLEIN, S., GREENWOOD, J. P. & RIDGWAY, J. P. 2011. *Cardiovascular MR manual,* Springer.

18 SALONER, D. 1995. The AAPM/RSNA physics tutorial for residents. An introduction to MR angiography. *Radiographics,* 15**,** 453-465.

19 HAASE, A., FRAHM, J., MATTHAEI, D., HANICKE, W. & MERBOLDT, K.-D. 1986. FLASH imaging. Rapid NMR imaging using low flip-angle pulses. *Journal of Magnetic Resonance (1969),* 67**,** 258-266.

20 HENNIG, J., NAUERTH, A. & FRIEDBURG, H. 1986. RARE imaging: a fast imaging method for clinical MR. *Magnetic resonance in medicine,* 3**,** 823-833.

21 RAHMER, J., B RNERT, P., GROEN, J. & BOS, C. 2006. Three-dimensional radial ultrashort

echo-time imaging with T2 adapted sampling. *Magnetic resonance in medicine,* 55**,** 1075-1082.
22 GLOVER, G. H., PAULY, J. M. & BRADSHAW, K. M. 1992. Boron-11 imaging with a three-dimensional reconstruction method. *Journal of Magnetic Resonance Imaging,* 2**,** 47-52.
23 ROBSON, M. D., GATEHOUSE, P. D., BYDDER, M. & BYDDER, G. M. 2003. Magnetic resonance: an introduction to ultrashort TE (UTE) imaging. *Journal of computer assisted tomography,* 27**,** 825-846.
24 HOLMES, J. E. & BYDDER, G. M. 2005. MR imaging with ultrashort TE (UTE) pulse sequences: basic principles. *Radiography,* 11**,** 163-174.
25 BERGIN, C., GLOVER, G. & PAULY, J. 1991. Lung parenchyma: magnetic susceptibility in MR imaging. *Radiology,* 180**,** 845-848.
26 HERRMANN, K.-H., KR MER, M. & REICHENBACH, J. R. 2016. Time Efficient 3D Radial UTE Sampling with Fully Automatic Delay Compensation on a Clinical 3T MR Scanner. *PloS one,* 11**,** e0150371.
27 MIRAUX, S., SERRES, S., THIAUDIERE, E., CANIONI, P., MERLE, M. & FRANCONI, J.-M. 2004. Gadolinium-enhanced small-animal TOF magnetic resonance angiography. *Magnetic Resonance Materials in Physics, Biology and Medicine,* 17**,** 348-352.
28 ALLKEMPER, T., BREMER, C., MATUSZEWSKI, L., EBERT, W. & REIMER, P. 2002. Contrast-enhanced blood-pool MR angiography with optimized iron oxides: effect of size and dose on vascular contrast enhancement in rabbits 1. *Radiology,* 223**,** 432-438.
29 PRICE, R. R., CREASY, J. L., LORENZ, C. H. & PARTAIN, L. C. 1992. Magnetic resonance angiography techniques. *Investigative radiology,* 27**,** S27-S32.
30 KNOPP, M., VON TENGG-KOBLIGK, H., FLOEMER, F. & SCHOENBERG, S. 1999. Contrast agents for MRA: future directions. *Journal of Magnetic Resonance Imaging,* 10**,** 314-316.
31 PANNETIER, N., LEMASSON, B., CHRISTEN, T., TACHROUNT, M., TROPR S, I., FARION, R., SEGEBARTH, C., R MY, C. & BARBIER, E. L. 2012. Vessel size index measurements in a rat model of glioma: comparison of the dynamic (Gd) and steady-state (iron-oxide) susceptibility contrast MRI approaches. *NMR in Biomedicine,* 25**,** 218-226.
32 LEMASSON, B., VALABLE, S., FARION, R., KRAINIK, A., R MY, C. & BARBIER, E. L. 2013. In vivo imaging of vessel diameter, size, and density: a comparative study between MRI and histology. *Magnetic Resonance in Medicine,* 69**,** 18-26.
33 CAI, K., SHORE, A., SINGH, A., HARIS, M., HIRAKI, T., WAGHRAY, P., REDDY, D., GREENBERG, J. H. & REDDY, R. 2012. Blood oxygen level dependent angiography (BOLDangio) and its potential applications in cancer research. *NMR in Biomedicine,* 25**,** 1125-1132.
34 PARK, S. H., MASAMOTO, K., HENDRICH, K., KANNO, I. & KIM, S. G. 2008. Imaging brain vasculature with BOLD microscopy: MR detection limits determined by in vivo two-photon microscopy. *Magnetic Resonance in Medicine,* 59**,** 855-865.
35 PARKES, L. M., SCHWARZBACH, J. V., BOUTS, A. A., PULLENS, P., KERSKENS, C. M. & NORRIS, D. G. 2005. Quantifying the spatial resolution of the gradient echo and spin echo BOLD response at 3 Tesla. *Magnetic resonance in medicine,* 54**,** 1465-1472.
36 HUANG, C.-H., CHEN, C.-C. V., SIOW, T.-Y., HSU, S.-H. S., HSU, Y.-H., JAW, F.-S. & CHANG, C. 2013. High-Resolution Structural and Functional Assessments of Cerebral Microvasculature Using 3D Gas ΔR2*-mMRA. *PloS one,* 8**,** e78186.
37 COROT, C., ROBERT, P., ID E, J.-M. & PORT, M. 2006. Recent advances in iron oxide nanocrystal technology for medical imaging. *Advanced drug delivery reviews,* 58**,** 1471-1504.
38 BREMERICH, J., BILECEN, D. & REIMER, P. 2007. MR angiography with blood pool contrast agents. *European radiology,* 17**,** 3017-3024.
39 CLOFT, H. J., MURPHY, K. J., PRINCE, M. R. & BRUNBERG, J. A. 1996. 3D gadolinium-enhanced MR angiography of the carotid arteries. *Magnetic resonance imaging,* 14**,** 593-600.
40 WU, E. X., TANG, H. & JENSEN, J. H. 2004. Applications of ultrasmall superparamagnetic iron oxide contrast agents in the MR study of animal models. *NMR in Biomedicine,* 17**,** 478-483.

41 LIN, C.-Y., LIN, M.-H., CHEUNG, W.-M., LIN, T.-N., CHEN, J.-H. & CHANG, C. 2009. In vivo cerebromicrovasculatural visualization using 3D ΔR2-based microscopy of magnetic resonance angiography (3D ΔR2-mMRA). *Neuroimage,* 45**,** 824-831.

42 YAN, G.-P., ROBINSON, L. & HOGG, P. 2007. Magnetic resonance imaging contrast agents: overview and perspectives. *Radiography,* 13**,** e5-e19.

43 CARAVAN, P., ELLISON, J. J., MCMURRY, T. J. & LAUFFER, R. B. 1999. Gadolinium (III) chelates as MRI contrast agents: structure, dynamics, and applications. *Chemical reviews,* 99**,** 2293-2352.

44 TROUGHTON, J. S., GREENFIELD, M. T., GREENWOOD, J. M., DUMAS, S., WIETHOFF, A. J., WANG, J., SPILLER, M., MCMURRY, T. J. & CARAVAN, P. 2004. Synthesis and evaluation of a high relaxivity manganese (II)-based MRI contrast agent. *Inorganic chemistry,* 43**,** 6313-6323.

45 NA, H. B., LEE, J. H., AN, K., PARK, Y. I., PARK, M., LEE, I. S., NAM, D. H., KIM, S. T., KIM, S. H. & KIM, S. W. 2007. Development of a T1 contrast agent for magnetic resonance imaging using MnO nanoparticles. *Angewandte Chemie,* 119**,** 5493-5497.

46 LAWACZECK, R., MENZEL, M. & PIETSCH, H. 2004. Superparamagnetic iron oxide particles: contrast media for magnetic resonance imaging. *Applied organometallic chemistry,* 18**,** 506-513.

47 LAURENT, S., FORGE, D., PORT, M., ROCH, A., ROBIC, C., VANDER ELST, L. & MULLER, R. N. 2008. Magnetic iron oxide nanoparticles: synthesis, stabilization, vectorization, physicochemical characterizations, and biological applications. *Chemical reviews,* 108**,** 2064-2110.

48 MAYO-SMITH, W. W., SAINI, S., SLATER, G., KAUFMAN, J., SHARMA, P. & HAHN, P. F. 1996. MR contrast material for vascular enhancement: value of superparamagnetic iron oxide. *AJR. American journal of roentgenology,* 166**,** 73-77.

49 CHAMBON, C., CLEMENT, O., LE BLANCHE, A., SCHOUMAN-CLAEYS, E. & FRIJA, G. 1993. Superparamagnetic iron oxides as positive MR contrast agents: in vitro and in vivo evidence. *Magnetic resonance imaging,* 11**,** 509-519.

50 KIM, B. H., LEE, N., KIM, H., AN, K., PARK, Y. I., CHOI, Y., SHIN, K., LEE, Y., KWON, S. G. & NA, H. B. 2011. Large-scale synthesis of uniform and extremely small-sized iron oxide nanoparticles for high-resolution T1 magnetic resonance imaging contrast agents. *Journal of the American Chemical Society,* 133**,** 12624-12631.

51 WESTENBERG, J. J., VAN DER GEEST, R. J., WASSER, M. N., VAN DER LINDEN, E. L., VAN WALSUM, T., VAN ASSEN, H. C., DE ROOS, A., VANDERSCHOOT, J. & REIBER, J. H. 2000. Vessel diameter measurements in gadolinium contrast-enhanced three-dimensional MRA of peripheral arteries. *Magnetic resonance imaging,* 18**,** 13-22.

52 BRUBAKER, L. M., BULLITT, E., YIN, C., VAN DYKE, T. & LIN, W. 2005. Magnetic resonance angiography visualization of abnormal tumor vasculature in genetically engineered mice. *Cancer research,* 65**,** 8218-8223.

53 MIYATI, T., BANNO, T., MASE, M., KASAI, H., SHUNDO, H., IMAZAWA, M. & OHBA, S. 1997. Dual dynamic contrast-enhanced MR imaging. *Journal of Magnetic Resonance Imaging,* 7**,** 230-235.

54 WARD, J., GUTHRIE, J. A., SCOTT, D. J., ATCHLEY, J., WILSON, D., DAVIES, M. H., WYATT, J. I. & ROBINSON, P. J. 2000. Hepatocellular carcinoma in the cirrhotic liver: double-contrast MR imaging for diagnosis 1. *Radiology,* 216**,** 154-162.

55 CHOI, J.-S., LEE, J.-H., SHIN, T.-H., SONG, H.-T., KIM, E. Y. & CHEON, J. 2010. Self-confirming "AND" logic nanoparticles for fault-free MRI. *Journal of the American Chemical Society,* 132**,** 11015-11017.

56 WU, S., ZHANG, L., ZHONG, J. & ZHANG, Z. 2010. Dual contrast magnetic resonance imaging tracking of iron-labeled cells in vivo. *Cytotherapy,* 12**,** 859-869.

57 ZHOU, Z., HUANG, D., BAO, J., CHEN, Q., LIU, G., CHEN, Z., CHEN, X. & GAO, J. 2012. A Synergistically Enhanced T1–T2 Dual-Modal Contrast Agent. *Advanced Materials,* 24**,** 6223-6228.

58 BAE, K. H., KIM, Y. B., LEE, Y., HWANG, J., PARK, H. & PARK, T. G. 2010. Bioinspired synthesis and characterization of gadolinium-labeled magnetite nanoparticles for dual contrast T1-and T2-weighted magnetic resonance imaging. *Bioconjugate chemistry,* 21**,** 505-512.

59 YANG, H., ZHUANG, Y., SUN, Y., DAI, A., SHI, X., WU, D., LI, F., HU, H. & YANG, S. 2011. Targeted dual-contrast T1-and T2-weighted magnetic resonance imaging of tumors using multifunctional gadolinium-labeled superparamagnetic iron oxide nanoparticles. *Biomaterials,* 32**,** 4584-4593.

60 KIM, Y., TEJIMA, E., HUANG, S., ATOCHIN, D., DAI, G., LO, E., HUANG, P., BOGDANOV, A. & ROSEN, B. 2008. In vivo quantification of transvascular water exchange during the acute phase of permanent stroke. *Magnetic resonance in medicine,* 60**,** 813-821.

61 BEAUMONT, M., LEMASSON, B., FARION, R., SEGEBARTH, C., R MY, C. & BARBIER, E. L. 2009. Characterization of tumor angiogenesis in rat brain using iron-based vessel size index MRI in combination with gadolinium-based dynamic contrast-enhanced MRI. *Journal of Cerebral Blood Flow & Metabolism,* 29**,** 1714-1726.

62 HUANG, S., KIM, J. K., ATOCHIN, D. N., FARRAR, C. T., HUANG, P. L., SUH, J. Y., KWON, S. J., SHIM, W. H., CHO, H. & CHO, G. 2013. Cerebral blood volume affects blood–brain barrier integrity in an acute transient stroke model. *Journal of Cerebral Blood Flow & Metabolism,* 33**,** 898-905.

63 DONAHUE, K. M., WEISSKOFF, R. M., CHESLER, D. A., KWONG, K. K., BOGDANOV, A. A., MANDEVILLE, J. B. & ROSEN, B. R. 1996. Improving MR quantification of regional blood volume with intravascular T1 contrast agents: accuracy, precision, and water exchange. *Magnetic resonance in medicine,* 36**,** 858-867.

64 BOGDANOV JR, A., WEISSLEDER, R., FRANK, H., BOGDANOVA, A., NOSSIF, N., SCHAFFER, B., TSAI, E., PAPISOV, M. & BRADY, T. 1993. A new macromolecule as a contrast agent for MR angiography: preparation, properties, and animal studies. *Radiology,* 187**,** 701-706.

65 MEDAROVA, Z., CASTILLO, G., DAI, G., BOLOTIN, E., BOGDANOV, A. & MOORE, A. 2007. Noninvasive magnetic resonance imaging of microvascular changes in type 1 diabetes. *Diabetes,* 56**,** 2677-2682.

66 BOGDANOV JR, A. A., MAZZANTI, M. L., CASTILLO, G. & BOLOTIN, E. 2012. Protected graft copolymer (PGC) in imaging and therapy: a platform for the delivery of covalently and non-covalently bound drugs.

67 LOOK, D. C. & LOCKER, D. R. 1970. Time saving in measurement of NMR and EPR relaxation times. *Review of Scientific Instruments,* 41**,** 250-251.

68 RUEHM, S. G., COROT, C., VOGT, P., KOLB, S. & DEBATIN, J. F. 2001. Magnetic resonance imaging of atherosclerotic plaque with ultrasmall superparamagnetic particles of iron oxide in hyperlipidemic rabbits. *Circulation,* 103**,** 415-422.

69 GIRARD, O., DU, J., AGEMY, L., SUGAHARA, K., KOTAMRAJU, V., RUOSLAHTI, E., BYDDER, G. & MATTREY, R. 2011. Optimization of iron oxide nanoparticle detection using ultrashort echo time pulse sequences: Comparison of T1, T2*, and synergistic T1− T2* contrast mechanisms. *Magnetic Resonance in Medicine,* 65**,** 1649-1660.

70 LEE, H. & BLAUFOX, M. 1985. Blood volume in the rat. *Journal of Nuclear Medicine,* 26**,** 72-76.

71 KEYS, R. G. 1981. Cubic convolution interpolation for digital image processing. *Acoustics, Speech and Signal Processing, IEEE Transactions on,* 29**,** 1153-1160.

72 MAES, F., COLLIGNON, A., VANDERMEULEN, D., MARCHAL, G. & SUETENS, P. 1997. Multimodality image registration by maximization of mutual information. *Medical Imaging, IEEE Transactions on,* 16**,** 187-198.

73 OTSU, N. 1975. A threshold selection method from gray-level histograms. *Automatica,* 11**,** 23-27.

74 SAITO, T. & TORIWAKI, J.-I. 1994. New algorithms for Euclidean distance transformation of an n-dimensional digitized picture with applications. *Pattern recognition,* 27**,** 1551-1565.

75 HILDEBRAND, T. & R EGSEGGER, P. 1997. A new method for the model-independent

assessment of thickness in three-dimensional images. *Journal of microscopy,* 185**,** 67-75.

76 BABUCCU, O., TEKEREKOGLU, B., OZDEMIR, H., BESIR, H. & GUNDOGDU, S. 2011. Comparison of the five different methods in arterial diameter measurement. *Surgical Science,* 2**,** 204.

77 NASIR, S., AYDIN, M. A., KARAHAN, N., DEMIRY REK, D. & SARGON, M. 2006. New microvenous anastomosis model for microsurgical training: external jugular vein. *Journal of reconstructive microsurgery,* 22**,** 625-630.

78 LI, W., TUTTON, S., VU, A. T., PIERCHALA, L., LI, B. S., LEWIS, J. M., PRASAD, P. V. & EDELMAN, R. R. 2005. First-pass contrast-enhanced magnetic resonance angiography in humans using ferumoxytol, a novel ultrasmall superparamagnetic iron oxide (USPIO)-based blood pool agent. *Journal of Magnetic Resonance Imaging,* 21**,** 46-52.

79 CHRISTEN, T., NI, W., QIU, D., SCHMIEDESKAMP, H., BAMMER, R., MOSELEY, M. & ZAHARCHUK, G. 2013. High-resolution cerebral blood volume imaging in humans using the blood pool contrast agent ferumoxytol. *Magnetic resonance in medicine,* 70**,** 705-710.

80 D'ARCEUIL, H., COIMBRA, A., TRIANO, P., DOUGHERTY, M., MELLO, J., MOSELEY, M., GLOVER, G., LANSBERG, M. & BLANKENBERG, F. 2013. Ferumoxytol enhanced resting state fMRI and relative cerebral blood volume mapping in normal human brain. *NeuroImage,* 83**,** 200-209.

81 PATHAK, A. P., RAND, S. D. & SCHMAINDA, K. M. 2003. The effect of brain tumor angiogenesis on the in vivo relationship between the gradient-echo relaxation rate change (ΔR2*) and contrast agent (MION) dose. *Journal of Magnetic Resonance Imaging,* 18**,** 397-403.

82 YANG, M., CHRISTOFORIDIS, G. A., FIGUEREDO, T., HEVERHAGEN, J. T., ABDULJALIL, A. & KNOPP, M. V. 2005. Dosage determination of ultrasmall particles of iron oxide for the delineation of microvasculature in the Wistar rat brain. *Investigative radiology,* 40**,** 655.

83 BOLAN, P. J., YACOUB, E., GARWOOD, M., UGURBIL, K. & HAREL, N. 2006. In vivo micro-MRI of intracortical neurovasculature. *Neuroimage,* 32**,** 62-69.

84 BOSOMTWI, A., JIANG, Q., DING, G. L., ZHANG, L., ZHANG, Z. G., LU, M., EWING, J. R. & CHOPP, M. 2008. Quantitative evaluation of microvascular density after stroke in rats using MRI. *Journal of Cerebral Blood Flow & Metabolism,* 28**,** 1978-1987.

85 WU, S. H., LIN, C. Y., HUNG, Y., CHEN, W., CHANG, C. & MOU, C. Y. 2011. PEGylated silica nanoparticles encapsulating multiple magnetite nanocrystals for high-performance microscopic magnetic resonance angiography. *Journal of Biomedical Materials Research Part B: Applied Biomaterials,* 99**,** 81-88.

86 YANEV, P. & DIJKHUIZEN, R. M. 2012. In vivo imaging of neurovascular remodeling after stroke. *Stroke,* 43**,** 3436-3441.

87 MAMANI, J. B., MALHEIROS, J. M., CARDOSO, E. F., TANN S, A., SILVEIRA, P. H. & GAMARRA, L. F. 2012. In vivo magnetic resonance imaging tracking of C6 glioma cells labeled with superparamagnetic iron oxide nanoparticles. *Einstein (Sao Paulo),* 10**,** 164-170.

88 CHEN, C., CHEN, Y.-C., HSIAO, H.-Y., CHANG, C. & CHERN, Y. 2013. Neurovascular abnormalities in brain disorders: highlights with angiogenesis and magnetic resonance imaging studies. *Journal of biomedical science,* 20**,** 1-8.

89 LIN, C.-Y., SIOW, T. Y., LIN, M.-H., HSU, Y.-H., TUNG, Y.-Y., JANG, T., RECHT, L. & CHANG, C. 2013. Visualization of rodent brain tumor angiogenesis and effects of antiangiogenic treatment using 3D ΔR2-μMRA. *Angiogenesis,* 16**,** 785-793.

90 LIN, C.-Y., CHANG, C., CHEUNG, W.-M., LIN, M.-H., CHEN, J.-J., HSU, C. Y., CHEN, J.-H. & LIN, T.-N. 2008. Dynamic changes in vascular permeability, cerebral blood volume, vascular density, and size after transient focal cerebral ischemia in rats: evaluation with contrast-enhanced magnetic resonance imaging. *Journal of Cerebral Blood Flow & Metabolism,* 28**,** 1491-1501.

91 HOWLES, G. P., GHAGHADA, K. B., QI, Y., MUKUNDAN, S. & JOHNSON, G. A. 2009. High-resolution magnetic resonance angiography in the mouse using a nanoparticle blood-pool

contrast agent. *Magnetic Resonance in Medicine,* 62**,** 1447-1456.

92 EL TAYARA, N. E. T., DELATOUR, B., VOLK, A. & DHENAIN, M. 2010. Detection of vascular alterations by in vivo magnetic resonance angiography and histology in APP/PS1 mouse model of Alzheimer's disease. *Magnetic Resonance Materials in Physics, Biology and Medicine,* 23**,** 53-64.

93 KLOHS, J., BALTES, C., PRINCZ-KRANZ, F., RATERING, D., NITSCH, R. M., KNUESEL, I. & RUDIN, M. 2012. Contrast-enhanced magnetic resonance microangiography reveals remodeling of the cerebral microvasculature in transgenic ArcAβ mice. *The Journal of Neuroscience,* 32**,** 1705-1713.

94 PORT, J. D. & POMPER, M. G. 2000. Quantification and minimization of magnetic susceptibility artifacts on GRE images. *Journal of computer assisted tomography,* 24**,** 958-964.

95 IMAI, H., TANAKA, Y., NOMURA, N., TSUTSUMI, Y., DOI, H., KANNO, Z., OHNO, K., ONO, T. & HANAWA, T. 2013. Three-dimensional quantification of susceptibility artifacts from various metals in magnetic resonance images. *Acta biomaterialia,* 9**,** 8433-8439.

96 OGAWA, S. & LEE, T. M. 1990. Magnetic resonance imaging of blood vessels at high fields: in vivo and in vitro measurements and image simulation. *Magnetic Resonance in Medicine,* 16**,** 9-18.

97 SMALL, W. C., NELSON, R. C. & BERNARDINO, M. E. 1993. Dual contrast enhancement of both T1-and T2-weighted sequences using ultrasmall superparamagnetic iron oxide. *Magnetic resonance imaging,* 11**,** 645-654.

98 HAN, S., CHO, J., JUNG, H., SUH, J., KIM, J., KIM, Y., CHO, G. & CHO, H. 2015. Robust MR assessment of cerebral blood volume and mean vessel size using SPION-enhanced ultrashort echo acquisition. *NeuroImage,* 112**,** 382-389.

99 KWON, H. J., SHIM, W. H., CHO, G., CHO, H. J., JUNG, H. S., LEE, C. K., LEE, Y. S., BAEK, J. H., KIM, E. J. & SUH, J. Y. 2015. Simultaneous evaluation of vascular morphology, blood volume and transvascular permeability using SPION-based, dual-contrast MRI: imaging optimization and feasibility test. *NMR in Biomedicine,* 28**,** 624-632.

100 HU, F., JIA, Q., LI, Y. & GAO, M. 2011. Facile synthesis of ultrasmall PEGylated iron oxide nanoparticles for dual-contrast T1-and T2-weighted magnetic resonance imaging. *Nanotechnology,* 22**,** 245604.

101 JUNG, H., PARK, B., LEE, C., CHO, J., SUH, J., PARK, J., KIM, Y., KIM, J., CHO, G. & CHO, H. 2014. Dual MRI T and T contrast with size-controlled iron oxide nanoparticles. *Nanomedicine*.

102 !!! INVALID CITATION !!! {}.

103 PATHAK, A. P., WARD, B. D. & SCHMAINDA, K. M. 2008. A novel technique for modeling susceptibility-based contrast mechanisms for arbitrary microvascular geometries: the finite perturber method. *Neuroimage,* 40**,** 1130-1143.

104 KIM, S. G., HAREL, N., JIN, T., KIM, T., LEE, P. & ZHAO, F. 2013. Cerebral blood volume MRI with intravascular superparamagnetic iron oxide nanoparticles. *NMR in Biomedicine,* 26**,** 949-962.

105 WEISSKOFF, R., ZUO, C. S., BOXERMAN, J. L. & ROSEN, B. R. 1994. Microscopic susceptibility variation and transverse relaxation: theory and experiment. *Magnetic Resonance in Medicine,* 31**,** 601-610.

106 KIM, H., CHO, J., KIM, Y. R., SONG, Y., CHUN, S.-I., SUH, J.-Y., KIM, J. K., RYU, Y.-H., CHOI, S.-M. & CHO, H. 2014. Response of the Primary Auditory and Non-Auditory Cortices to Acoustic Stimulation: A Manganese-Enhanced MRI Study. *PloS one,* 9**,** e90427.

107 NY L, L. G., UDUPA, J. K. & ZHANG, X. 2000. New variants of a method of MRI scale standardization. *Medical Imaging, IEEE Transactions on,* 19**,** 143-150.

108 MADABHUSHI, A. & UDUPA, J. K. 2005. Interplay between intensity standardization and inhomogeneity correction in MR image processing. *Medical Imaging, IEEE Transactions on,* 24**,** 561-576.

109 CANNY, J. 1986. A computational approach to edge detection. *Pattern Analysis and Machine Intelligence, IEEE Transactions on***,** 679-698.

110 LEE, T.-C., KASHYAP, R. L. & CHU, C.-N. 1994. Building skeleton models via 3-D medial surface axis thinning algorithms. *CVGIP: Graphical Models and Image Processing,* 56**,** 462-478.

111 KERSCHNITZKI, M., KOLLMANNSBERGER, P., BURGHAMMER, M., DUDA, G. N., WEINKAMER, R., WAGERMAIER, W. & FRATZL, P. 2013. Architecture of the osteocyte network correlates with bone material quality. *Journal of bone and mineral research,* 28**,** 1837-1845.

112 BALTES, C., RADZWILL, N., BOSSHARD, S., MAREK, D. & RUDIN, M. 2009. Micro MRI of the mouse brain using a novel 400 MHz cryogenic quadrature RF probe. *NMR Biomed,* 22**,** 834-842.

113 PIĘDZIA, W., JASIŃSKI, K., KALITA, K., TOMANEK, B. & WĘGLARZ, W. P. 2014. White and gray matter contrast enhancement in MR images of the mouse brain in vivo using IR UTE with a cryo-coil at 9.4 T. *Journal of neuroscience methods,* 232**,** 30-35.

114 ZHOU, X., LIANG, Z. P., COFER, G. P., BEAULIEU, C. F., SUDDARTH, S. A. & JOHNSON, G. A. 1993. Reduction of ringing and blurring artifacts in fast spin-echo imaging. *Journal of Magnetic Resonance Imaging,* 3**,** 803-807.

115 WAN, X., PARKER, D. L., LEE, J. N., BUSWELL, H. R. & GULLBERG, G. T. 1995. Reduction of phase error ghosting artifacts in thin slice fast spin-echo imaging. *Magnetic resonance in medicine,* 34**,** 632-638.

116 KHOLMOVSKI, E. G., PARKER, D. L. & ALEXANDER, A. L. 2000. A generalized k-sampling scheme for 3D fast spin echo. *Journal of Magnetic Resonance Imaging,* 11**,** 549-558.

117 ZIMMER, C., WEISSLEDER, R., POSS, K., BOGDANOVA, A., WRIGHT JR, S. C. & ENOCHS, W. S. 1995. MR imaging of phagocytosis in experimental gliomas. *Radiology,* 197**,** 533-538.

118 MOORE, A., MARECOS, E., BOGDANOV JR, A. & WEISSLEDER, R. 2000. Tumoral distribution of long-circulating dextran-coated iron oxide nanoparticles in a rodent model 1. *Radiology,* 214**,** 568-574.

119 MCROBBIE, D. W., MOORE, E. A., GRAVES, M. J. & PRINCE, M. R. 2007. *MRI from Picture to Proton*, Cambridge university press.

120 SALVOLINI, U. & SCARABINO, T. 2006. *High Field Brain MRI*, Springer.

121 YUH, W. T., CHRISTOFORIDIS, G. A., KOCH, R. M., SAMMET, S., SCHMALBROCK, P., YANG, M. & KNOPP, M. V. 2006. Clinical magnetic resonance imaging of brain tumors at ultrahigh field: a state-of-the-art review. *Topics in magnetic resonance imaging: TMRI,* 17**,** 53.

122 DE SOUSA, P. L., LIVRAMENTO, J. B., HELM, L., MERBACH, A. E., M ME, W., DOAN, B. T., BELOEIL, J. C., PRATA, M. I., SANTOS, A. C. & GERALDES, C. 2008. In vivo MRI assessment of a novel GdIII-based contrast agent designed for high magnetic field applications. *Contrast media & molecular imaging,* 3**,** 78-85.

123 CARAVAN, P., FARRAR, C. T., FRULLANO, L. & UPPAL, R. 2009. Influence of molecular parameters and increasing magnetic field strength on relaxivity of gadolinium-and manganese-based T1 contrast agents. *Contrast media & molecular imaging,* 4**,** 89-100.

124 HELM, L. 2010. Optimization of gadolinium-based MRI contrast agents for high magnetic-field applications. *Future medicinal chemistry,* 2**,** 385-396.

125 HAGBERG, G. E. & SCHEFFLER, K. 2013. Effect of r1 and r2 relaxivity of gadolinium-based contrast agents on the T1-weighted MR signal at increasing magnetic field strengths. *Contrast media & molecular imaging,* 8**,** 456-465.

126 MIN, J., JUNG, H., SHIN, H.-H., CHO, G., CHO, H. & KANG, S. 2013. Implementation of p22 viral capsids as intravascular magnetic resonance T1 contrast conjugates via site-selective attachment of Gd (III)-chelating agents. *Biomacromolecules,* 14**,** 2332-2339.

127 GARIMELLA, P. D., DATTA, A., ROMANINI, D. W., RAYMOND, K. N. & FRANCIS, M. B. 2011. Multivalent, high-relaxivity MRI contrast agents using rigid cysteine-reactive gadolinium complexes. *Journal of the American Chemical Society,* 133**,** 14704-14709.

128 LUCON, J., QAZI, S., UCHIDA, M., BEDWELL, G. J., LAFRANCE, B., PREVELIGE JR, P. E. & DOUGLAS, T. 2012. Use of the interior cavity of the P22 capsid for site-specific initiation

of atom-transfer radical polymerization with high-density cargo loading. *Nature chemistry,* 4**,** 781-788.

129 QAZI, S., LIEPOLD, L. O., ABEDIN, M. J., JOHNSON, B., PREVELIGE, P., FRANK, J. A. & DOUGLAS, T. 2012. P22 viral capsids as nanocomposite high-relaxivity MRI contrast agents. *Molecular pharmaceutics,* 10**,** 11-17.

130 POKORSKI, J. K., BREITENKAMP, K., LIEPOLD, L. O., QAZI, S. & FINN, M. 2011. Functional virus-based polymer–protein nanoparticles by atom transfer radical polymerization. *Journal of the American Chemical Society,* 133**,** 9242-9245.

131 CARAVAN, P. 2009. Protein-targeted gadolinium-based magnetic resonance imaging (MRI) contrast agents: design and mechanism of action. *Accounts of chemical research,* 42**,** 851-862.

132 XUE, S., QIAO, J., JIANG, J., HUBBARD, K., WHITE, N., WEI, L., LI, S., LIU, Z. R. & YANG, J. J. 2014. Design of ProCAs (Protein-Based Gd3+ MRI Contrast Agents) with High Dose Efficiency and Capability for Molecular Imaging of Cancer Biomarkers. *Medicinal research reviews,* 34**,** 1070-1099.

133 YANG, J. J., YANG, J., WEI, L., ZURKIYA, O., YANG, W., LI, S., ZOU, J., ZHOU, Y., MANICCIA, A. L. W. & MAO, H. 2008. Rational design of protein-based MRI contrast agents. *Journal of the American Chemical Society,* 130**,** 9260-9267.

134 LI, S., JIANG, J., ZOU, J., QIAO, J., XUE, S., WEI, L., LONG, R., WANG, L., CASTIBLANCO, A. & WHITE, N. 2012. PEGylation of protein-based MRI contrast agents improves relaxivities and biocompatibilities. *Journal of inorganic biochemistry,* 107**,** 111-118.

135 KUDA-WEDAGEDARA, A. N. & ALLEN, M. J. 2014. Enhancing magnetic resonance imaging with contrast agents for ultra-high field strengths. *Analyst,* 139**,** 4401-4410.

136 USSELMAN, R. J., QAZI, S., AGGARWAL, P., EATON, S. S., EATON, G. R., RUSSEK, S. & DOUGLAS, T. 2015. Gadolinium-Loaded Viral Capsids as Magnetic Resonance Imaging Contrast Agents. *Applied Magnetic Resonance,* 46**,** 349-355.

137 GOLDMANN, E. 1907. The growth of malignant disease in man and the lower animals: with special reference to the vascular system. *The Lancet,* 170**,** 1236-1240.

138 PEER, D., KARP, J. M., HONG, S., FAROKHZAD, O. C., MARGALIT, R. & LANGER, R. 2007. Nanocarriers as an emerging platform for cancer therapy. *Nature nanotechnology,* 2**,** 751-760.

139 SEYMOUR, L., MIYAMOTO, Y., MAEDA, H., BRERETON, M., STROHALM, J., ULBRICH, K. & DUNCAN, R. 1995. Influence of molecular weight on passive tumour accumulation of a soluble macromolecular drug carrier. *European Journal of Cancer,* 31**,** 766-770.